Wind erosion in northern China: Insights from the western Qaidam fold belt, Loess Plateau, and Hami Basin

Paul Kapp, Alex Pullen, Jordan T. Abell, Liyun Zhang

PII: S0012-8252(24)00365-9

DOI: https://doi.org/10.1016/j.earscirev.2024.105037

Reference: EARTH 105037

To appear in: *Earth-Science Reviews*

Received date: 16 June 2024

Revised date: 21 October 2024

Accepted date: 28 December 2024

Please cite this article as: P. Kapp, A. Pullen, J.T. Abell, et al., Wind erosion in northern China: Insights from the western Qaidam fold belt, Loess Plateau, and Hami Basin, *Earth-Science Reviews* (2024), https://doi.org/10.1016/j.earscirev.2024.105037

Wind erosion in northern China: Insights from the western Qaidam fold belt, Loess Plateau, and Hami Basin

Paul Kapp[a,*], Alex Pullen[b], Jordan T. Abell[c], and Liyun Zhang[d]

[a]Department of Geosciences, University of Arizona, Tucson, Arizona 85721, USA
[b]Department of Environmental Engineering and Earth Sciences, Clemson University, Clemson, South Carolina 29634, USA
[c]Department of Earth and Environmental Sciences, Lehigh University, Bethlehem, Pennsylvania 18015, USA
[d]State Key Laboratory of Tibetan Plateau Earth System, Resources and Environment, Institute of Tibetan Plateau Research, Chinese Academy of Sciences, Beijing 100101, China
* Corresponding author.

E-mail addresses: pkapp@arizona.edu (P. Kapp), apullen@clemson.edu (A. Pullen), joa423@lehigh.edu (J.T. Abell), zly@itpcas.ac.cn (L. Zhang)

ABSTRACT

Pliocene – Quaternary wind erosion profoundly modified the physiography of northern China at a large range of spatial (10 m to >100 km) and temporal (10 ka to Myr) scales. In the western Qaidam Basin along the northeastern margin of the Tibetan Plateau, northwesterly winds sculpted yardangs in actively folding Miocene – Pleistocene strata. Wind erosion was most dominant during glacial periods, whereas lacustrine deposition was more extensive during warmer and wetter interglacial periods. Cyclical wind erosion and sedimentation is recorded by paleoyardangs in Pliocene – Pleistocene strata. A thickness of hundreds to thousands of meters of strata has been blown off the crests of Qaidam anticlines. Wind erosion initiated at ~3 Ma and increased in spatial extent and magnitude from early to late Pleistocene time as aridity intensified and strata were tectonically uplifted. Qaidam anticlines are propagating in the windward direction and accelerated in growth concomitant with wind erosion, raising the possibility that spatially variable removal of mass by wind influenced the rates and kinematics of deformation. To the east of Qaidam Basin is the Chinese Loess Plateau. The northern, windward margin of the central Loess Plateau is an up to 400-m-high erosional escarpment made of loess that slopes

northward into the wind-eroded and endorheic Mu Us Desert. During Pleistocene aridification and expansion of the Mu Us Desert, the Loess Plateau escarpment margin retreated as it was wind eroded while loess continued to accumulate downwind and further build the plateau. The Hami Basin within the eastern Tian Shan of northwestern China is one of the windiest regions on Earth today and part of the broader Gobi Desert that extends eastward into Mongolia. In the north-central Hami Basin, northerly winds sculpted yardangs in Cretaceous strata and have blown a thickness of ≥200 m of Cretaceous – Pleistocene strata out of the closed basin. Wind erosion of northern Hami Pleistocene alluvial deposits led to the widespread development of unconsolidated gravel deposits and pavements. These gravels armor underlying alluvial strata from further wind erosion and thereby suppress dust emissions, despite extreme winds. The Hami and other Gobi Desert basins may have experienced an overall decrease in dust emissions from Pliocene to late Pleistocene time as the volume of silt-bearing strata decreased in the basins while the area of the basins armored by gravel increased. Structural unloading joints in some Hami yardang fields accelerate rates of wind erosion and yardang demise, and their wind-parallel orientation provides another potential example of an interplay between wind erosion and rock deformation. This review suggests that the sources and fluxes of Asian dust were not spatially uniform through the Neogene and Quaternary. The geological and topographic history, landscape evolution, and short and long-term climate variations in Asia all need to be simultaneously evaluated when interpreting terrestrial and marine archives of dust in the context of past and future climate changes.

Keywords:
wind erosion; dust; yardang; landscape evolution; Loess Plateau; Qaidam; desert

1. Introduction

Every human is intimate with the wind. This anthropogenic connection with wind processes and their role in eroding bedrock, generating bedforms and landforms, and transporting and depositing sediment may date back to our earliest ancestors. Some of the oldest (1.26 – 2.12 Ma) hominins outside of Africa lived, breathed, and were buried in dust comprising the Chinese Loess Plateau (Zhu et al., 2018b) (Figs. 1 and 2)—the largest terrestrial accumulation of Quaternary loess on Earth (Kukla and An, 1989; Porter, 2007). Wind plays several important roles in the climate system. Atmospheric circulation is a major mechanism for redistributing

thermal energy and moisture around the globe (Toggweiler and Samuels, 1995; Kuhlbrodt et al., 2007). Near-surface winds loft dust into the atmosphere, whereas upper-level winds transport it long distances before it settles on land or into the oceans (Fig. 1). Mineral dust itself influences climate in a variety of ways. As an aerosol, dust can alter Earth's radiative forcing by directly scattering and/or absorbing incoming solar radiation, impacting cloud formation and characteristics, altering atmospheric chemistry, and changing the albedo of both land and sea ice (Kok et al., 2023). Additionally, dust, in its capacity as a carrier of elements and compounds essential for life, can stimulate biological productivity in the ocean and on land, solidifying its importance in the marine and terrestrial carbon cycles (Bopp et al., 2003; Jickells et al., 2005; Boy and Wilcke, 2008; Bristow et al., 2010; Moore et al., 2013; Aciego et al., 2017).

Wind is an important agent of sediment transport and erosion (by deflation and abrasion by wind-blown sediment) in all of Earth's major deserts. During the early twentieth century, a subset of geomorphologists argued that wind erosion was more important than fluvial erosion in beveling desert landscapes, and even more important than normal faults in producing the Basin and Range topography of southwestern North America (Keyes, 1912). Historical perspectives about these extreme "eoliation" views and why they were dismissed have been provided (Goudie, 2012; Orme, 2013). The pendulum may have swung too far away from "wind power," however, such that many fundamental questions and likely discoveries remain encumbered by conviction rather than scientific inquiry. However, the pendulum is starting to swing back because of a combination of increased cross-disciplinary research, the growing understanding of how important wind processes are on other planetary bodies, increasing availability of high-resolution imagery of Earth and other planetary bodies, the need to accurately forecast anthropogenic climate change, and an increasing desire to understand dust as a growing societal hazard (e.g., visibility and aviation, human health, military operations), among other factors. Below we introduce specific outstanding questions that we touch upon in this review of wind-themed research in northern China.

1.1. Yardangs and paleoyardangs

Yardangs are wind-sculpted and wind-parallel bedrock ridges that were first described scientifically in China near Lop Nur (Fig. 2) (Hedin, 1903). Yardangs *sensu stricto* are sculpted by unidirectional winds and streamlined, exhibiting a wind-parallel topographic profile that is

steep and highest in elevation in the upwind direction and tapers downwind, and a map-view geometry that is tear-drop-shaped. This morphology minimizes pressure and skin friction drag (McCauley et al., 1977; Ward and Greeley, 1984; Goudie, 2007). However, many wind-sculpted bedrock ridges deviate from this classical geometry and exhibit diverse forms (Halimov and Fezer, 1989) because of rheologic heterogeneities in bedrock lithologies (e.g., interbedded strong and weak sedimentary rocks), variable strike and dip directions of tilted sedimentary rocks and how they vary as a function of the wind direction, and the influence of sculpting by more than one geomorphically-effective wind direction (Li et al., 2016; Hu et al., 2017; Pelletier, 2018; Pelletier et al., 2018; Xiao et al., 2021). The term yardang is widely extended to include any linear bedrock ridge sculpted by wind (Laity, 2011).

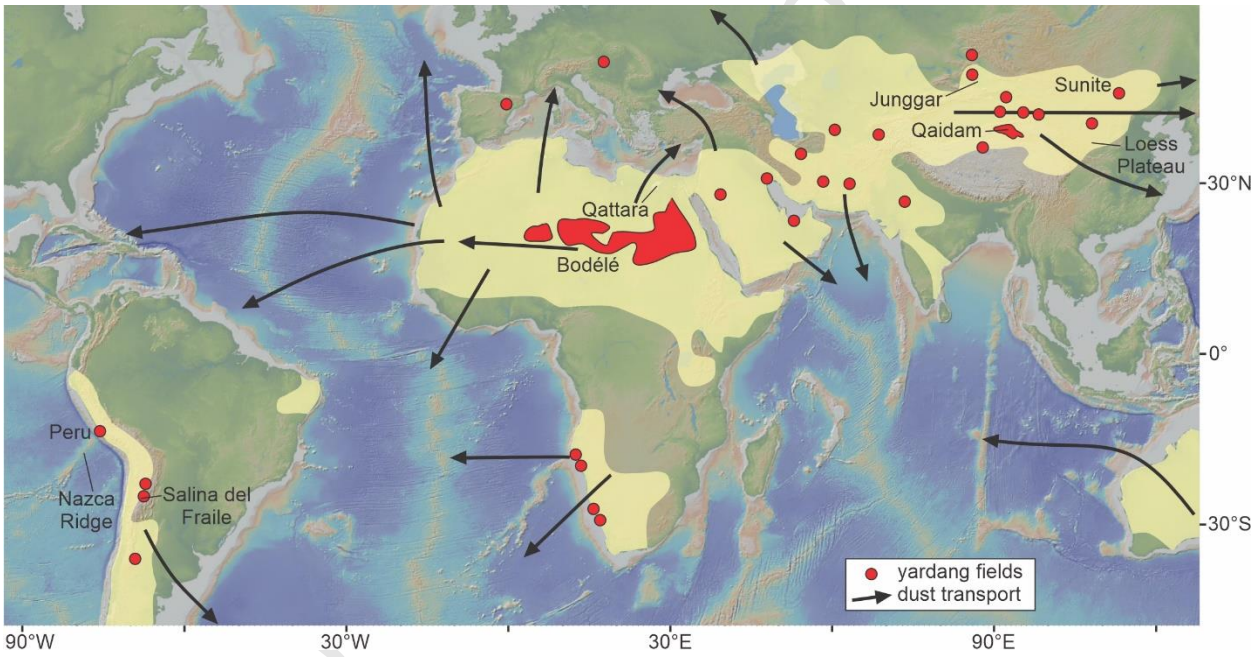

Figure 1. *Major modern dust sources (shaded in yellow), dust-transporting wind directions (black arrows) modified from Muhs et al. (2014) and Middleton (2020), and locations of yardang fields (in red circles and shading). Fields of megayardangs in the Pannonian Basin (Sebe et al., 2011) and Russian/Siberian Altai (Potter et al., 2023) are covered in vegetation. Atmospheric dust transport directions vary in detail among studies and are generalized.*

While yardangs are present in almost all of Earth's deserts, and on other planetary bodies, unambiguous documentation of paleoyardangs in the stratigraphic record is scant. Purported paleoyardang ridges in Permian eolian sandstone and buried by Triassic strata in Utah, U.S.A., exhibit asymmetric ridge-perpendicular topographic profiles (Tewes and Loope, 1992), which

does not disprove but queries the interpretation. Paleoyardangs were raised as one of two interpretations of enigmatic ridges along the eolian-marine boundary within Jurassic strata, also in Utah (Jones and Blakey, 1993). Interpreted paleoyardang ridges were mapped in ~2.4 Ma lacustrine strata of the Qaidam Basin (Figs. 1 and 2), but their long-axis orientations are different than those of yardangs in the modern landscape, suggesting that either the near-surface wind pattern changed through time in the basin (Heermance et al., 2013) or that they are misinterpreted. We present new remote observations which suggest that paleoyardangs are ubiquitous in Pliocene through upper Pleistocene strata of the western Qaidam Basin—and that a subset exhibits orientations that differ substantially from the trends of prominent yardangs fields in the basin today. It is ironic that convincing images of paleoyardangs were documented on Mars (Wang et al., 2018; Dromart et al., 2021) before Earth.

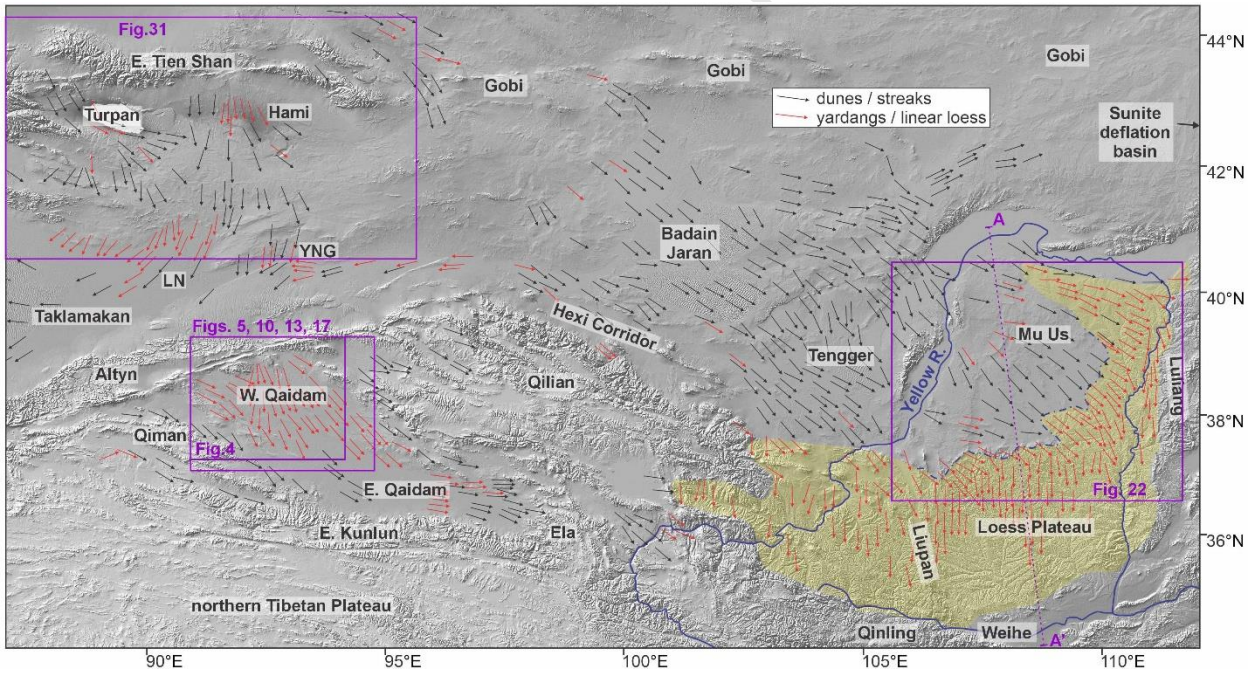

Figure 2. *Shaded relief map (www.geomapapp.org) showing major deflationary bedrock-floored and sandy deserts in China, the Chinese Loess Plateau, and location of the Yellow River. Arrows show geomorphologically-effective wind directions based on previous (Kapp et al., 2011; Kapp et al., 2015) and our new geomorphologic mapping in Google Earth. Red arrows indicate dominant orientations of wind-sculpted linear bedrock topography (yardangs and linear loess topography). Black arrows are based on sand dune geometries and wind streaks. Lop Nur (LN); Yardang National Geopark (YNG).*

1.2. Potential linkages between wind processes and tectonics

Climatically-driven changes in the spatial distribution and rates of erosion within mountain belts may exert a strong influence on the rates and kinematics of rock deformation (Dahlen et al., 1984; Willett, 1999; Beaumont et al., 2001; Montgomery et al., 2001; Whipple, 2009). There are a growing number of case examples, albeit some more controversial than others, that emphasize the importance of fluvial or glacial erosion and the extent to which erosion and deformation are spatially focused (Zeitler et al., 2001; Reiners et al., 2003; Simpson, 2004; Berger et al., 2008; Egholm et al., 2009). In contrast, there is one case example in which spatially variable unloading of mass by wind might have influenced the rates and kinematics of folding in the Qaidam Basin (Kapp et al., 2011) (Fig. 2). In this review, we expand on the observations motivating this wind-erosion-enhanced tectonics hypothesis, along with its predictions. We also explore the potential role of wind erosion in influencing the orientations of structural joints in Cretaceous strata within the Hami Basin (Fig. 2).

1.3. Chinese Loess Plateau

The up to ~350-m-thick alternating loess-paleosol stratigraphy of the Chinese Loess Plateau (Fig. 2) provides one of the richest and most extensively studied terrestrial records of Pliocene – Quaternary climate change (Tungsheng and Zhongli, 1993; An, 2000; Kohfeld and Harrison, 2003; Sun and An, 2005; Porter, 2007; Maher, 2016). Massive layers of loess accumulated during glacial periods when central Asia was colder and drier. The intervening accretionary paleosols developed during warmer and wetter interglacial periods when the East Asian summer monsoon penetrated farther inland. Rarely addressed is why the stratigraphy of the Chinese Loess Plateau defines a relatively high-elevation (~1600 m), albeit fluvially incised, plateau and how the plateau was built. Implicit in much of the literature is that the Loess Plateau is a geographically static feature that was incised as its surface was tectonically uplifted. There are no active fault systems that could have uniformly uplifted the Loess Plateau, however, and it has been shown that high topographic relief and river systems characterized the Loess Plateau region prior to and during the accumulation of Neogene – Quaternary loess (Porter and An, 2005; Xiong et al., 2014; Zhu et al., 2018a). Wind erosion has also been suggested to explain the northern, windward margin of the Loess Plateau, which is defined by a steep and up to 400-m-high erosional escarpment composed of loess, in addition to widely developed wind-parallel

linear loess topography (Kapp et al., 2015). This review expands on the hypothesis that the Loess Plateau grew upward through eolian sediment accumulation while its windward margin retreated downwind as a result of wind erosion and net expansion of the Mu Us Desert during the Pliocene – Pleistocene (Kapp et al., 2015).

1.4. Evolving landscapes, winds, and sources and fluxes of dust

The bulk of global atmospheric mineral dust is sourced from geographically localized "hot spots," many of which are endorheic playa basins that hosted large lakes during wetter climates (Prospero et al., 2002; Washington et al., 2003; Todd et al., 2007). In China, modern dust point sources are most abundant along the eastern and northern margins of the Taklamakan Desert (paleolake Lop Nur and alluvial fans and playas along the southern flank of the Tian Shan), along the Hexi Corridor, and within the Qaidam and composite Turpan-Hami basins (Nobakht et al., 2021). The central Gobi Desert is also the locus of major dust storm outbreaks (Xuan and Sokolik, 2002; Wang et al., 2008), emitting clouds of dust that track to the southeast across the Loess Plateau or to the east across the Pacific Ocean (Husar et al., 2001; Sun, 2002). Dust from the Taklamakan Desert is lofted higher into—and may travel even farther in the atmosphere—than that of Gobi-sourced dust (Uno et al., 2009).

While studies of the modern Asian dust engine provide valuable insights, numerous factors must be considered in evaluating dust source regions and emissions in the past. In this review, we generally consider changes over two timescales: that of Quaternary glacial-interglacial cyclicity (40-100 kyr), and the overall cooling and drying of Asian climate from Pliocene to early Pleistocene to late Pleistocene time (Ding et al., 2005; Sun and An, 2005; Fang et al., 2020). Loess layers of the Loess Plateau were dominantly deposited during colder and drier glacial periods whereas intervening accretionary paleosols accumulated during interglacial periods (Tungsheng and Zhongli, 1993; An, 2000; Kohfeld and Harrison, 2003; Sun and An, 2005; Porter, 2007; Maher, 2016). Enhanced surface wind gustiness and windstorm outbreaks are expected during glacial periods with larger meridional temperature gradients over Asia and a stronger Siberian high-pressure system (Roe, 2009; McGee et al., 2010; Sun et al., 2011).

Landscape properties, including the availability of silt to be deflated, exert a primary control on wind erosion and dust production (Gillette et al., 1980; Sweeney et al., 2011). Landscape properties likely changed dramatically between glacial-interglacial periods as well as

throughout Pliocene – Quaternary time. For example, the Gobi Desert is named after its stony nature, with extensive areas being covered by dark-colored gravel deposits and pavements. The Gobi Desert is a significant source of dust today, but it would be an even larger emitter of dust if its surface was less armored by tightly-packed gravel and more fertile with silt. This review summarizes studies of the Hami Basin located to the northeast of the Taklamakan Desert within the eastern Tian Shan (Fig. 2) as a case example of how a stony desert landscape might evolve and impact dust emissions as well as how near-surface winds may be impacted by changes in surface roughness and albedo.

Climate-driven changes in the position of the mid-latitude westerly jet is another factor that needs to be considered when assessing the Pliocene – Quaternary history of wind erosion and dust dynamics. The mid-latitude westerly jets are likely shifting poleward as anthropogenic global warming progresses (Chen and Held, 2007; Yang et al., 2020a; Gulev et al., 2021). This poleward shift is consistent with global atmospheric circulation models and empirical studies suggesting that the position of the westerly jets shift equatorward during colder climates (Toggweiler et al., 2006; Toggweiler and Russell, 2008; Kapp et al., 2011; Pullen et al., 2011; Quade and Kaplan, 2017; Abell et al., 2021; Pullen et al., 2022; Stubbins et al., 2023). If correct, this implies that the more southerly central Asian dust sources (e.g., Qaidam Basin and Tibetan Plateau) may have been more significant dust sources during past glacial maxima and during the overall colder late Pleistocene relative to the early Pleistocene.

A review of the plethora of Chinese Loess Plateau provenance studies is beyond the scope of this review and only a subset of recent studies are cited here (Stevens et al., 2013; Licht et al., 2016; Maher, 2016; Zhang et al., 2021; Zhang et al., 2022b; Zhou et al., 2022; Bohm et al., 2023; Peng et al., 2023). A paradigm is that the Gobi and adjacent sand deserts were dominant sediment sources, in large part because loess grain size decreases from northwest to southeast across the central Loess Plateau and that dust generated during some modern Gobi Desert windstorms is transported by low-level northwesterly winds and falls out over the Loess Plateau (Sun, 2002; Ding et al., 2005; Sun et al., 2008). The appreciation of the Yellow River as an important sediment source is growing (Stevens et al., 2013; Nie et al., 2015; Licht et al., 2016; Zhang et al., 2021; Peng et al., 2023). The Yellow River has its headwaters on the northeastern Tibetan Plateau, flows northward through the western Loess Plateau and along the western margin of the Mu Us Desert, then makes its ~90° bends eastward and then southward through the

eastern Loess Plateau (Fig. 2). The Yellow River has taken this course for at least the past ~2 Myr (Craddock et al., 2010) and its reaches to the west and north of the Mu Us Desert were intermittently filled with lakes throughout the Pliocene and Quaternary (Jia et al., 2016; Li et al., 2017; Li et al., 2020; Li et al., 2023). The Yellow River has thus provided a long-term and large supply of sand and silt to the margins of the Mu Us Desert that could be reworked by wind and transported to the Loess Plateau. Additionally, the river includes sediment sourced from northeastern Tibet such that a northeastern Tibet provenance signal in Loess Plateau strata, which is increasingly being recognized, does not necessarily implicate a direct dust source-sink relationship between the two regions. Nonetheless, we maintain that the Qaidam Basin, located directly west of the Loess Plateau (Figs. 1 and 2), must have been a major dust source hotspot during, at minimum, Pleistocene glacial periods (Bowler et al., 1987; Kapp et al., 2011), and it is here where we begin our more in-depth review.

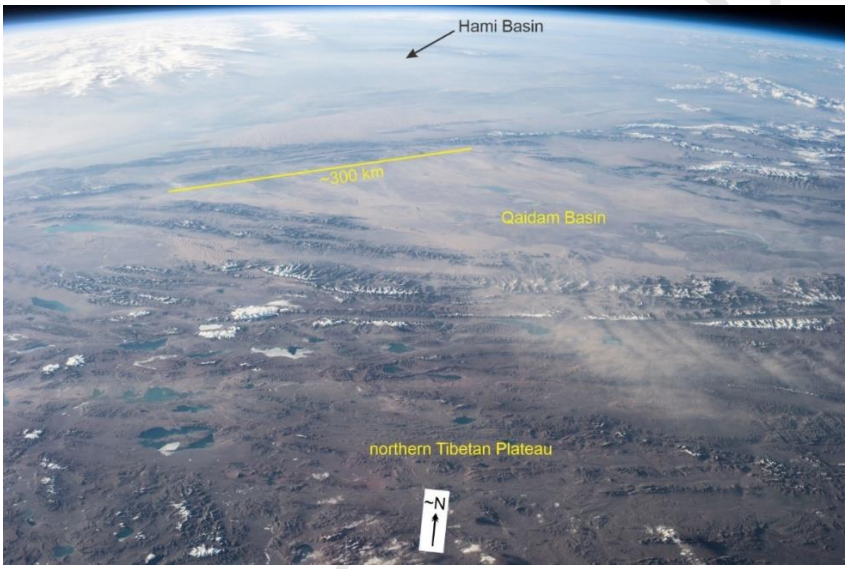

Figure 3. *Astronaut photograph looking northward across the northern Tibetan Plateau and Qaidam Basin. Credit: Earth Science and Remote Sensing Unit, NASA Johnson Space Center. NASA Photo ID: ISS036-E-6937. Date: 2013.06.09. Time: 12:17:27 GMT. Spacecraft nadir point: 30.4°N, 91.5°E. Altitude: 404 km.*
https://eol.jsc.nasa.gov/SearchPhotos/photo.pl?mission=ISS036&roll=E&frame=6937

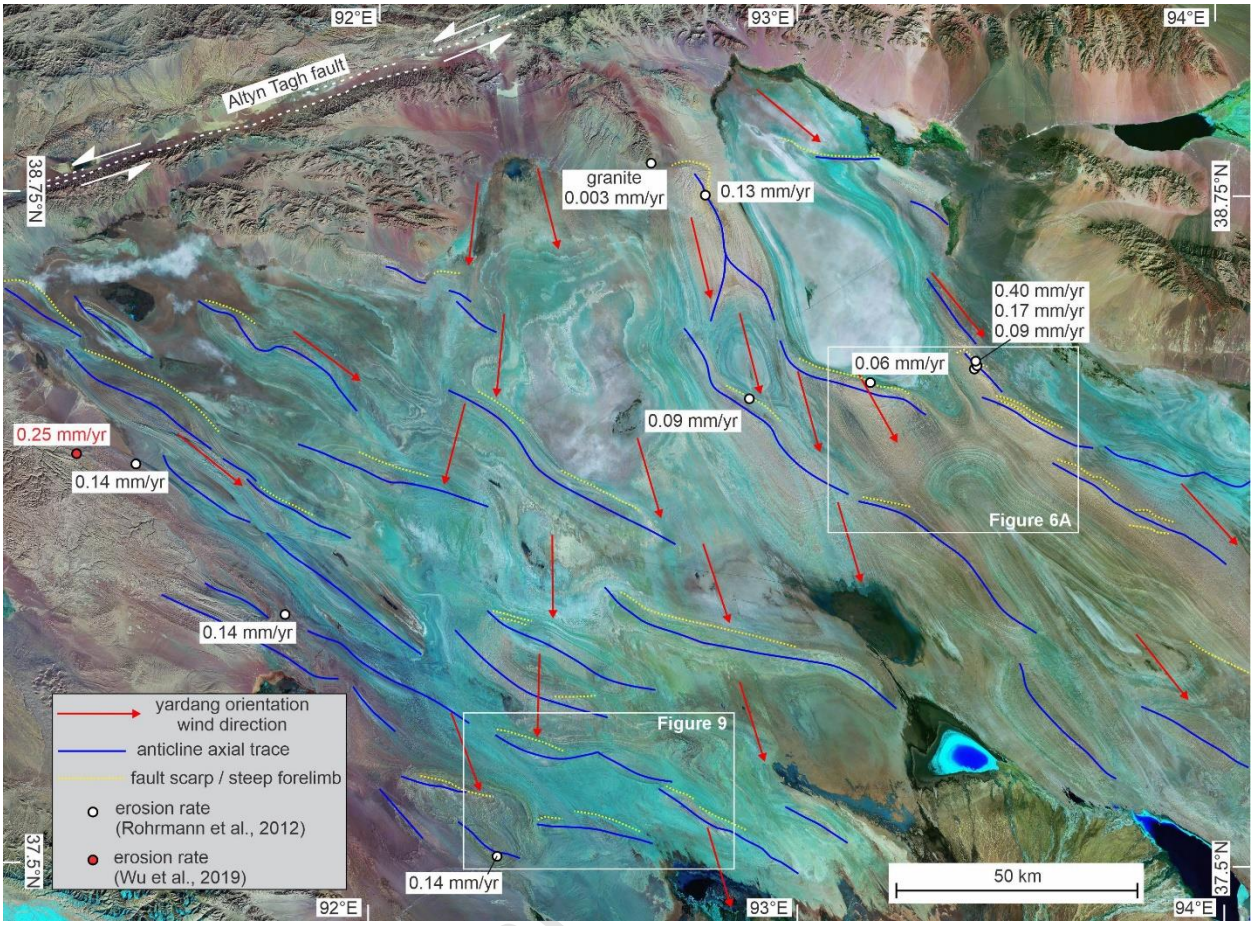

Figure 4. *Satellite image of the western Qaidam Basin. Superimposed are traces of major anticlines (blue lines), the steeper forelimbs and locally thrust faults associated with the anticlines (dotted yellow lines), geomorphically-effective wind directions (red arrows), and localities where erosion rates have been estimated (circles).*

2. Qaidam Basin

The Qaidam Basin abuts the northeastern margin of the Tibetan Plateau (Figs. 1-3), spans an area of ~120,000 km^2, and exhibits surface elevations ranging from ~2.7 to 3.0 km across most of its floor. The basin is endorheic, being bounded by the Qiman – Eastern Kunlun, Altyn, Qilian, and Ela mountains to the south, northwest, northeast, and east, respectively (Fig. 2). The majority of the basin is unvegetated (Jin et al., 2013) and hyper-arid, with a mean annual precipitation of <50 mm/yr (chinamaps.org).

Some refer to the Qaidam as the largest basin within the northeastern Tibetan Plateau, but we distinguish the Tibetan Plateau proper as a contiguous high-elevation (~5 km mean elevation) and low-relief physiographic province, with its northern margin being the Eastern Kunlun

Mountains (Kapp and DeCelles, 2019) (Fig. 2). The physiographic Tibetan Plateau is also actively extending ~E-W by normal and strike-slip faulting, whereas the Qaidam Basin and adjacent mountain ranges are actively shortening ~NE-SW by folding and thrust faulting (Taylor and Yin, 2009) (Figs. 4-6).

The Qaidam Basin contains up to 10-12 km of Cenozoic basin fill within a regional ~NW-SE-trending synclinorium that developed during uplift of adjacent mountain ranges (Xia et al., 2001; Yin et al., 2008; Cheng et al., 2021; Xiao et al., 2021). Endorheic drainage was established in the Qaidam Basin by at least Oligocene time (Yin et al., 2008; Zhuang et al., 2011). Cenozoic sediment accumulation was most voluminous in the western Qaidam Basin until late Miocene – Quaternary time, when it became partitioned by crustal deformation and large sedimentary depocenters migrated toward the eastern Qaidam Basin (Yin et al., 2008; Bao et al., 2017).

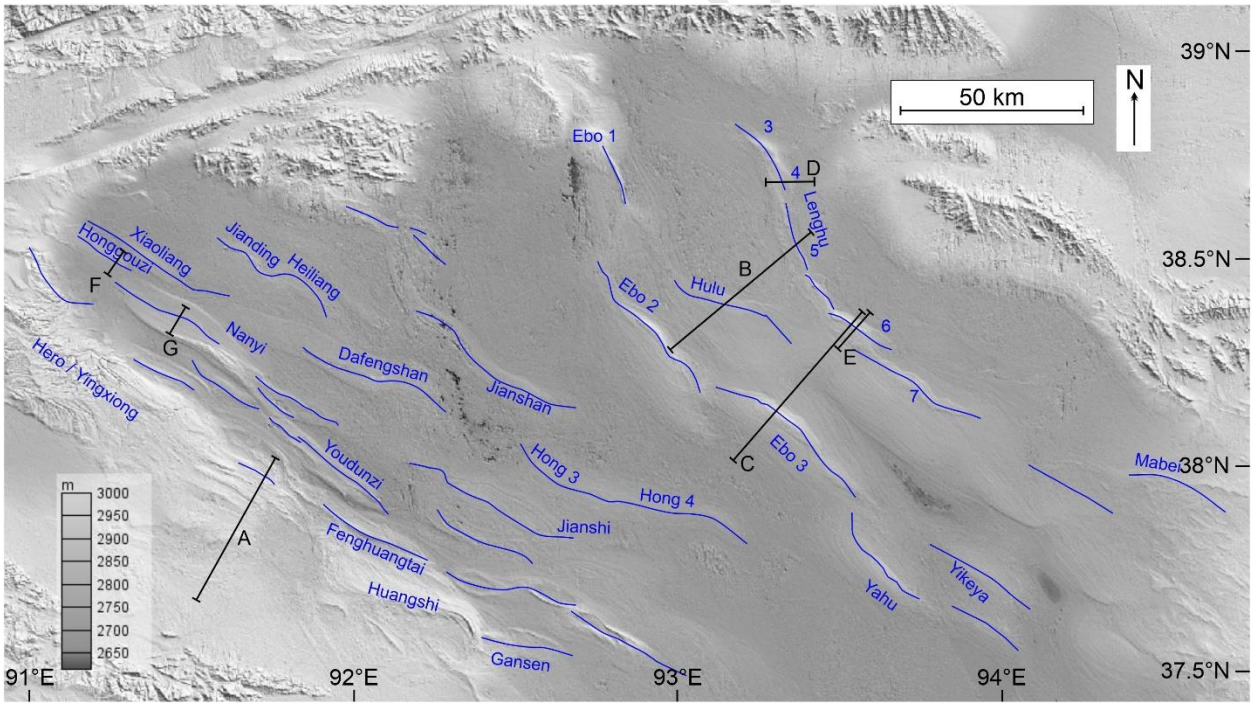

Figure 5. *Shaded relief map (www.geomapapp.org) of the wind-eroded western Qaidam fold belt. Blue lines indicate axial traces of major anticlines. Cross-sections along lines A-G are provided in Figure 7.*

2.1. Wind-eroded Qaidam fold belt

Despite being surrounded by mountain ranges and encompassing a multitude of closed sub-depressions, most of the western two-thirds of the Qaidam Basin is not filling with sediment. Instead, the western Qaidam Basin exposes an actively growing NW-SE-trending fold belt (Figs. 4-7) of mostly Pliocene – Pleistocene lacustrine sedimentary rocks (Kapp et al., 2011). The crests of most of the larger structural-amplitude (km-scale) anticlines are composed of relatively older and more indurated strata (Rohrmann et al., 2013) and form topographic highs with ~100 – 250 m of relief (Figs. 5 and 6). Intervening, lower-elevation and closed topographic depressions expose synclinally folded bedding in younger sedimentary rocks and are occupied by ephemeral playas and saline lakes at their lowest elevations (Chen and Bowler, 1986; Zhao and Huang, 2021) (Fig. 4).

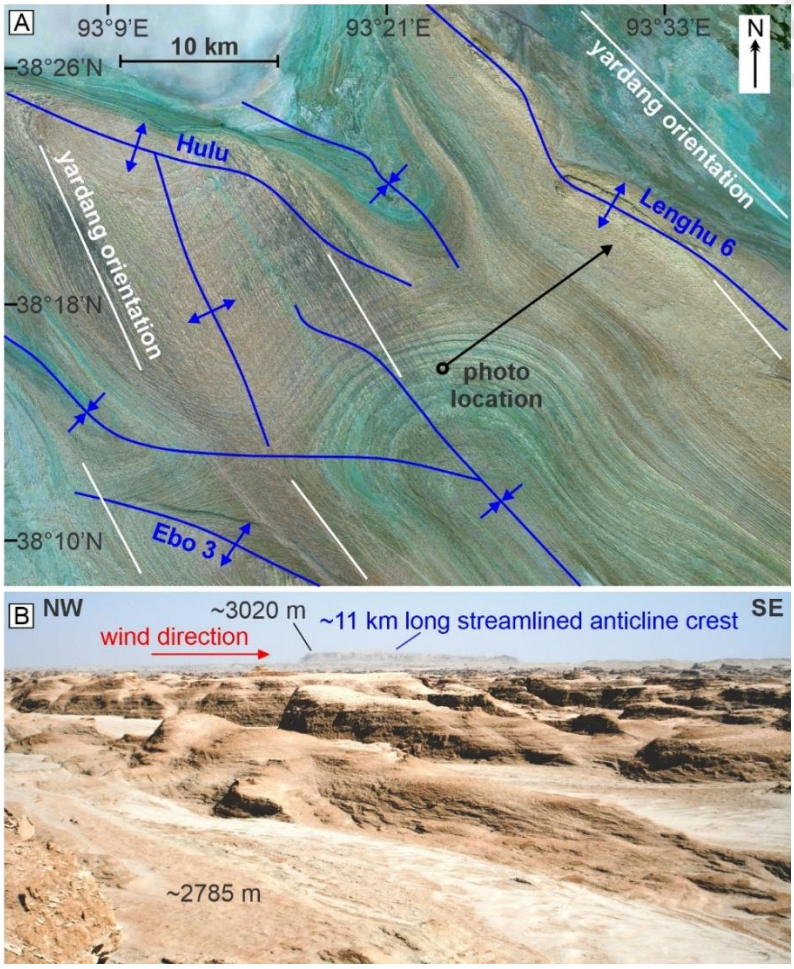

Figure 6. *(A) Satellite image of a part of the northeastern Qaidam fold belt, with axial traces of anticlines and synclines indicated. The faint linear streaks (parallel to the white lines) are expressions of yardang trends. Folded sedimentary rocks have been eroded and blown away,*

even from above syncline axes. (B) View to northeast of the crest of Lenghu 6 anticline. The yardangs in the foreground are sculpted in mid-Pleistocene lacustrine strata, whereas the anticline ridge crest in the distance is composed of more indurated upper Miocene fluvial strata. The anticline has >2 km of structural relief, but exhibits <250 m of topographic relief; the difference is the thickness of sedimentary rock that has been eroded from the crest of the anticline. Intriguingly, the axis- and wind-parallel topographic profile of the ~11-km-long anticline ridge crest in the background is streamlined like a yardang.

Erosion is required to exhume folded sedimentary rocks to the surface. The magnitude of erosion can be estimated by constructing geological cross-sections and projecting sedimentary bedding dip angles measured at the surface and depicted on geological maps, and imaged in seismic-reflection profiles, above the erosion surface (Fig. 7). This exercise is straightforward for sedimentary units exposed in the cores of anticlines that pre-date folding, as demonstrated by their uniformity in bed thickness across a particular fold. More subjective in interpretation is upward extrapolation of growth strata—sedimentary rocks that were deposited coeval with deformation (Suppe et al., 1992). Anticlinal growth strata are distinguished by decreases in bed thickness and dip angle towards anticline crests where there is less accommodation for sediment, or which have become erosive due to topographic relief. For eroded growth strata, the magnitude of thinning is uncertain, but the gentle to open tightness of Qaidam anticlines precludes drastic thinning at the kilometer scale. We maintain that even the most conservative cross-sections in terms of minimizing the area of strata above the erosion surface will not change the conclusion that a thickness of hundreds to thousands of meters of strata has been eroded from the crests of major Qaidam anticlines (Fig. 7).

Erosion and sediment transport may be attributable to liquid water, ice, and wind. Alluvial fans rim the margins of the Qaidam Basin, but they deliver sediment into proximal down-slope lake and playa basins (Fig. 4). There are no fluvial drainage networks in the interior of the Qaidam fold belt (Figs. 4-6). Glaciers, along with evidence for glacial erosion such as U-shaped valleys and moraines, are localized to the highest-elevation parts of adjacent mountain ranges (Li et al., 2019). In contrast, there is ubiquitous evidence for erosion by wind and wind-blown sediment, and the Qaidam Basin has become an increasingly popular laboratory to investigate wind-dominated landscapes and processes on Earth and as an analog for those on

other planetary bodies (Rubin and Hesp, 2009; Anglés and Li, 2017; Xiao et al., 2017; Wang et al., 2018; Xiao, 2021).

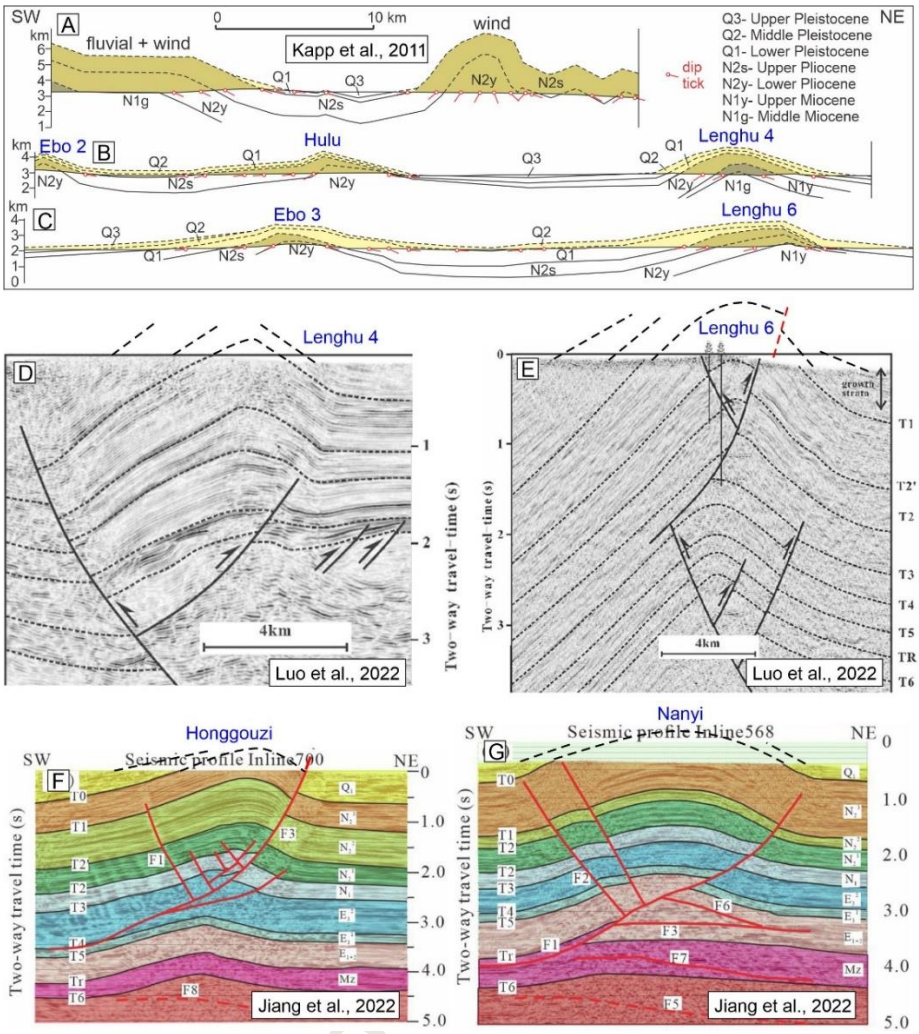

Figure 7. *Cross-sectional interpretations of Qaidam folds. Locations of section lines are indicated in Figure 5. (A)-(C): Geological cross-sections constructed using age and bedding orientation constraints provided from unpublished 1:200,000-scale geological maps (Kapp et al., 2011). Their aim was to estimate how much sedimentary rock was eroded from above the folds (shaded area above topographic profiles). Many synclinal areas are also wind eroded, but where bedding is sub-horizontal or bedding dip data are absent, it is not possible to estimate the magnitude of wind erosion in these regions. (D)-(G): Interpreted seismic reflection profiles across Qaidam anticlines (Jiang et al., 2022; Luo et al., 2022), along with dashed lines projecting bedding measurements above the topographic profiles. For estimates of depth, two-way travel times of 1 s and 2 s corresponds to ~1.3 km depth and ~3 km depth, respectively (Liu*

et al., 2019). To is ~2.8 Ma; T1 is ~8 Ma; T2' is ~15 Ma; interpreted ages of older units are not listed here because they are not relevant for estimating magnitudes of erosion. Growth strata, which are sedimentary rocks that are deposited coeval with deformation and recognized based on lateral bed thickness and dip orientations, have been recognized in T2' through T1 units, but are most prevalent and pronounced in strata above To. A key takeaway is that a thickness of hundreds to thousands of meters of sedimentary rocks has been eroded from above Qaidam anticlines (and all since ~3 Ma; see text for discussion).

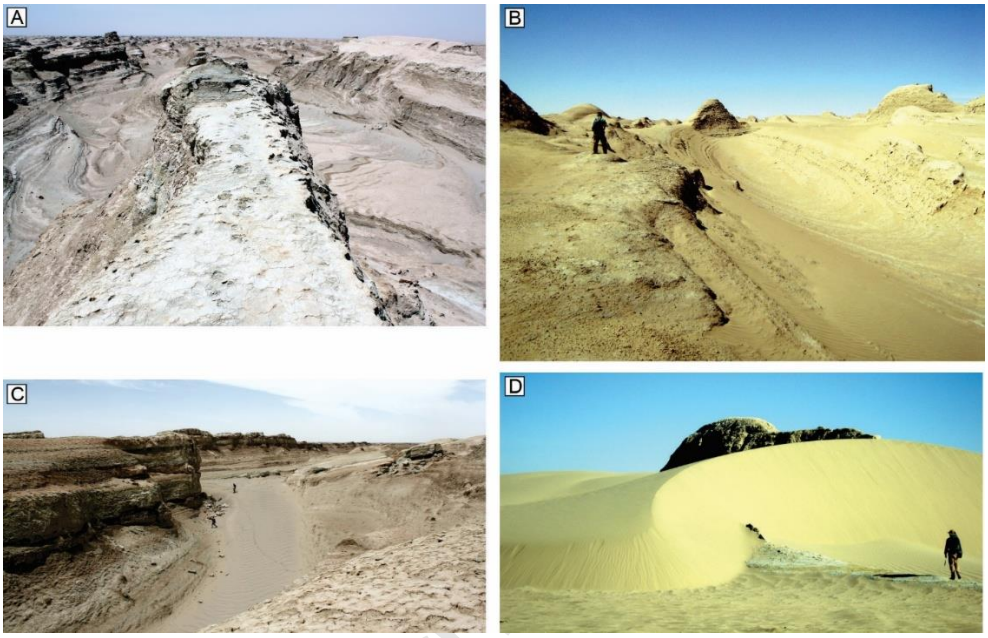

Figure 8. *Field photographs. (A) View standing on the narrow crest of a yardang and looking in the upwind direction. The sedimentary rocks are actively folding but the regional topography has been beveled flat. (B) A wind-scoured trough exposing sedimentary bedding. (C) An inter-yardang corridor floored by rippled sand. Inter-yardang corridors exhibit undulatory topography; they are not relicts of fluvial drainages. Erosion by windblown sand is greatest near the base of the corridors, leading to undercutting and mass wasting. (D) Modern sand dune burying a yardang.*

There are two primary observations that underscore wind as the dominant mechanism of sediment removal from above the Qaidam fold belt. The first is that the folded sedimentary rock has been sculpted into extensive fields of yardangs (Figs. 4 and 6) (Halimov and Fezer, 1989). The second observation is the multitude of closed topographic depressions in the Qaidam fold belt that must have experienced erosion via deflation and up-slope sediment transport to expose

tilted bedding. The closed depressions range from 10- to 100-m-scale inter-yardang scoured corridors in bedrock (Figs. 8A-B), which may include overlying sand ripples (Fig. 8C) and dunes (Fig. 8D), to >10-km-scale deflation depressions (Figs. 5 and 9). An outstanding example of the efficacy of wind erosion is the presence of topographically-inverted anticlines in the southern part of the Qaidam fold belt (Fig. 9). Here, sedimentary bedding defines an en-échelon array of three doubly-plunging NW-SE-trending anticlines. The crests of the anticlines are not characterized by topographic highs, like in most other parts of the Qaidam fold belt, but instead topographic troughs that are ~100 m deep and floored by yardangs. Wind processes have undeniably not only beveled off but have also scoured down into the crests of the anticlines, presumably because younger strata along the anticline limbs are more resistant to wind erosion than the underlying older strata (Fig. 9).

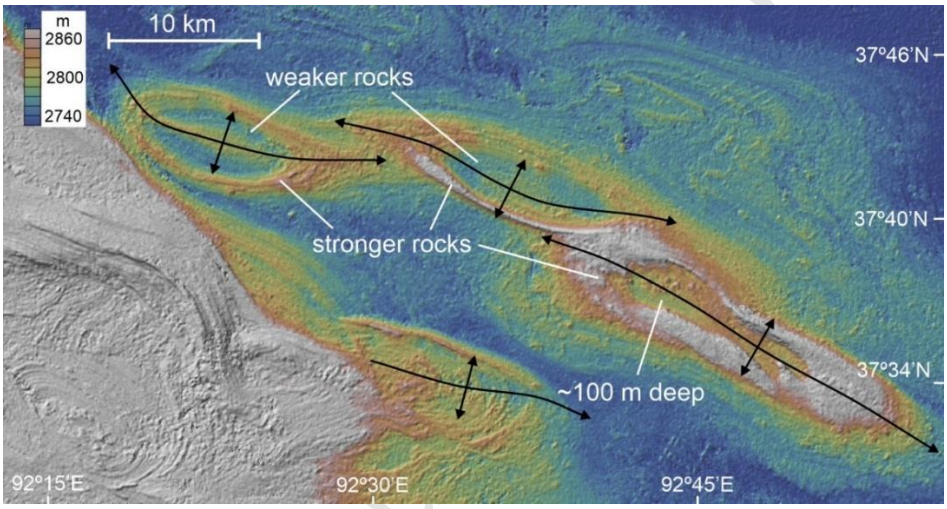

Figure 9. *Shaded relief map (www.geomapapp.org) showing anticlines in the southern Qaidam Basin fold belt that exhibit topographic troughs along their crests and which are floored mostly by wind-eroded bedrock. The only viable transport mechanism to remove sediment from the troughs is wind. Spatially variable magnitudes of wind erosion are attributable to relative erodibility of the folded sedimentary beds. Also note the multitude of closed topographic depressions and their large range of scales.*

Multiple mechanisms contribute to eroding bedrock into sediment in arid regions, including mass wasting, salt weathering, rainsplash and fluvial erosion during rainstorm events (the largest yardangs and bedrock ridges in relatively older and more indurated strata are locally gullied/rilled), expansion-contraction related to changes in temperature and moisture, and chemical weathering, in addition to deflation and abrasion by wind-blown sand (Goudie, 2008;

Laity, 2011). However, wind is the only process that could have ultimately removed sediment from the closed depressions within the exhumed western Qaidam fold belt.

Wind erosion rates over the past ~10-20 ka were estimated for 11 samples collected from Qaidam fold belt sedimentary rocks by measuring the concentrations of cosmogenic-produced beryllium in quartz (Fig. 4) (Rohrmann et al., 2013). Ten of the calculated rates range from 0.06 to 0.17 mm/yr with an average and standard deviation of 0.12 ± 0.03 mm/yr, excluding one outlier with a rate of 0.4 mm/yr. These rates should be considered minima for two reasons. First, the samples were collected from older (Miocene – Pliocene) strata near the crests of anticlines to avoid complications of beryllium inheritance in younger strata. These Miocene – Pliocene strata are more indurated and thus less susceptible to wind erosion than spatially more widespread Pleistocene strata in the fold belt. Second, the samples are from or near the tops of yardangs or strike-parallel bedrock ridges (Rohrmann et al., 2013). Higher erosion rates would be expected in inter-yardang troughs where abrasion by wind-blown sediment is maximized (at heights < ~1 m from the surface) (Pelletier et al., 2018). A sample of Paleozoic granite collected along the northernmost margin of the basin yielded an erosion rate of 0.003 mm/yr, demonstrating that friable sedimentary rocks are approximately two orders of magnitude more erodible by wind than crystalline bedrock (Rohrmann et al., 2013).

2.2. Geomorphically-effective wind regime

We have continued to expand on initial geomorphologic and geologic mapping of the Qaidam fold belt (Kapp et al., 2011) as high-resolution satellite imagery has become increasingly available. Our goals were to illuminate the geomorphically-effective surface wind pattern across the Qaidam fold belt, the extent to which surface winds are deflected around topographically-higher anticline crests, and potential relationships between local wind directions and anticline axial trace orientations. Initial mapping focused on the orientations of the most geomorphically-prominent yardang trends. Tens of thousands of yardang trends were mapped in Google Earth and then transferred to the shaded relief map (Fig. 10) where red lines were drawn to depict visually averaged orientations. This is a qualitative exercise as yardang orientations are in many places curvilinear and/or vary over distances of <100 m (Fig. 11).

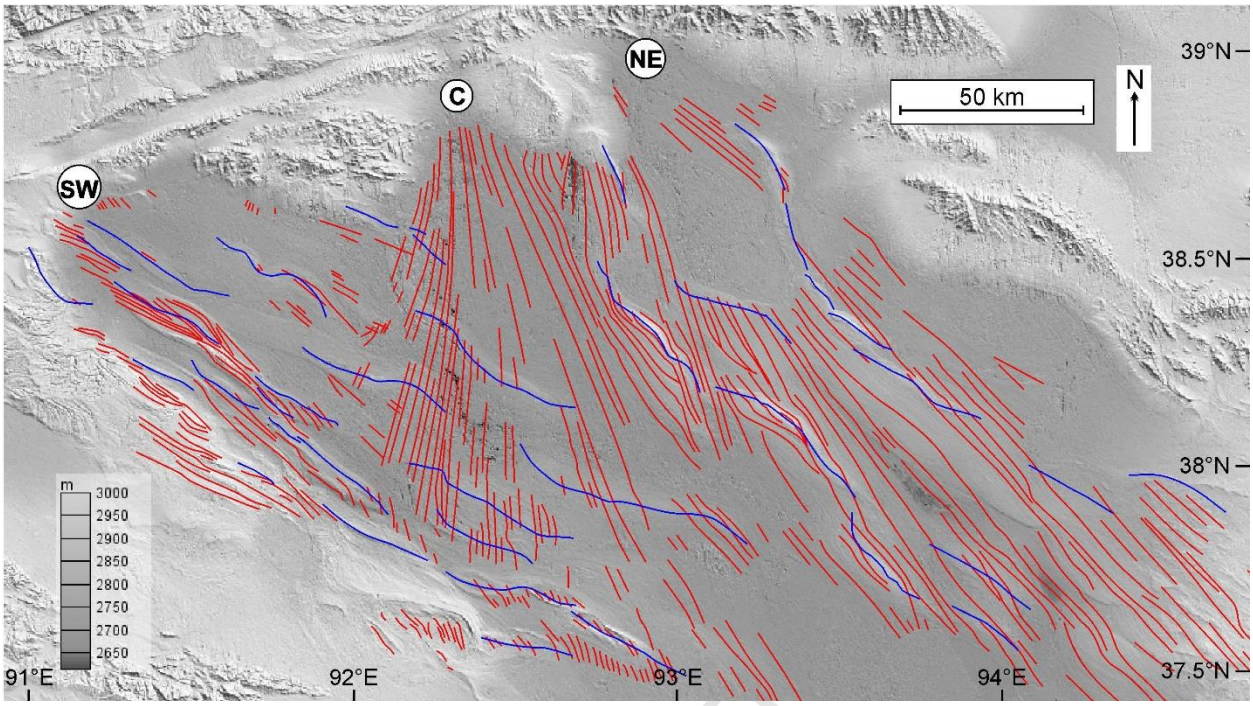

Figure 10. *Shaded relief map (www.geomapapp.org) showing axial traces of anticlines (blue lines) and geomorphically-effective wind directions (red lines) based on the average orientations of the most prominent yardangs in the modern landscape. Yardangs are absent or scarce in the regions where no red lines are depicted, primarily within modern playa depressions. The mapping reveals three topographic gaps in the Altyn Mountains where strong surface winds appear to enter the northeastern (NE), central (C), and southwestern (SW) parts of the northwestern Qaidam Basin.*

The mapping supports the presence of three distinct near-surface wind regimes, apparently controlled by where winds enter the northwestern Qaidam Basin through topographic gaps in the Altyn Mountains (Halimov and Fezer, 1989; Kapp et al., 2011; Rohrmann et al., 2013): dominantly northwesterly winds in the northeast (NE); more northerly winds in the central (C) northwestern margin of the basin that diverge southward; and northwesterly winds in the southwest (SW) (Fig. 10). In the central and eastern Qaidam Basin, geomorphically-effective wind directions generally parallel the long axis of the basin (Fig. 2). Wind patterns show moderate deflections around and between the topographically higher relief anticlines, demonstrating that topography influences local wind patterns. We address the local differences in wind direction and anticline axial trace orientation, and their potential significance, in a subsequent section.

The wind pattern determined from the most prominent yardang trends (Fig. 10) is consistent with the modern surface wind regime as indicated by measurements at sparse meteorological stations (Hu et al., 2017) and orientations of modern sand dunes, sand ripples, and wind streaks (Kapp et al., 2011 and this study). However, the strength of modern interglacial (Holocene) winds and/or the frequency of strong windstorms, and magnitude of Holocene wind erosion in the Qaidam, are likely much less than during past glacial periods (McGee et al., 2010; Kapp et al., 2011; Wu et al., 2019). Windstorms occur in the Qaidam Basin today (Qiang et al., 2010) but are less frequent and severe than in other parts of China such as in the Gobi and Taklamakan deserts (Sun et al., 2001). This observation has been used to suggest that the Qaidam Basin was not a major source of Chinese Loess Plateau strata. Holocene loess deposits have locally accumulated in the Qaidam Basin, but pre-Holocene loess is rare, further suggesting (1) a weaker Holocene wind regime favorable for loess accumulation, and (2) that any pre-Holocene loess was effectively eroded from the basin during more arid and stronger-wind-regime glacial periods (Bowler et al., 1987). These findings for the Qaidam Basin are consistent with the framework that the preservation of loess in the geological record is the exception rather than the rule in most settings (Meijer and van der Meulen, 2023).

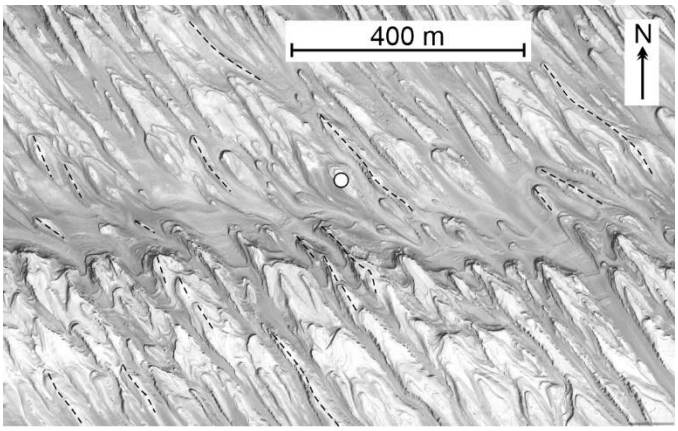

Figure 11. *GoogleEarth image showing spatial variations in yardang orientations. Our mapping in Figure 10 attempted to capture the average trends of the most prominent yardangs, which are better defined upon zooming out in Google Earth. White-filled circle indicates location of latitude and longitude: 38.27922 °N; 93.41159 °E.*

2.3. Qaidam megalake during the Last Interglacial Period?

Critical for understanding the history of Qaidam Basin wind erosion is knowledge of when it was most recently wetter and undergoing widespread sediment accumulation. Chen and Bowler (1986) argued for a former Qaidam megalake based on remnants of shorelines and marginal lake deposits at an elevation of ~2800 m (Fig. 12). This lake highstand was initially thought to be at ~40 ka (Chen and Bowler, 1986), but subsequent dating of sedimentary records suggest that it occurred during Marine Isotope Stage 5 (MIS 5; ~130 – 80 ka). For example, the "Shell Bar" deposit in the eastern Qaidam Basin, appreciated for its fresh-water clam shells, was revised from ≤40 ka (Bowler et al., 1986; Zhang et al., 2008) to ~115 – 100 ka (Lai et al., 2014). Playa salt crust in synclinal parts of the northwestern Qaidam fold belt is dated to ~100 ka (Han et al., 2014b), whereas fluvial strata in the southwestern-most Qaidam fold belt were deposited at ~105 ka (Wu et al., 2019). Relatively high lake levels may have persisted, at least in the eastern Qaidam Basin, until ~80 ka (Fan et al., 2012). The MIS 5 timing is also in accord with better established dates of lake highstands across the Tibetan Plateau (Yu et al., 2019).

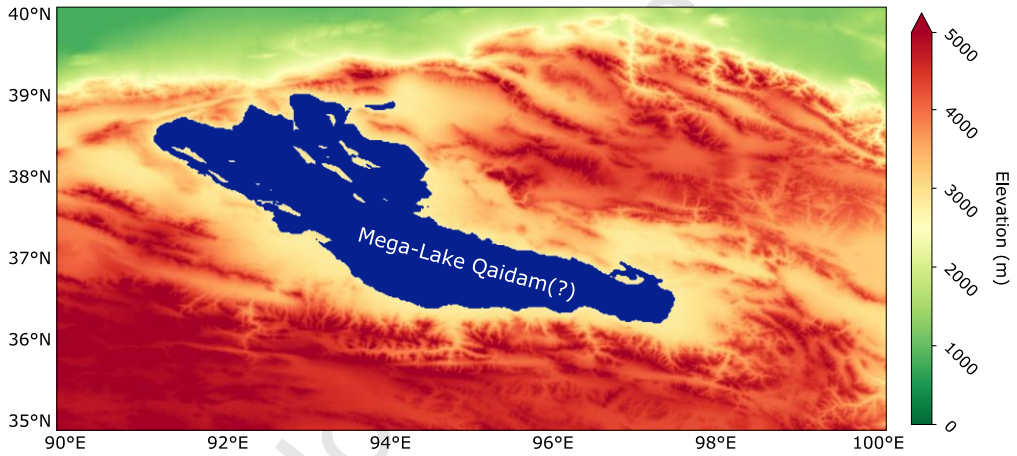

Figure 12. *Digital elevation model showing the approximate extent of a megalake in the Qaidam Basin with a lake surface elevation at 2800 m. Available data suggest that this highstand may have occurred during Marine Isotope Stage 5 (~130 – 80 ka)*

It seems extraordinary that a lake as large as the third largest lake on Earth today (Lake Huron, one of the North American Great Lakes) occupied the Qaidam Basin during MIS 5, especially given the hyperaridity in today's Holocene interglacial climate. This motivated us to map lake shorelines and remnant lake and marginal lake alluvial-fluvial strata in Google Earth satellite imagery. The shorelines and strata are widely scattered and only locally preserved as isolated remnants that have fortuitously not been sculpted into yardangs or entirely blown away

(Fig. 13). The difference between the highest elevation shorelines and sedimentary strata (blue circles; Fig. 13) and modern base level of adjacent sub-basins (white circles; Fig. 13) range from ~85 m to ~140 m and provide approximate water paleodepths during this lake highstand (Fig. 13). While we confirm that a lake of large spatial extent occupied the Qaidam Basin, likely during MIS 5, the paleolake depth estimates should probably be considered maxima. This is because the lowest-elevation depressions may have undergone base-level drop by wind scour since the highstand whereas the basin margins and anticline crests likely experienced surface uplift due to rock deformation. Some marginal lake deposits are preserved at elevations up to ~2900 m (Fig. 13). These strata could potentially be remnant from older interglacial periods (~200-400 ka) for which some Qaidam Basin strata has been dated (Mischke et al., 2010; Ding et al., 2021) and are at higher elevations because of tectonic surface uplift since their deposition.

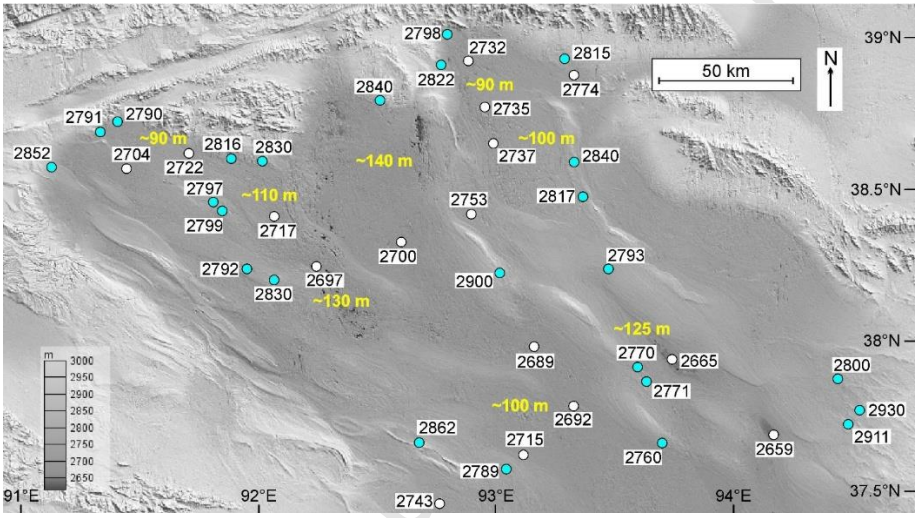

Figure 13. *Modern elevations of local base level (white circles) and remnants of shorelines and sub-horizontal lake and lake-marginal alluvial-fluvial deposits sitting above angular unconformities (blue circles). The yellow numbers are the approximate difference between the two, providing estimates for paleolake depths.*

Remnant lake and lake-marginal alluvial-fluvial deposits provide an opportunity to quantify wind erosion rates since their deposition. For example, ~105 ka fluvial strata along the northwestern margin of the Qaidam fold belt are locally preserved at elevations ~26 m higher than adjacent wind-scoured valleys in Miocene bedrock, yielding a time-averaged erosion rate of ~0.25 mm/yr (Wu et al., 2019). There are many other areas in the Qaidam Basin where this approach could be employed (near the blue circles indicated in Fig. 13, among other places). Our preliminary analysis suggests that remnant lake and marginal lake strata generally sit at

elevations of 20-40 m higher than intervening wind-eroded topographic depressions. Under the major assumption that these strata are ~100 ka, erosion rates of 0.2 – 0.4 mm/yr are implicated, in line with the estimate of Wu et al. (2019). Additional geochronology and 3-D topographic analysis of these remnant, non-eroded sedimentary rocks in the Qaidam fold belt have potential to provide estimates of the volume of strata that has been wind eroded since their deposition.

While we maintain that the presence of a megalake in the Qaidam Basin during MIS 5 is plausible, additional robust geochronology on upper Pleistocene strata is warranted to confirm this as well as to provide more confident estimates of wind erosion rates. Additionally, future research is warranted to address how large and deep late Pleistocene lakes might have developed within the Qaidam Basin when strongly evaporative saline lakes and playas generally prevailed as in the modern climate (Cai et al., 2012; Han et al., 2014a).

2.4. Glacial-interglacial cyclicity and paleoyardangs

If all wind erosion of the Qaidam fold belt occurred since the beginning of the Last Glacial Period, this would require unrealistically high erosion rates from above Qaidam anticline crests. For example, removal of ~1 km of strata from the crests during the past ~100 ka would suggest an erosion rate of ~10 mm/yr, higher than those in the highest-relief, tectonically active mountain belts on Earth (Montgomery and Brandon, 2002). Conversely, if glacial wind erosion was as significant as it was during the Last Glacial Period throughout the Pleistocene, this raises the question of how parts of the exhumed Qaidam fold belt include thick (locally >1 km) accumulations of Pleistocene strata (Fig. 7). To reconcile these issues, it was proposed that the Qaidam Basin experienced alternating episodes of wind erosion and sediment accumulation in phase with the alternating loess – paleosol stratigraphy of the Loess Plateau, with wind erosion being dominant during past glacial periods (Kapp et al., 2011). Where there is net accumulation of Pleistocene strata, the thickness of sediment accumulated during interglacial periods exceeded the thickness of strata eroded during intervening glacial periods (Fig. 14). An implication of this hypothesis is that estimates of the amount of sediment eroded from the top of the Qaidam fold belt from geological cross-sections are underestimates as they do not account for strata that were deposited and then subsequently eroded during interglacial – glacial cycles.

A prediction of alternating interglacial sediment accumulation and glacial wind erosion is that there should be wind-eroded intraformational unconformities, including paleoyardangs,

within Qaidam Basin stratigraphy that has been exhumed to the surface by folding and erosion (Fig. 14). Previous evidence of intraformational unconformities include the periodic presence of salt crusts, deflation lag and windstorm deposits, and paleopans within otherwise dominantly lacustrine Pliocene – Pleistocene strata (Kapp et al., 2011; Heermance et al., 2013). Recent feldspar luminescence studies have confirmed the presence of glacial period depositional hiatuses of up to ~100 ka, interpreted to be wind-eroded unconformities, within lacustrine-playa strata within the eastern Qaidam Basin (Ding et al., 2024). Buttress unconformities in ~2.4 Ma Qaidam fold belt strata have been interpreted as paleoyardangs, although the long-axis orientations of the buried ridges are different from those of the yardangs in the modern landscape (Heermance et al., 2013). We provide less ambiguous examples of paleoyardangs later in this section that also have long-axis orientations that are significantly different than those of yardangs that dominate the modern landscape.

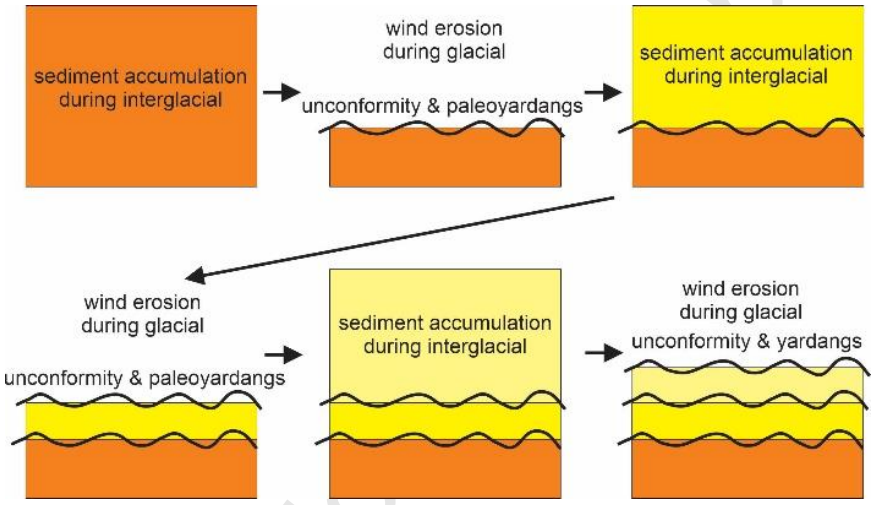

Figure 14. *Cross-sectional cartoon illustrating how strata can accumulate despite periods of significant wind erosion. The thickness of sediment accumulated during interglacial periods exceeded the thickness of sediment eroded during glacial periods. This history predicts that Qaidam fold belt strata should exhibit evidence of intraformational wind-eroded unconformities, including paleoyardangs.*

Inspection of the modern Qaidam fold belt provides insight into how yardangs might be preserved in the stratigraphic record. Partially submerged yardangs are common in Qaidam Basin saline lakes (Fig. 15A) (Zhao and Huang, 2021) where presumably Holocene lake sediment is buttressing up against the bases of the yardangs. If lake-level rise and lacustrine sedimentation were to continue, the yardang ridges would get buried and be bound by buttress

unconformities (Heermance et al., 2013). We documented an example along the southwestern crest of the Lenghu 6 anticline (Fig. 5) where remnants of undated but much younger (given their shallower bedding dip) lacustrine strata have buttressed against more steeply dipping and wind-eroded Miocene strata (Fig. 15B). The preservation potential of the younger lacustrine strata is low given their susceptibility to future wind erosion. It is likely that many modern yardangs have been at least partially buried one or more times and subsequently re-exhumed, and thus *sensu-stricto* are paleoyardangs.

Yardangs could be partially buried or completely buried, resulting in horizontal lacustrine flooding sequences above fields of paleoyardangs. In fact, this is predicted if there is to be net accumulation of Pleistocene strata: generally thick and continuous lacustrine sequences during interglacials, followed by lake desiccation (resulting in sedimentary structures like mud cracks and evaporative lacustrine facies), and then wind erosion during glacial periods, scouring the underlying lacustrine and marginal lacustrine strata. If yardangs are formed, those more proximal to subsequent interglacial lakes would get flooded and preserved beneath more thick and continuous lacustrine sequences. Potentially good examples of this are exposed on the southwestern flank of the northwesternmost Hulu anticline (Fig. 5) and adjacent to a synclinal playa, which we would expect to fill with a lake during interglacial periods and flood yardangs sculpted during prior glacial periods. In the example Google Earth image (Fig. 15C), strata that have been sculpted into ~northwest-trending yardangs are dipping very gently to the southwest. We interpret a paleoyardang field (#1) in the northeast of the image (Fig. 15C). The southwesternmost yardangs show overlying strata buttressing onto them (white dotted line on Fig. 15C), and stratigraphically above this are laterally continuous layers of lacustrine strata. Then there is a younger interpreted paleoyardang field to the southwest (#2) (Fig. 15C). Again, there is evidence of overlying lacustrine strata buttressing against the yardang ridges (white dotted lines) and then the yardangs are completely buried by non-wind-eroded lacustrine strata (yellow dashed line) (Fig. 15C). We emphasize *potentially* good examples because key relationships like the buttress unconformities need to be confirmed in the field. One could argue that paleoyardang field #1 terminates on its southwestern margin because the sedimentary facies of the overlying strata may not be favorable to being sculpted into yardangs and/or that paleoyardang field #2 terminates to the southwest because wind scouring has not yet progressed through the overlying

non-eroded lake strata (Fig. 15C). Regardless of the ambiguity and need for field documentation, we hope our lines of reasoning help guide future investigations.

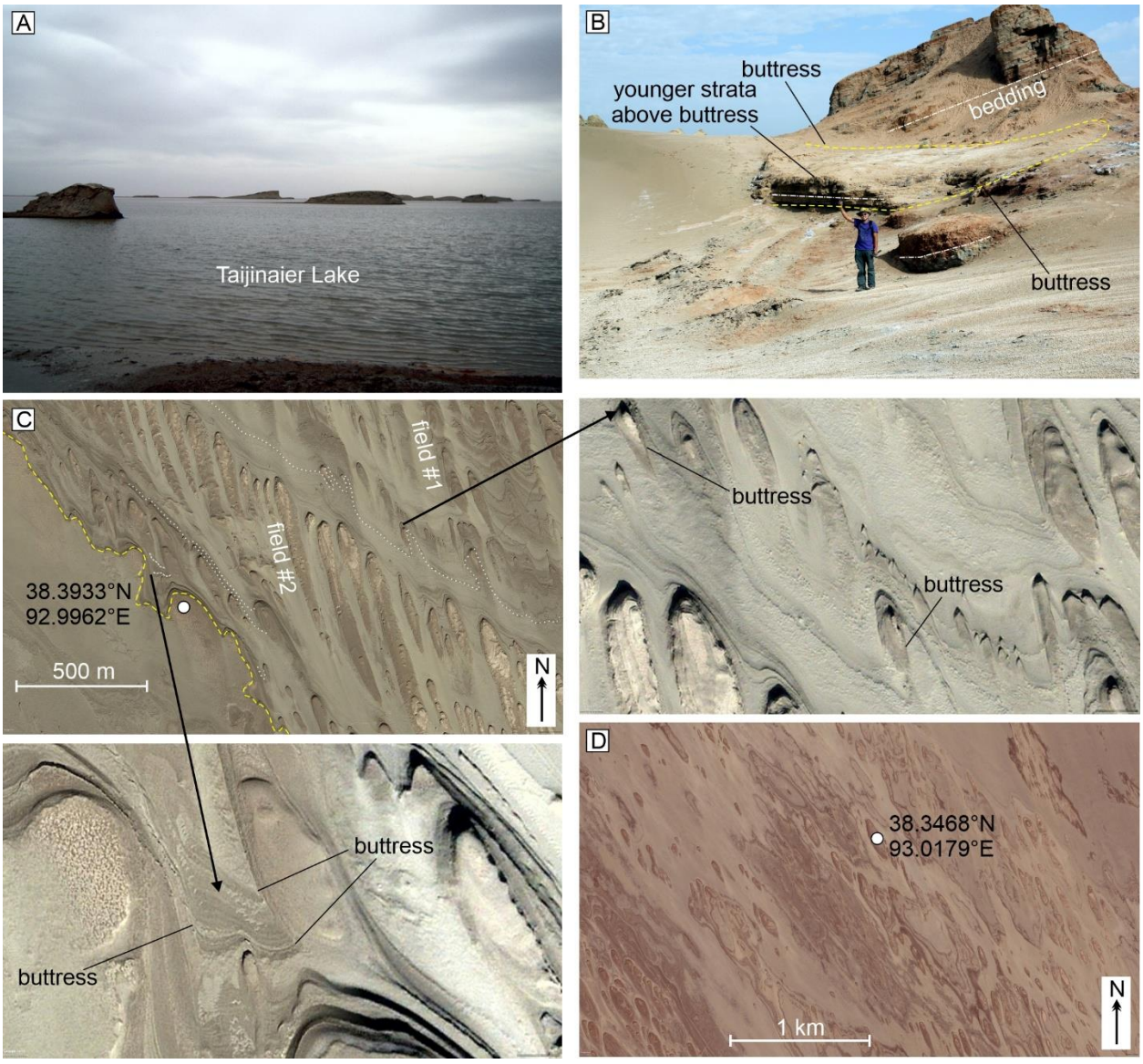

Figure 15. *(A) Partially-submerged yardangs in a western Qaidam Basin saline lake. (B) Photo taken near the crest of Lenghu 6 anticline (Fig. 6) of a buttress unconformity between moderately-dipping and reddish-colored Miocene strata below and more shallow-dipping and lighter-colored lacustrine strata above. The age of the younger lacustrine strata is unknown, but their presence demonstrates that the yardang landform in the background was at least partially buried in the past. (C) Google Earth image of potential paleoyardang fields bounded by unconformities (white dotted lines). The yellow dashed line is interpreted to be a surface above which paleoyardang fields were buried beneath by younger sediment to the southwest. Zoomed-*

in images of the interpreted buttress unconformities are shown to the right and below. (D) Google Earth image of exhumed paleoyardangs that were likely partially buried in a lake setting similar to that shown in Fig. 15A. White circles indicate longitude and latitude localities.

A more convincing, and in our view unambiguous example of exhumed paleoyardang fields in the Qaidam fold belt is where sedimentary bedding is not regionally continuous (Fig. 15D). Instead, the bedding shows elongate elliptical patterns where strata have filled inter-paleoyardang troughs (and bound paleoyardang ridges). These types of paleoyardang fields would be expected to develop when the amount of alternating sediment accumulation and wind erosion are nearly equal in a region, with slight net sediment accumulation required for preservation. A modern analog setting for this paleoyardang field is where yardangs are partially submerged in lakes (Fig. 15A).

We identified another class of paleoyardangs in the Qaidam fold belt. They are distinct and readily identifiable in imagery because their orientations differ from those of the yardangs that dominate the modern landscape and henceforth referred to as oddly-oriented paleoyardangs. A good example of oddly-oriented paleoyardangs is found along the eastern flank of the Heiliang anticline (Fig. 5) where strata dip very gently to the northeast (Fig. 16A). Oddly-oriented paleoyardangs are oriented northeast-southwest in the southwestern part of the image (Fig. 16A). They are overlain by strata to the northeast that are sculpted into NW-SE-trending yardangs, similar in orientation to those that dominate the modern landscape in this region.

The oddly-oriented paleoyardangs share similar characteristics in all places where they were identified. They exhibit long aspect ratios (>10:1), narrow spacing (<40 m and typically 5 – 15 m), and low amplitudes (below digital elevation model resolution). The oddly-oriented paleoyardangs are confined to stratigraphic intervals that are generally light-colored (Fig. 16) and inferred to consist of erosionally-resistant salt playa facies. The relative strength of the oddly-oriented paleoyardangs explains why they have not been completely overprinted by the more geomorphically-dominant wind regime, although there are many examples of partial overprinting (Fig. 16B). Confinement of the paleoyardangs to individual stratigraphic intervals suggests that they formed shortly after deposition when they were more friable. A modern setting analog of these paleoyardangs may be near the central topographic gap in the Altyn Mountains (Fig. 10) where north-northwesterly winds have sculpted long-aspect-ratio yardangs into ~100 ka salt playa strata (Fig. 16C) (Han et al., 2014b).

Paleoyardangs were identified in strata as old as late Pliocene in age in the core of the Heiliang anticline (Fig. 5) and which are offset by faults with hundreds of meters of stratigraphic separation, consistent with their antiquity (Fig. 16D). The crest of the Heiliang anticline has been topographically inverted by wind scour, with lower elevations along its crest than along its limbs. Remnants of non-wind-eroded lake shoreline deposits are present along its northeastern limb at an elevation of ~2790 m (Fig. 16D; corresponding to the Qaidam megalake highstand). We infer that lacustrine strata were deposited unconformably on top of the Pliocene strata during a late Pleistocene interglacial period and subsequently wind eroded, such that the remnants of the upper Pleistocene strata are sculpted into normally-oriented northwest-southeast trending yardangs along the crest of the Heiliang anticline (Fig. 16D).

During our initial mapping of the oddly-oriented paleoyardangs, we hypothesized that they would be restricted to upper Pliocene to lower Pleistocene strata such that a change in the wind regime could be attributed to tectonically-driven changes in topography. After extensive remote mapping, however, we identified oddly-oriented paleoyardangs throughout the late Pliocene to late Pleistocene stratigraphy, including within lacustrine strata remnant from a recent interglacial period (Fig. 16E; MIS5?).

The orientations of the oddly-oriented paleoyardangs vary locally, but generally by less than ~20° in azimuth and in a nonsystematic manner (Fig. 16D). Overall, the orientations of the oddly-oriented paleoyardangs are sufficiently similar throughout time in the stratigraphic record and space across the basin to make a map of visually-averaged orientations (Fig. 17, solid yellow and green lines). Regional extrapolation of these, in turn, yields a reasonable near-surface wind regime during which more westerly winds entered through the southwestern topographic gap in the Altyn Mountains, and more easterly winds entered through the central topographic gap (Fig. 17; dashed yellow and green lines). It remains to be determined when during the glacial-interglacial cycles this wind regime may have dominated.

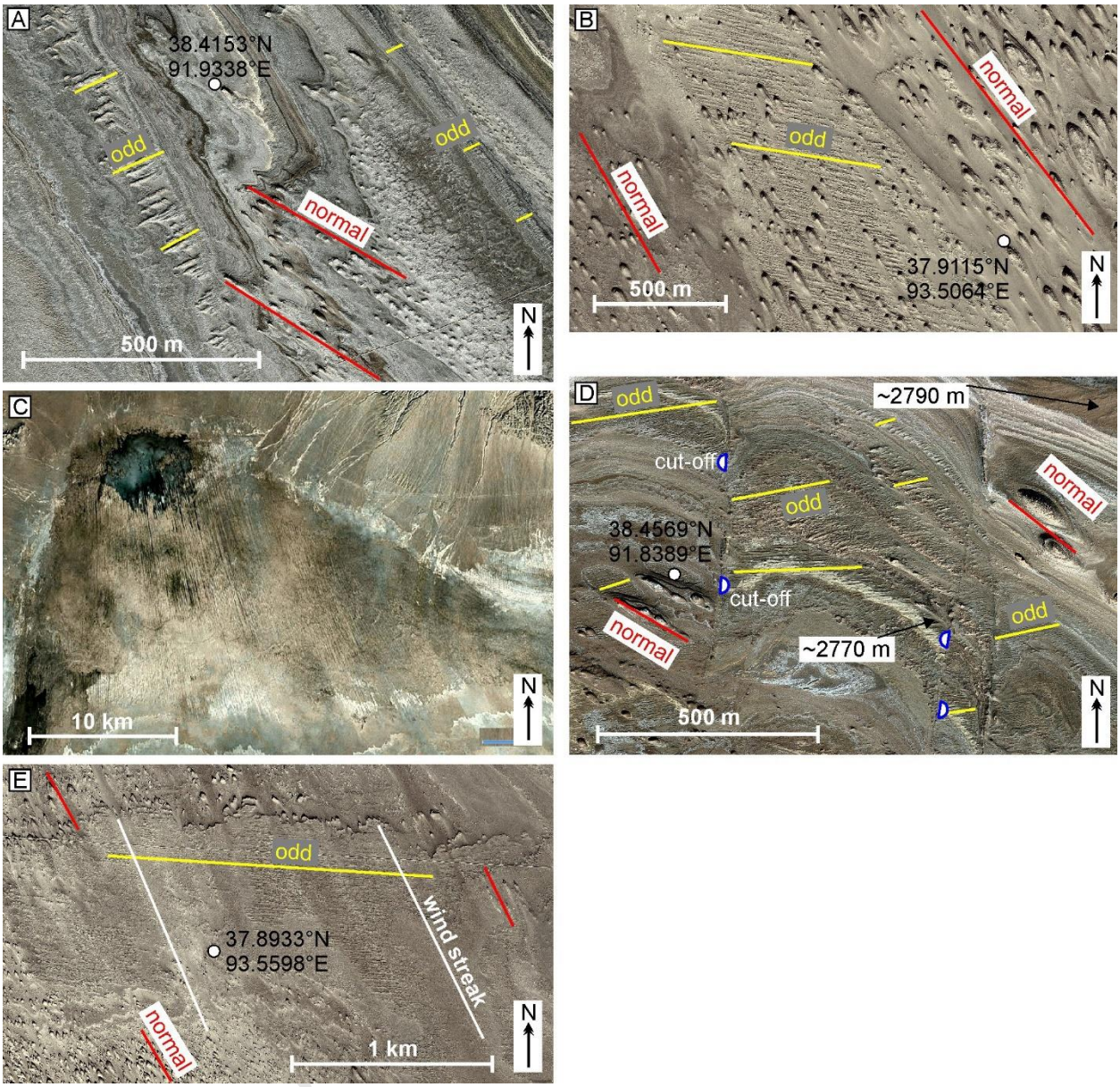

Figure 16. *Google Earth images of paleoyardangs (indicated by the yellow lines and labeled as odd) that are oriented differently than the long-axis trends of the more prominent yardang fields (indicated by the red lines and labeled as normal) in the western Qaidam Basin. (A) Pleistocene strata along the northeastern limb of the Heiliang anticline (Fig. 5). (B) Typical expression of oddly-oriented paleoyardangs exposed between the southern tip of the Ebo 3 anticline and the northern tip of the Yahu anticline (Fig. 5). (C) Modern setting analog for the formation of the oddly-oriented paleoyardangs where long-axis and closely-spaced yardangs have developed within ~100 ka playa salt crust (Han et al., 2014b) in the northwestern-most Qaidam Basin. (D) Faulted paleoyardangs in upper Pliocene strata along the topographically inverted crest of the*

Heiliang anticline. In the northeastern-most part of the image are flat-laying and non-wind-eroded strata at relatively higher elevations (~2790 m) and which exhibit shorelines. These strata remnants may have been deposited during the MIS 5(?) megalake highstand and likely buried the crest of the Heiliang anticline but have since been blown away. (E) Oddly-oriented paleoyardangs within flat-lying strata. The orientations of the wind streaks (white lines) are reliable indicators for the modern geomorphically-effective wind direction.

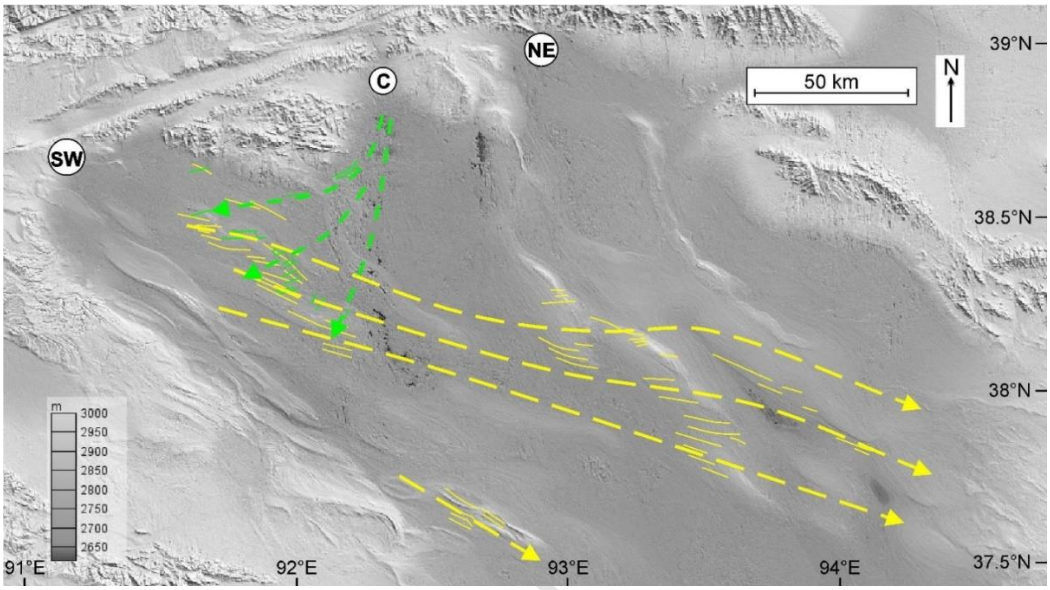

Figure 17. *Solid yellow and green lines indicate visually-averaged orientations of oddly-oriented paleoyardangs where they are readily identifiable and mapped in imagery (at thousands of individual localities where solid lines are indicated). Dashed yellow and green lines are the interpreted surface wind regimes in which the oddly-oriented paleoyardangs formed. The paleoyardangs (of similar orientation in a given region) are present in upper Pliocene to upper Pleistocene strata, demonstrating that these "odd" wind regimes were intermittently active during the past few million years, although precisely when remains to be determined. They do not match the modern wind regime and unlikely represent glacial maxima wind regimes when the larger and more prominent yardang fields likely formed. SW, southwestern; C, central; and NE, northeastern topographic gaps.*

2.5. Pliocene – Quaternary history of aridification, fold growth, and wind erosion

The Qaidam fold belt offers a unique laboratory for investigating potential linkages among rock deformation, surface processes, and climate. Here we review the Pliocene – Quaternary history of climate change and fold belt development in the Qaidam Basin and discuss

its implications for the history of wind erosion and its potential positive feedback with rock deformation.

The Neogene stratigraphy of the Qaidam Basin holds clues to its surficial evolution from a relatively warm and wet environment during the early Miocene to an arid setting by the late Pliocene (Dettman et al., 2003; Miao et al., 2011; Heermance et al., 2013; Zhuang et al., 2014). The western Qaidam Basin was arid by ~3.9 Ma (Su et al., 2024), but aridification began to intensify at ~3 Ma as evidenced by an abrupt shift in lacustrine carbonate stable isotope values (Heermance et al., 2013; Su et al., 2024), initiation of evaporite deposition (Wang et al., 2013), the disappearance of fish fossils (Wang et al., 2007), an estimated order of magnitude decline in precipitation based on palynology and carbonate-silicate geochemistry (Schwarz et al., 2022), and the presence of paleoyardangs in upper Pliocene strata (this study). Aridification generally intensified throughout the Pleistocene (Rieser et al., 2009; Heermance et al., 2013; Yang et al., 2020b) with a punctuated phase of less arid conditions between ~1.9 and 1.2 Ma (Cai et al., 2012; Herb et al., 2015) and accelerated aridification since ~0.6 Ma (Cai et al., 2012; Han et al., 2014a). Superimposed on this long-term Pliocene – Pleistocene drying trend are the wetter and drier interglacial and glacial periods, respectively (Heermance et al., 2013; Yang et al., 2017). The climate evolution of the Qaidam Basin thus broadly mimics that archived in stratigraphic records of the Chinese Loess Plateau (An, 2000; Porter, 2007) and globally (Lisiecki and Raymo, 2005; Westerhold et al., 2020).

Seismic-reflection profiling of the petroliferous Qaidam Basin has significantly illuminated its Cenozoic deformation history. Shortening initiated locally in the Qaidam fold belt during the early Cenozoic (Yin et al., 2008; Cheng et al., 2019; Cheng et al., 2021) and became more widespread at ~15 Ma (Mao et al., 2016; Liu et al., 2019; Huang et al., 2021; Luo et al., 2022). However, the rate and spatial distribution of shortening increased markedly during late Pliocene – Quaternary time (Zhou et al., 2006; Wei et al., 2016; Bao et al., 2017; Jiang et al., 2022). Deposition of growth strata associated with the Lenghu 6 anticline began at ~3 Ma (Heermance et al., 2013). The crests of the Dafengshan and Jianshan anticlines (Fig. 5) were uplifted above lake level, as determined by offlapping growth strata, beginning at ~3 Ma and ~1.6 Ma, respectively (Lu et al., 2015; Zhang et al., 2020d). As the Qaidam fold belt grew during Miocene – Quaternary time, the larger depocenters migrated to the southeast toward the central

part of the Qaidam Basin (Meng and Fang, 2008; Yin et al., 2008; Bao et al., 2017; Cheng et al., 2021).

The continuity of lower Pliocene lacustrine strata across most of the Qaidam Basin suggests that erosional exhumation of the fold belt occurred after ~3 Ma (Liu et al., 1998; Meng and Fang, 2008; Yin et al., 2008; Kapp et al., 2011; Bao et al., 2017). Removal of hundreds of meters of strata, and locally up to ~3 km above the largest-amplitude folds since ~3 Ma (Fig. 7) suggests long-term erosion rates on the order of ~0.1 to 1 mm/yr, with erosion being inactive in places of sediment accumulation during interglacial periods and maximum in places that were subaerial during glacial wind erosion. The spatial distribution and magnitude of glacial wind erosion throughout late Pliocene – Pleistocene time are unknown, but it seems reasonable to speculate that they generally increased as aridification, lake desiccation, fold growth (uplifting rocks above lake levels / groundwater tables), and the intensity of glacial climate intervals amplified. This is consistent with the widespread preservation of lower Pleistocene strata in the Qaidam fold belt compared to the modern setting where only localized remnants of Last Interglacial Period strata were fortuitously shielded from wind erosion.

The concomitant ~3 Ma onset of aridification and marked increase in the rate and spatial extent of shortening in the Qaidam fold belt is intriguing in the context of potential linkages between tectonics and climate. Asian interior stepwise aridification has been attributed to phases of rapid tectonically-driven orographic growth (Li and Fang, 1999; Qiang et al., 2001; Zhisheng et al., 2001). While tectonically-driven surface uplift might explain changes in climate over a million-year time scale, we deem it unlikely to cause the abrupt (within ~0.5 Ma; Heermance et al., 2013; Su et al., 2024) and drastic climate shift that the Qaidam Basin experienced at ~3 Ma. Rather, ~3 Ma marks the end of the global mid-Pliocene warm period (Haywood et al., 2016; Schwarz et al., 2022), leading us and most other investigators in the present community to favor a global climatic rather than a local tectonic driver for abrupt aridification.

An alternative hypothesis linking tectonics and climate concerns basin hydrology. Aridification would have resulted in an abrupt removal of mass from the endorheic Qaidam Basin by decreasing the amount of surface water, groundwater, and soil moisture. Seasonal changes in water mass loading of the Himalayan foreland basin have been shown to modulate rock deformation, with a higher frequency of seismicity and higher shortening rates during dry winters compared to wet summers (Bollinger et al., 2007; Bettinelli et al., 2008). Whether

changes in hydrology can cause secular changes in deformation rates, however, has yet to be demonstrated.

Kapp et al. (2011) speculated that the onset of wind erosion might have accelerated shortening within the Qaidam fold belt by removing mass from above it. The spatial extent of significant net wind erosion at ~3 Ma was likely limited, occurring only above the crests of the largest-amplitude anticlines in the fold belt. If erosional unloading by wind did modulate rock deformation, we would expect shortening rates to have generally increased from late Pliocene to late Pleistocene time along with the magnitude and spatial extent of net wind erosion. This prediction remains to be tested as shortening rate estimates are only available for binned time intervals of insufficient temporal resolution (e.g., from 8 – 2.5 Ma and 2.5 – 0 Ma, with marked increases in rate at ~2.5 Ma; Bao et al., 2017). Further detailed analysis of 3-D seismic-reflection profiles, coupled with constraints from borehole data, have potential to test whether Qaidam fold belt shortening may have accelerated from late Pliocene to late Pleistocene time.

At least locally above anticline crests, wind-erosion rates have been on the order of ~1 mm/yr, comparable to those in the Himalaya and other mountain belts (Montgomery and Brandon, 2002) where it has been proposed that erosion has had a positive feedback with rock deformation (Beaumont et al., 2001; Zeitler et al., 2001; Simpson, 2004; Montgomery and Stolar, 2006; Whipple, 2009). Spatially variable wind erosion of Qaidam anticlines might have influenced fold geometry and kinematics (Kapp et al., 2011). Global Positioning System studies show that the Qaidam fold belt is regionally accommodating shortening in the ~NE-SW direction at a rate of ~5–7 mm/yr (Gan et al., 2007; Wang and Shen, 2020). However, the axial traces of many anticlines trend more E-W than expected from this shortening direction and exhibit axial traces that are sigmoidal in map view (Figs. 4-6). The majority of Qaidam anticlines also exhibit steeper-dipping strata (and reverse fault scarps in places) along their windward, northeastern limbs (Fig. 4, yellow dotted lines), indicating that they are asymmetric and propagating approximately toward the northeast.

Many Qaidam anticlines have been argued to be associated with transpression, although whether locally dominantly dextral (right-lateral) (Song and Wang, 1993; Huang et al., 2021; Luo et al., 2022), sinisitral (left-lateral) (Liu et al., 2017; Liu et al., 2019), or variable through time and space across the basin remains to the resolved. As the Qaidam fold belt is bound to the northwest by the NE-striking left-lateral Altyn fault, areas of more regional and distributed shear

oriented more oblique to the trends of the anticlines is another possibility to consider when assessing fold kinematics (Liu et al., 2019). Highly spatially-variable wind erosion across the fold belt may have also influenced fold geometry and kinematics (Kapp et al., 2011).

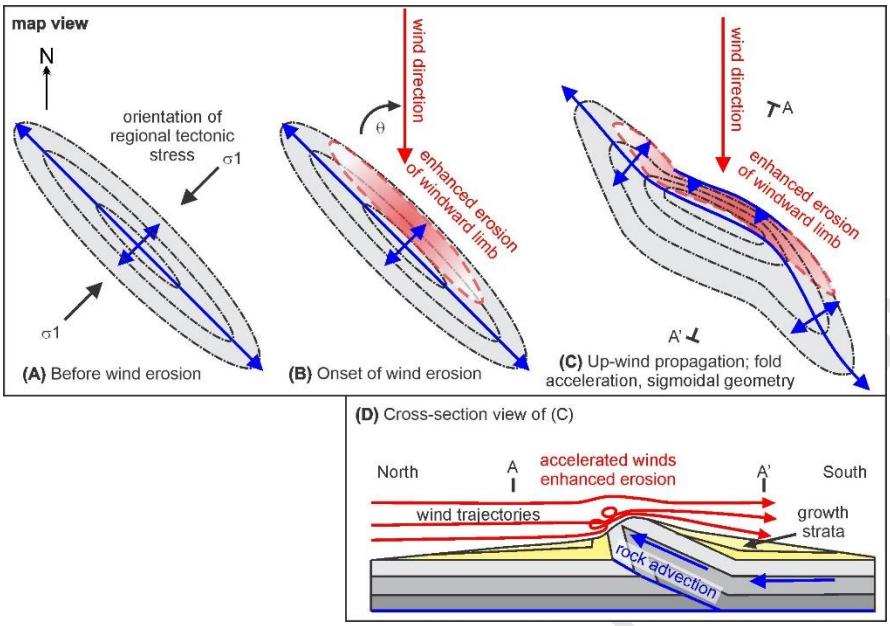

Figure 18. *Cartoon illustrating how spatially-focused wind erosion may have influenced fold geometry and kinematics. The top panel is in map view. Anticline axial traces are in blue and dash-dot lines are topographic contour lines, increasing in elevation toward the crest of the fold. Red shading indicates where erosion is focused; the deeper the red, the higher the rate of erosion. (A) Growth of a NW-SE trending symmetrical anticline in response to regional NE-SW tectonic stress prior to the onset of wind erosion. (B) Erosion begins in a northerly wind regime, oblique to the anticline axis. Erosion is focused on the windward side of the anticline and where topographic relief is the highest. (C) The central part of the anticline preferentially propagates in the up-wind direction where the most mass is being removed by wind erosion, resulting in a sigmoidal geometry. (D) Cross-section view illustrating why wind erosion may be enhanced along the windward sides of anticlines and why this in turn may favor upwind fault-fold propagation. Growth strata are also shown, which in the case of Qaidam basin anticlines are mostly late Pliocene to Quaternary in age (Fig. 7).*

We expand on the conceptual model of Kapp et al. (2011) for how at least some Qaidam anticlines might have evolved during Pliocene – Quaternary time (Fig. 18). Anticlines that began to grow prior to wind erosion along their crests (e.g, subaqueously) may have been more symmetrical and oriented more NW-SE, perpendicular to active regional shortening direction

(Fig. 18A). Winds accelerate as they move up and over topography and through constrictions (Jackson and Hunt, 1975; Laity, 1987). Focused unloading of mass by enhanced wind erosion would thus be expected along the central parts of the windward limbs of the anticlines where fold crest topographic heights reach their maxima (Fig. 18B, red shading). This focused erosional unloading may have facilitated more northerly fault-propagation folding and counterclockwise rotation (in map view) of axial traces along the central parts of the anticlines (Figs. 18C-D). This hypothesis predicts that (1) wind-erosion rates on the central windward limbs are greater than those along the leeward/southwestern limbs, (2) the anticline axial traces became progressively more sigmoidal in map view throughout Pleistocene time, and (3) axial traces of anticlines located in more northerly wind regimes are preferentially oriented more E-W. The first two predictions remain untested but the third can be explored given the detailed mapping of the wind regime, as proxied by the dominant yardang trends, along with the axial traces of the anticlines (Fig. 10).

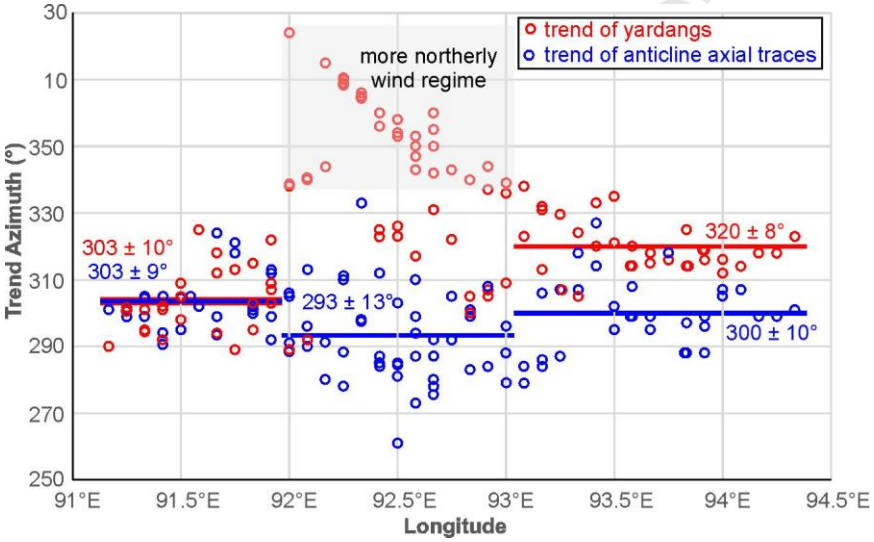

Figure 19. *Trends of yardangs and anticline axial traces as a function of longitude. Where the trends of the yardang are more northerly (generally 335° to 15° between 92°E and 93°E), the anticline axial traces trend more E-W (293 ± 13°) than those to the east or west.*

To conduct an objective and systematic analysis, we divided Figure 10 into five-minute (5') longitudinal slices. Where each 5' longitude intersected an anticline fold axis across the Qaidam fold belt, we measured the local trend of the axial trace and the trend of the most proximal yardangs (blue axial traces and red lines on Fig. 10, respectively). The data (n = 102 pairs of measurements) reveal the three visually dominant wind regimes in the Qaidam fold belt

as well as systematic correlations with anticline fold axis trends (Fig. 19). West of 92°E, the average anticline and yardang azimuth trends are indistinguishable, being 303 ± 9° and 303 ± 10°, respectively. East of 93°E, average anticline trends (300 ± 10°) are ~20° more westerly than the yardang trends (320 ± 8°). Between 92°E and 93°E, yardang trends are more northerly (generally 335° to 15°) and anticline trends are on average more E-W and scattered (293 ± 13°) than those to the east or west. The observation that fold axes are on average oriented more E-W in the more northerly wind regime motivates further consideration of a linkage between wind erosion and fold kinematics. If asymmetric fold growth is enhanced by wind erosion, we would expect its impact to be more substantial east of 93°E where there is a wind – fold direction obliquity of ~20° than to the west of 92°E where anticline axial traces and wind directions are subparallel.

2.6. Where did the wind-eroded sediment go?

A large volume of sediment has been blown out of the Qaidam Basin since ~3 Ma, estimated to be on the order of approximately half that of the volume of the Loess Plateau (Kapp et al., 2011). The extent to which dust lofted from the Qaidam Basin was transported by westerly winds over the Loess Plateau and/or by northwesterly winds over the eastern Tibetan Plateau (as seen in Fig. 3) and more southern parts of China where Quaternary loess is also present (Muhs, 2013) remains to be determined. Certainly, finer-grained Qaidam dust entrained by higher-level westerly winds would have been transported into or across the Pacific Ocean. During times of lake desiccation, Qaidam Basin sand could have saltated across the entire basin, up and over the Ela Mountains in the form of climbing and falling dunes and sand sheets (Evans, 1962), and into the Yellow River catchment and western Loess Plateau strata. We do not review here the enormous body of research that has focused on provenance of Neogene – Quaternary Loess Plateau strata beyond what we stated in the introduction. Rather, we turn our attention now to the question of how the Loess Plateau developed as a regional physiographic feature.

3. Chinese Loess Plateau

The >230,000 km^2 Chinese Loess Plateau is bounded by the Tengger and Mu Us deserts to the north and abuts the Luliang, Qinling, and Qilian mountains to the east, south, and west, respectively (Fig. 2). Precipitation is dominated by the East Asian summer monsoon and increases southeastward from ~200 mm/yr in the northwestern Mu Us Desert to >500 mm/yr over the central Loess Plateau (Porter et al., 2001). The Loess Plateau is incised by the Yellow

River and its tributaries and exhibits an archetype fluvial dendritic drainage pattern because of the homogeneous erodibility of loess. In more deeply incised valleys, the mostly Quaternary loess is locally underlain by the Neogene Red Clay deposits of eolian origin (Ding et al., 1999; Guo et al., 2002) and elsewhere sits unconformably above Mesozoic strata (Li, 2006).

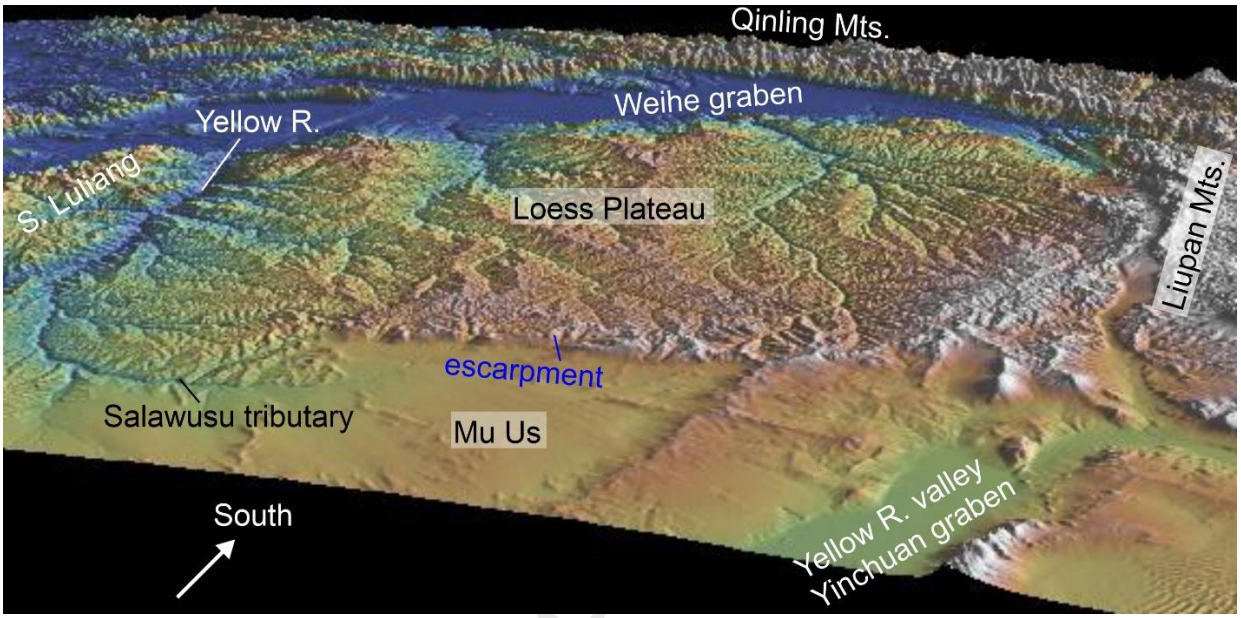

Figure 20. *Shaded relief perspective image with vertical exaggeration (www.geomapapp.org) showing the central Loess Plateau as viewed from the northwest. Note the prominent northern escarpment of the Loess Plateau. It is composed of loess and separates the fluvially incised Loess Plateau to the south from the dominantly endorheic Mu Us Desert to the north.*

The Loess Plateau is most prominent as a physiographic feature in its central part between the actively E-W shortening Liupan Mountains (Peizhen et al., 1991; Zheng et al., 2006) in the west and the southern Luliang Mountains in the east which comprise the western shoulder to the active NNE-trending Shanxi rift (Xu and Ma, 1992; Zhang et al., 1998; Clinkscales et al., 2021) (Figs. 2 and 20). In this central part, the northern and southern margins of the Loess Plateau are defined by prominent escarpments. The southern escarpment margin with kilometer-scale relief is controlled by extensional down-dropping of the Weihe graben (Figs. 2, 20, and 21) (Zhang et al., 1998). The crest of the northern escarpment margin locally stands at elevations of >1900 m, hundreds of meters higher than the adjacent Mu Us Desert to the north. There is no indication that this escarpment is controlled by Quaternary faulting (Zhang et al., 1998) and thus interpreted to be erosional (Kapp et al., 2015). The significance of this escarpment is best appreciated when approached from the perspective of the Mu Us Desert to the north (Fig. 20).

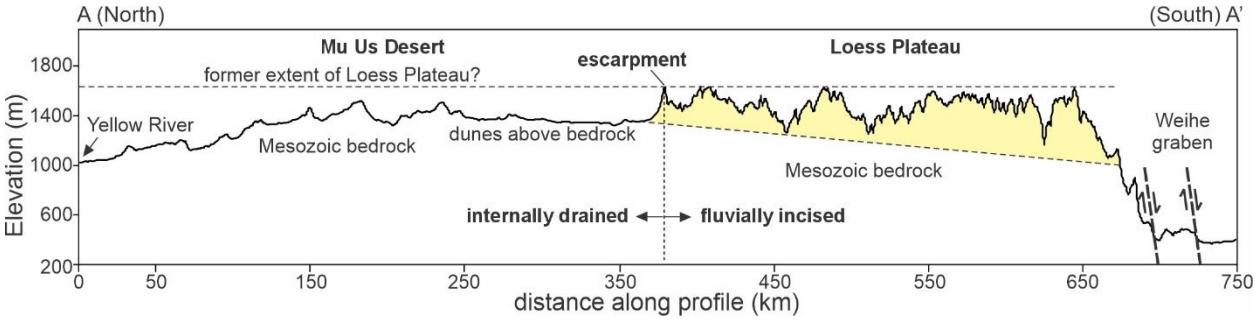

Figure 21. *N-S topographic profile across the Mu Us Desert and central Loess Plateau. Line of profile is shown on Figure 2. Modified from Kapp et al. (2015). Topography shaded in yellow is composed of Neogene – Quaternary Loess Plateau strata; dashed basal unconformity shown is schematic and oversimplified as there may be substantial topographic relief on it (Xiong et al., 2014; Zhu et al., 2018a).*

3.1. Mu Us Desert and Loess Plateau windward escarpment margin

Geomorphically-effective surface wind directions in the Mu Us Desert are westerly to northwesterly as indicated by eolian landforms and wind streaks (Fig. 2; Kapp et al., 2015) as well as surface wind measurements during modern windstorm events (Liu et al., 2005; Mason et al., 2008). Relatively friable Cretaceous sandstone floors most of the higher-elevation and -relief northwestern Mu Us Desert and is locally sculpted into yardangs and larger (kilometers- to tens-of-kilometers-long) wind-parallel bedrock ridges with relief of up to ~100 m (Fig. 22) (Kapp et al., 2015). Like in the western Qaidam Basin, one- to ten-km-scale wind-scoured depressions are ubiquitous (Fig. 22). Variably active and stabilized sand sheets and sand dunes and lesser Quaternary loess and paleosols locally cover bedrock in the northwestern Mu Us Desert but dominate in the lower-elevation and -relief landscape to the southeast (Lu et al., 2005; He et al., 2010; Wen et al., 2019). Quaternary eolian strata within the interior of the Mu Us Desert are mostly <25 ka, with only rare occurrences of older strata (oldest is ~150 ka) (He et al., 2010; Xu et al., 2015). Given that the desert interior is characterized by internal drainage, if older Neogene – Quaternary strata were deposited there, they have since been eroded and blown away.

The Mu Us Desert shows a subtle decrease in elevation as it approaches the northern escarpment margin of the Loess Plateau (Fig. 21). The transition from wind-eroded bedrock to eolian sand to loess (and from sandy to silty to clayey loess on the Loess Plateau) in the downwind and increased precipitation gradient direction is intuitive and common in desert-

marginal areas globally. More thought-provoking is the question of why the northern escarpment margin of the Loess Plateau, which is composed entirely of loess, rises hundreds of meters (up to ~400 m) like a "Great Wall of Dust" bounding the southern margin of the Mu Us Desert (Figs. 20-23). The metaphor with the Great Wall of China is additionally fitting because sections of it were constructed along the escarpment, which provides excellent 360° vantages at high elevation ideal for watchtowers.

Neogene Red Clay strata are locally exposed near the northern base of the escarpment (Li, 2006; our own observations). Hence, the magnitude of relief on the escarpment—up to ~400 m—provides an approximation for the thickness of loess strata along it. This suggests that the escarpment is composed of some of the thickest loess strata of the Loess Plateau, comparable to, if not thicker, than the thickest loess depocenters in the western and southwestern central Loess Plateau (Xiong et al., 2014; Zhu et al., 2018a). For comparison, mean loess strata thickness across the Loess Plateau is ~100 m, with thinner accumulations being present in the eastern and southeastern parts of the Loess Plateau (Xiong et al., 2014; Zhu et al., 2018a).

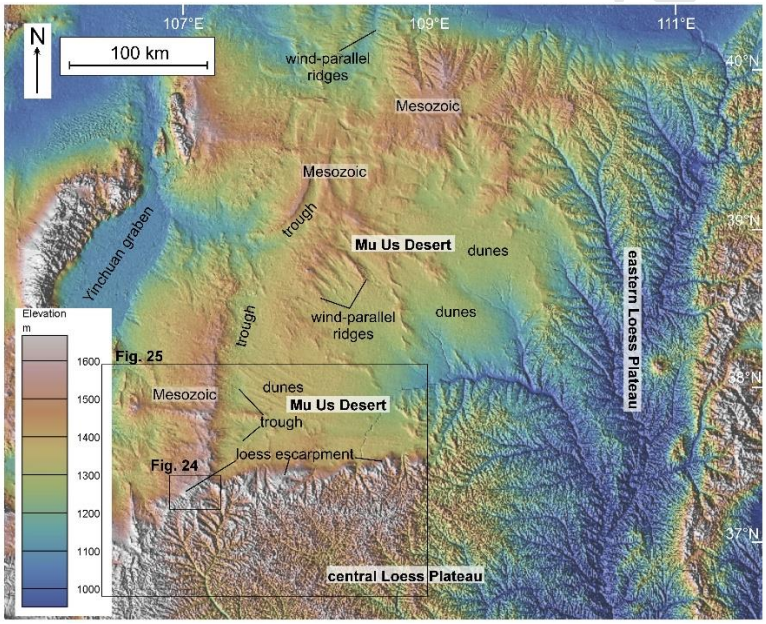

Figure 22. *Shaded relief map (www.geomapapp.org) of the Mu Us Desert and eastern and north-central Loess Plateau. Wind-scoured troughs and wind-parallel bedrock ridges are prevalent in the western Mu Us Desert. The northern margin of the central Loess Plateau is an erosional escarpment composed of loess.*

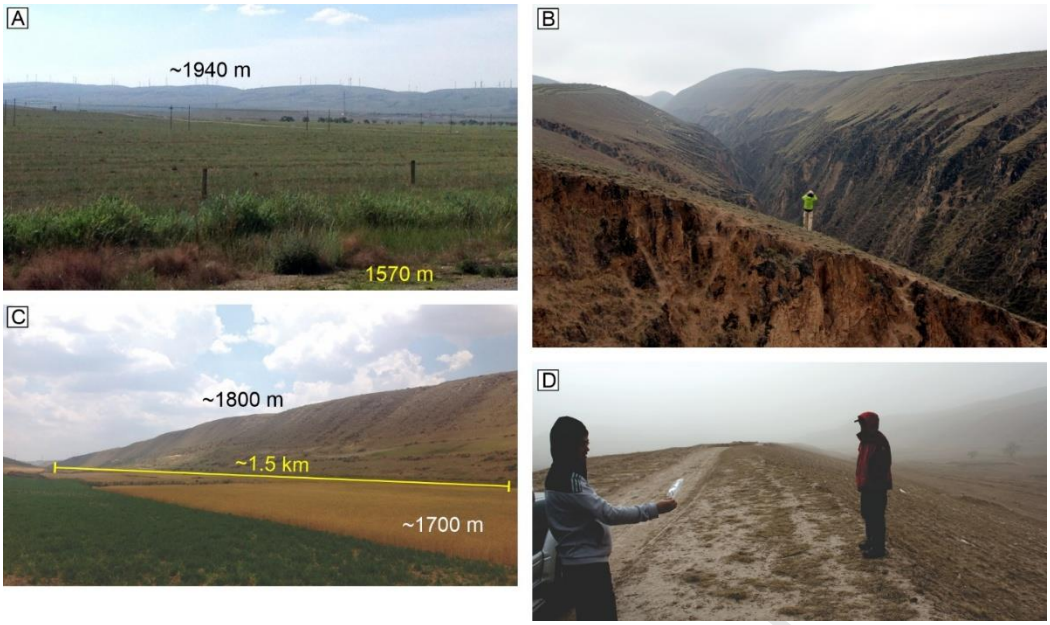

Figure 23. *Field photos. (A) Looking to the southeast up the windward face of the northern escarpment margin of the central Loess Plateau. Relief on the escarpment here is ~370 m. The crest of the escarpment, along which there are wind turbines, is a drainage divide between the endorheic Mu Us Desert to the northwest and the fluvially incised Loess Plateau to the southeast. Location: 37.396°N; 106.969°E. (B) Wind-parallel linear ridge and valley in loess, looking southward obliquely up the northern escarpment margin of the central Loess Plateau. Location: 37.129°N; 106.843°E. (C) Wind-parallel ridge of loess along the northwestern margin of the central Loess Plateau. Location: 37.133°N; 106.610°E. (D) Dirt road parallels a linear loess ridge near the drainage divide along the northwestern central Loess Plateau escarpment. Taken during a windy and dusty day (March 12, 2013), with a piece of plastic in the person's hand blowing downwind to the southeast. Location: 37.103°N; 106.859°E.*

3.2. Linear loess topography and wind erosion of the Loess Plateau

The presence of the windward escarpment of the central Loess Plateau (Figs. 20-22) requires that the loess strata of which it is composed previously extended farther northward into the Mu Us Desert and were subsequently eroded. There is ample evidence supporting downwind retreat of the escarpment by wind erosion. On the windward face of the escarpment, loess has been sculpted into wind-parallel ridges with lengths of ~7 km, a spacing of ~1 km, and relief of up to ~100 m (Figs. 23A-C). These ridges may appropriately be called megayardangs, but we refer to wind-parallel ridges (and intervening valleys) in loess as linear loess topography because

the mechanisms of its formation may differ from those of more classical yardangs in other types of bedrock. Smaller-scale linear loess topography is also superimposed on the dendritic drainage pattern in large parts of the central and eastern Loess Plateau (Kapp et al., 2015; Figs. 2 and 24). It has been shown that linear loess topography forms parallel to the geomorphically-effective wind direction and that wind erosion plays a significant role in its formation, although perhaps dominated by deflation of silt rather than abrasion by wind-blown sand as in the case of classical yardangs (Sweeney and Mason, 2013). While in the field during a windy and dusty spring day, we noted that surface winds were parallel to the linear loess topography (Fig. 23D) and that the dust was sourced locally from the Loess Plateau. Winds calmed and the sky cleared abruptly as we drove northwestward across the loess escarpment margin approximately one hour after taking the Figure 23D photo.

Orientations of linear loess topography vary systematically in space and suggest that geomorphically-effective surface winds become more northerly adjacent to the Luliang Mountains and over the central and western Loess Plateau (Fig. 2; Kapp et al., 2015). The length-scale and prominence of the linear loess topography generally decrease in the downwind direction before becoming absent; this may reflect a decrease in wind velocity downwind to the south. Kapp et al. (2015) showed that the surface wind pattern reconstructed from the eolian geomorphology of the Mu Us Desert and Loess Plateau is similar to near-surface wind vectors during some historical spring dust storm events, and which also show a southward decrease in wind velocity as speculated from the nature of the linear loess topography. Wind-speed reduction and associated enhanced dust fallout occur where there are relatively spatially abrupt clockwise (from more westerly to more northerly) changes in wind direction (Nugteren and Vandenberghe, 2004) (Fig. 2).

The highest elevation, western part of the northern loess escarpment is a drainage divide separating the fluvially incised and exorheic Loess Plateau to the south from the endorheic Mu Us Desert to the north (Figs. 24 and 25). The presence of wind gaps along the divide (Fig. 25) suggests that the upper reaches of formerly southward-flowing rivers were beheaded and reversed flow direction as the escarpment retreated in the windward direction (Kapp et al., 2015). The eastern part of the northern escarpment has been breached by headward fluvial incision within the upper reaches of the northward flowing Salawusu tributary of the Yellow River, such

that the modern drainage divide and wind gaps along it are offset to the south from the escarpment (Fig. 25).

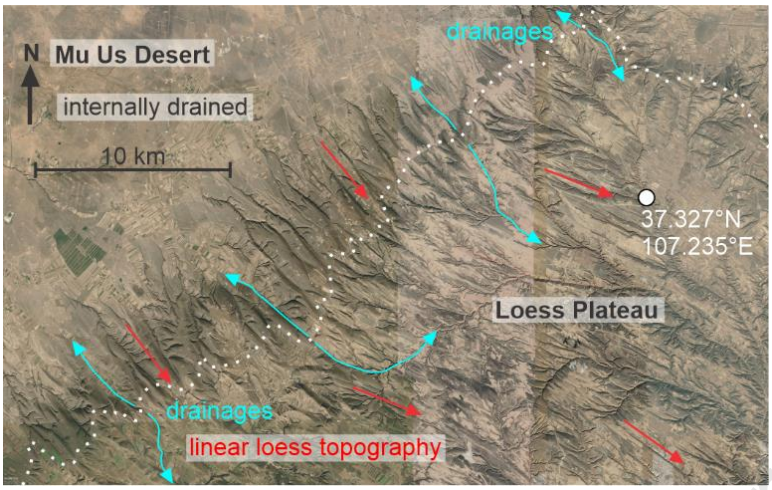

Figure 24. *Google Earth image of the westernmost part of the prominent escarpment margin of the northern central Loess Plateau. The crest of this portion of the escarpment is a drainage divide (dotted white line) between the endorheic Mu Us Desert to the northwest and the fluvially-incised Loess Plateau to the southeast. Light blue lines with arrow tips highlight a selection of drainages and their down-slope directions.*

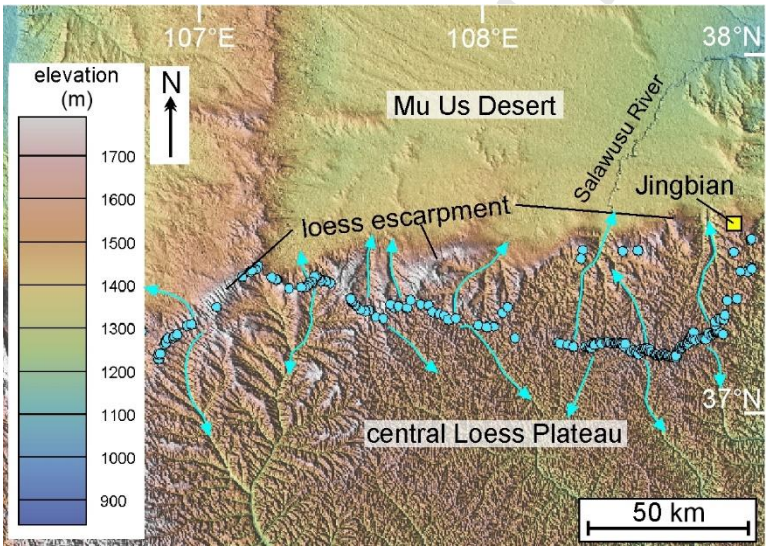

Figure 25. *Shaded relief map (www.geomapapp.org) of the northern escarpment margin of the central Loess Plateau. Blue dots are a selection of wind gaps mapped in Google Earth imagery. The western part of the escarpment forms a drainage divide between the Mu Us Desert and fluvially incised Loess Plateau. Here, the escarpment is retreating in the windward direction faster than the rivers are incising northward into it. To the east, wind gaps are offset to the south*

of the escarpment margin because of southward headward incision of the Salawusu tributary of the Yellow River. Light blue lines with arrow tips highlight a selection of drainages and their down-slope directions.

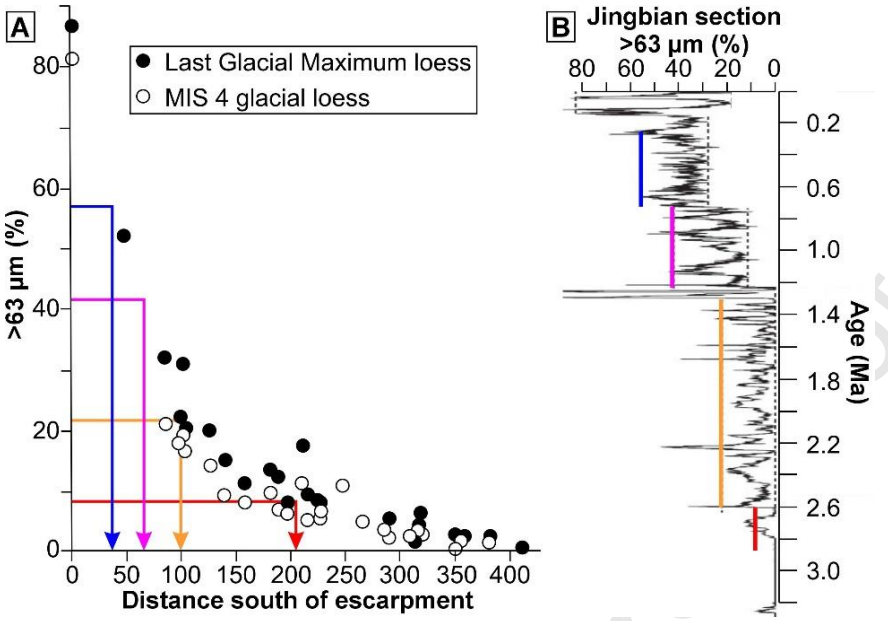

***Figure 26**. (A) Percentage of sand in Last Glacial Maximum and MIS 4 glacial loess as a function of distance south of the northern escarpment margin of the central Loess Plateau. (B) Percentage of sand in the Jingbian section (Fig. 25) as a function of age. The up-section increase in sand content suggests that the Mu Us Desert expanded southwards by hundreds of kilometers during the Quaternary, using the empirical results shown in (A). The colored lines show loess sand content for various time intervals (in B) and their implications for the history and magnitude of escarpment retreat (in A). Data are from Ding et al. (2005).*

The presence of wind gaps along the western part of the northern loess escarpment margin demonstrates that it is a dynamic physiographic feature that is retreating in the windward direction, as previously inferred (Nugteren and Vandenberghe, 2004) and implied (Ding et al., 2005) based on grain-size studies. The percentage of sand in Last Glacial Maximum and MIS 4 (~70 ka) glacial loess decreases systematically southward downwind from >80% near the Mu Us margin to nearly zero over a lateral distance of ~350 km (Ding et al., 2005) (Fig. 26A). Grain size analysis of the ~280-m-thick Jingbian Pliocene Red Clay strata and overlying loess-paleosol section along the northern escarpment (Fig. 25) reveals up-section increases in sand percentage in glacial loess: 0-10% prior to 2.6 Ma, up to ~20% between 2.6 and 1.2 Ma, ~40-45% between 1.2 and 0.6 Ma, and >50% since 0.6 Ma (Fig. 26B) (Ding et al., 2005). Using the Last Glacial

Period loess grain-size spatial correlation as a proxy suggests that a sandy desert source was located >200 km upwind of the Jingbian section during the Pliocene and expanded toward the section throughout the Quaternary. These grain size data provide additional evidence that loess strata previously extended farther north of the Loess Plateau windward escarpment and were eroded as the Mu Us Desert expanded.

Factors beyond spatial distance may control the percentage of sand in loess, such as vegetation cover and the strength, duration, and frequency of windstorms. There may have been less effective down-wind transport of sand-sized particles during lower-amplitude glacial periods and generally warmer climates of the early Pleistocene compared to the late Pleistocene (Herbert, 2023), and thus using grain size records of Last Glacial Period loess for calibration likely provides an overestimate in the magnitude of net Mu Us desert migration. However, Last Interglacial Period paleosols also show a systematic southward decrease in sand content, albeit of lower gradient (Ding et al., 2005); using these for calibration would decrease the distance of desert migration but not by more than a factor of two.

3.3. Erosion and Growth of the Loess Plateau

We expand on the hypothesis of Kapp et al. (2015) for how the Loess Plateau evolved. Neogene Red Clay strata and lower Pleistocene loess-paleosol sequences extended farther to the north and west of the modern Loess Plateau, perhaps covering most of the region that now comprises the Mu Us Desert (Figs. 21 and 27A). As aridity and glacial periods intensified during the Pleistocene, Asian deserts expanded and regions of former eolian deposition transitioned into regions dominated by wind erosion (Ding et al., 2005). Wind erosion scoured closed depressions and sculpted wind-parallel bedrock ridges in the Mu Us Desert (Fig. 27B). The Loess Plateau windward escarpment margin retreated as it was sandblasted while loess continued to accumulate downwind and further build the Loess Plateau. At any given time, loess transitioned downwind from proximal sandy loess to silty loess to clay-dominated loess. Mu Us Desert expansion and escarpment retreat thus explains the vertical up-section stacking from clayey to silty and then sandy loess in Pliocene – Quaternary strata along the windward margin of the Loess Plateau (Ding et al., 2005). Where the escarpment defines the boundary between internal drainage and fluvial incision, the rate of windward escarpment retreat has been greater than the rate of northward headward river incision (Fig. 27C). A profound implication is that eolian processes

are locally more effective than fluvial processes at eroding loess. Approximately 200 km of escarpment retreat since ~3 Ma suggested from grain-size analysis yields a retreat rate of ~7 cm/yr, which is roughly two orders of magnitude faster than that of escarpments composed of more indurated sedimentary bedrock (Duszyński et al., 2019).

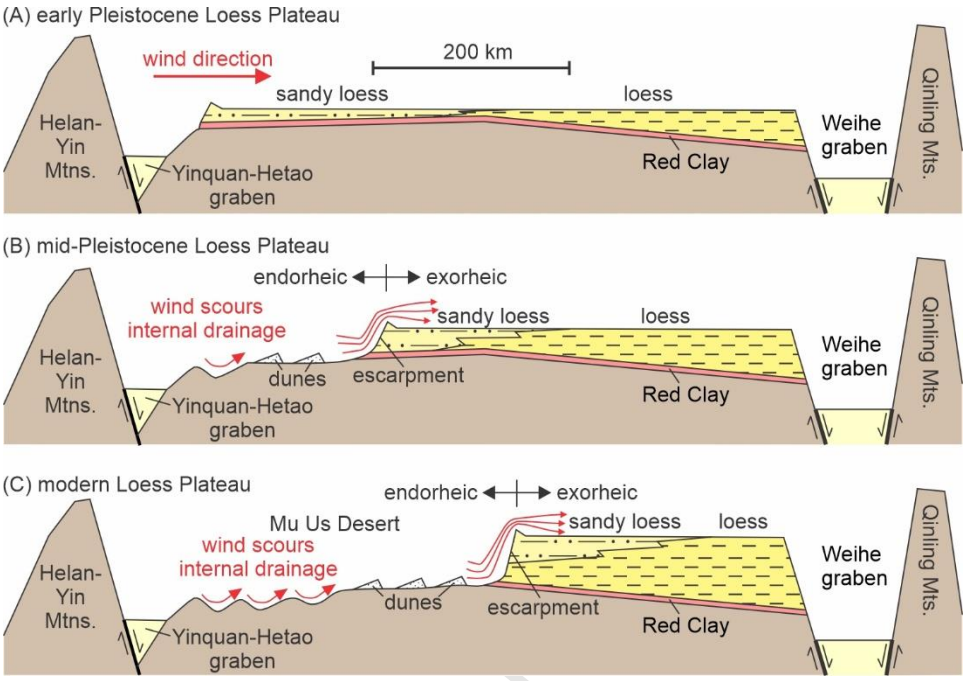

Figure 27. *Cross-sectional cartoon illustrating a million-year-scale history for how the Loess Plateau and its windward escarpment margin developed during the Neogene – Quaternary. (A) During the early Pleistocene, loess accumulated in the area that is presently occupied by the Mu Us Desert to the north and west of the modern Loess Plateau. (B) Pleistocene aridification and desert expansion transitioned the modern Mu Us Desert region from one of loess accumulation to net wind erosion. Wind erosion scoured closed depressions in the Mu Us Desert and led to downwind retreat of the Loess Plateau escarpment margin. (C) Continued Mu Us Desert expansion, downwind retreat of the Loess Plateau escarpment margin, and loess deposition downwind to further build the height of the Loess Plateau. While the cartoon underscores the importance of erosion and reworking of loess by wind in building the Loess Plateau, it is not intended to preclude contributions of silt and sand to the Loess Plateau from other source regions not shown (e.g., more inland sand deserts, Hexi Corridor alluvial-fluvial strata, Qaidam Basin, etc.; Fig. 2).*

The process of Loess Plateau development at the million-year timescale is analogous to using a leaf blower to generate an expanding region of bedrock erosion (the Mu Us Desert), a

windward-retreating escarpment made of leaves/dust, and a growing pile of leaves/dust downwind (Fig. 28). The history was more complex at shorter timescales as the Mu Us Desert – Loess Plateau marginal region transitioned between erosion and sediment accumulation in response to glacial-interglacial and millennial-scale climate fluctuations. A prediction of this hypothesis is that the windward margin of the Loess Plateau experienced erosion during peak glacial periods. This has been confirmed in the Jingbian section along the windward escarpment (Fig. 25) where there are ~60 kyr hiatuses corresponding to the last two glacial periods; instead, loess accumulation occurred primarily during stadials within interglacial periods (Stevens et al., 2018). This implicates the windward parts of the Loess Plateau as major contributors to atmospheric dust loading during glacial periods (Kapp et al., 2015; Licht et al., 2016; Stevens et al., 2018). Wind erosion of the Loess Plateau may have been nontrivial in places where linear loess topography is present (Fig. 2). Downwind of the linear loess topography, glacial period loess accumulation was continuous as demonstrated by high-sample-density luminescence dating of southern Loess Plateau strata (Zhang et al., 2022c).

Figure 28. *A leaf-blower analogy shows how wind can simultaneously erode and grow a plateau of leaves/dust.*

The development of the Loess Plateau hinges on the history and relative roles of wind erosion, fluvial erosion, and sediment accumulation at any given geographic locality. The common perception that Loess Plateau strata were deposited and then fluvially incised as the Loess Plateau was tectonically uplifted is misleading in two aspects. First, fluvial incision of the Loess Plateau is more likely enhanced by a decrease in base level elevation associated with down-dropping of the Weihe graben in the south (Figs. 2 and 21), rather than tectonically-driven

uplift of the Loess Plateau itself. The surface elevation of the Loess Plateau did likely increase by up to several hundreds of meters, but because of sediment accumulation rather than tectonics. Second, reconstructions of the Mesozoic bedrock topography beneath the Loess Plateau show that it was characterized by a southward decrease in elevation and hundreds-of-meters- to kilometer-scale topographic relief prior to the Quaternary (Xiong et al., 2014; Zhu et al., 2018a). This indicates that fluvial drainage was established in the Loess Plateau region prior to the onset of loess deposition. Supporting the antiquity of the Loess Plateau fluvial drainage network is documentation of buried paleogullies (Fig. 29) dating back to at least 600 ka (Porter and An, 2005; Huang et al., 2012); it is logical to speculate given the paleobedrock topography that early Pleistocene paleogullies are also present but have yet to be documented or dated.

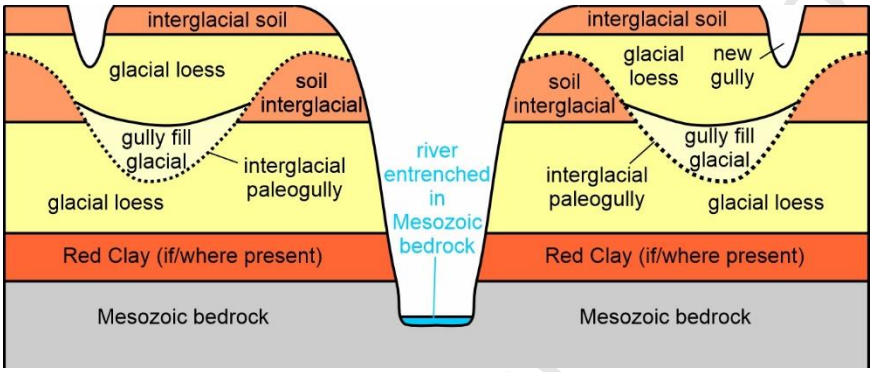

Figure 29. *Cross-sectional cartoon illustrating the stratigraphy and topography of the Loess Plateau. Eolian sediment accumulation during glacial periods exceeded the amount of sediment eroded by rivers during interglacial periods such that there is net growth and rise of the Loess Plateau. Illustration of interglacial paleogullies is adapted after Porter and An (2005). The larger rivers entrenched in Mesozoic bedrock might have been established prior to Loess Plateau development.*

Away from the most deeply incised, Mesozoic bedrock-floored valleys, there was net Pleistocene sediment accumulation in most places because former paleovalleys, incised mostly during interglacial periods, were completely buried by loess during subsequent glacial periods (Fig. 29; Porter and An, 2005). River incision rates in highly erodible loess are likely orders of magnitude faster than in the Mesozoic bedrock upon which the Loess Plateau strata were deposited. Fluvial erosion rates in highly erodible loess (Fu, 1989; Bryan, 2000) are likely orders of magnitude faster than in the Mesozoic bedrock upon which the Loess Plateau strata were deposited. This can explain why the floors of the deepest incised valleys of the Loess Plateau are

located within Mesozoic bedrock, but generally at depths of only meters to several tens of meters below the unconformity beneath the Neogene – Quaternary loess strata (Li, 2006). Low-gradient rivers occupying these deeply incised valleys might have been present prior to the Quaternary and already entrenched in erosionally-resistant Mesozoic bedrock, which would have impeded their efficacy to erode laterally. The high-elevation and low-relief loess tablelands which exemplify the physiography of weakly incised parts of the Loess Plateau (Fig. 30) developed where blankets of loess accumulated during glacial periods at a rate faster than rivers could incise into them during interglacial periods. Whether the spatial extent of loess tablelands increases or decreases in area is a delicate balance between rates of loess accumulation (and valley burial) and headward river incision. The basic observation that an enormous plateau of loess has been built, albeit deeply incised, demonstrates that the volume of loess accumulation has exceeded the volume of loess removed by fluvial erosion during the Quaternary, despite the highly erodible nature of loess. Hence, the future fate of the Loess Plateau is one of continued growth, at least downwind of the retreating erosional escarpment margin of the Loess Plateau.

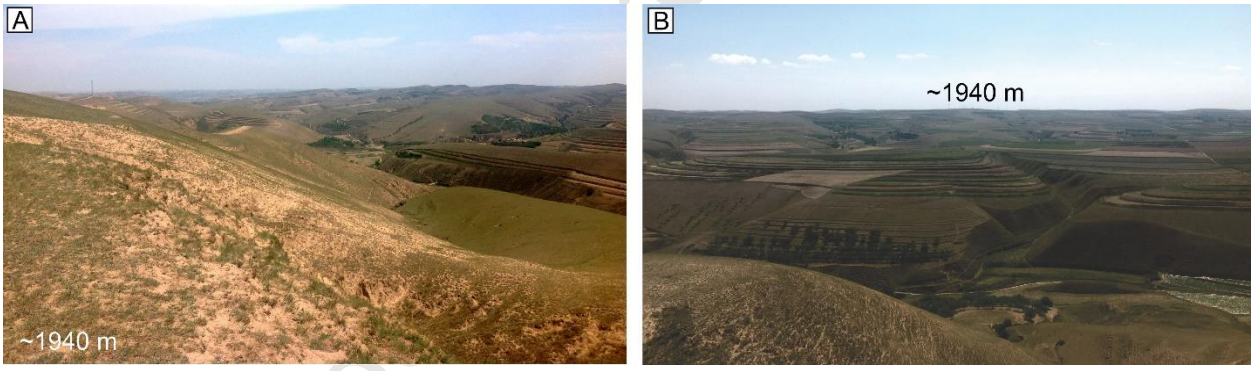

Figure 30. *Views to the (A) southeast and (B) southwest from the same locality (36.60°N; 106.71°E) showing the high-elevation plateau physiography of lesser-incised parts of the central Loess Plateau.*

4. Hami Basin

We now shift attention to our final case example of extreme wind erosion and gravel-dominated desert development. Located within the eastern Tian Shan, the composite Turpan-Hami Basin is ~600 km long east-west and up to ~200 km wide north-south (Figs. 2 and 31). The composite basin is recognized for its extremes—it is one of the lowest-elevation (-154 m in Turpan), hottest (up to ~67 °C land surface temperatures), and windiest hyper-arid deserts on Earth (Mildrexler et al., 2011; Yao et al., 2012). In contrast, towering to the north are >4000 m

elevation glaciated peaks of the Bogda, Barkol, and Karlik mountains of the eastern Tian Shan (Fig. 31). Here we focus on the Hami Basin (Figs. 31 and 32) as an extreme natural laboratory for studying feedbacks among geology, wind erosion and wind-eroded landforms, landscape evolution, atmospheric circulation, and dust emissions.

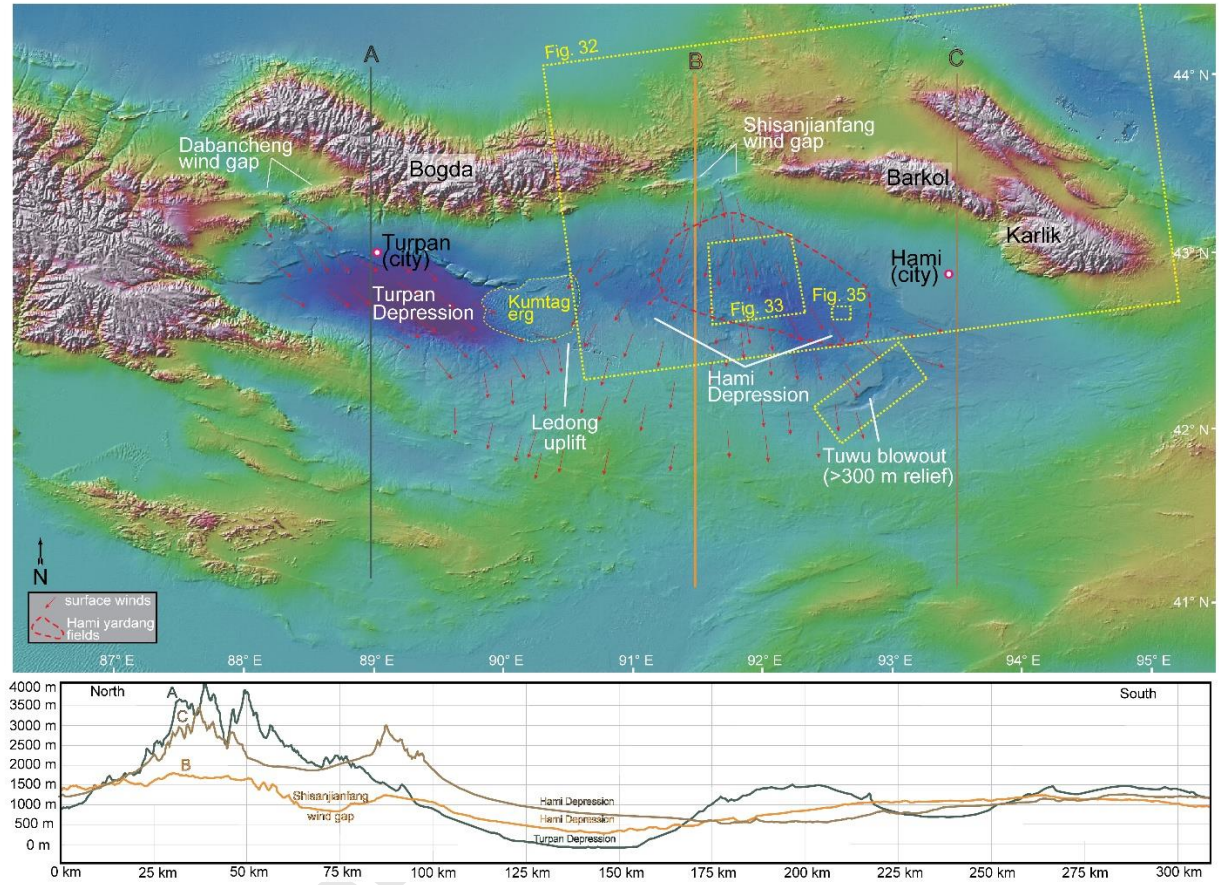

Figure 31. *Digital elevation map and topographic profiles (www.geomapapp.org) of the composite Turpan-Hami Basin, Xinjiang, China. Geomorphically-effective surface winds are based on orientations of yardangs, wind streaks, and gravel megaripples.*

4.1. Modern wind regime

The geomorphically-effective wind pattern in the Turpan-Hami Basin is illuminated by orientations of yardangs, crests of gravel megaripples, and wind streaks (Figs. 31 and 32). Surface winds where they enter the northern Hami Basin through the Shisanjianfang wind gap are northerly, move down-surface-slope, and generally fan out southwards. The Turpan Basin is dominated by northwesterly winds which enter the basin through the Dabancheng wind gap (Fig. 31). The two wind regimes converge over the Ledong uplift and trap the mountain of sand that is

the ~2000 km^2 Kumtag erg (Figs. 31 and 32). In the present climate, the Hami Basin experiences >100 days/yr with wind gusts of >17.2 m/s (Yao et al., 2012). An annual maximum daily extreme wind event of 44 m/s is predicted every two years at the Shisanjianfang wind gap, whereas an event of 60 m/s is predicted once every 100 years (Yao et al., 2012). While winds roar through the Hami Basin today, it is not a major emitter of dust because of the nature of its landscape and surface geology.

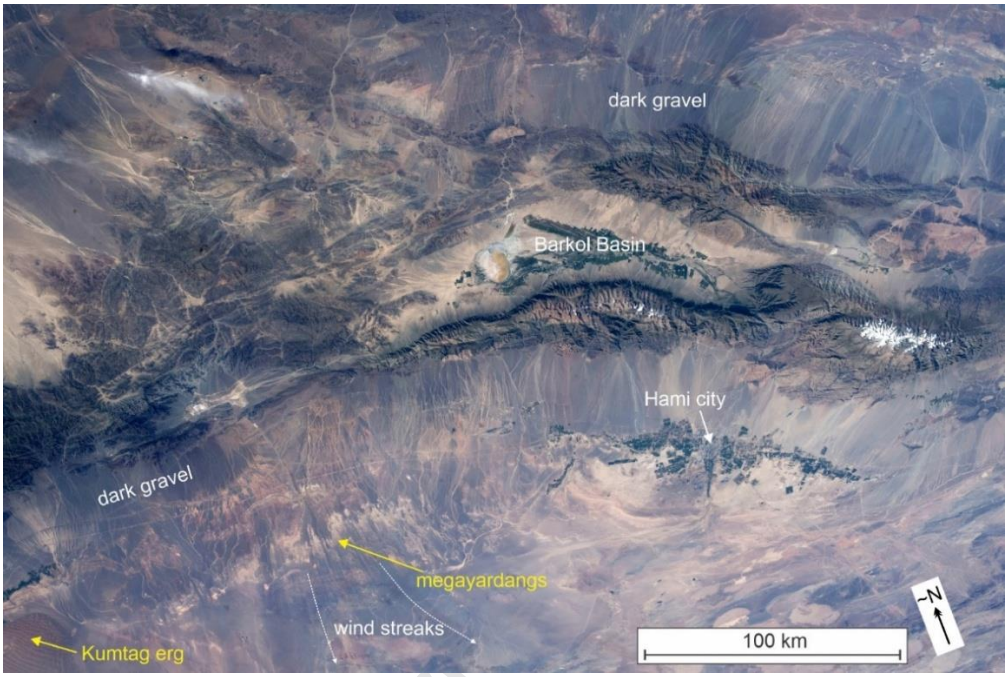

Figure 32. *Astronaut photograph of the northern Hami Basin and eastern Tian Shan. Credit: Earth Science and Remote Sensing Unit, NASA Johnson Space Center. NASA Photo ID: ISS063-E-64853. Date: 2020.08.01. Time: 08:58:01 GMT. Photo center point: 43.5°N, 92.5°E. Altitude: 413 km. https://eol.jsc.nasa.gov/SearchPhotos/photo.pl?mission=ISS063&roll=E&frame=64853.*

4.2. Stratigraphic architecture, surficial geology, and wind erosion

The endorheic Hami Basin has been interpreted as an underfilled flexural foreland basin loaded by the actively shortening and growing mountain belts of the eastern Tian Shan to the north (Allen et al., 1993). However, if basin subsidence was solely driven by flexure in response to the mass load of the eastern Tian Shan, we would expect basin topographic profiles to be asymmetric, with lower elevations being located more proximal to the actively growing mountain load to the north. Instead, basin N-S topographic profiles are markedly symmetrical

and concave up (Fig. 31). We raise two potential explanations for this and they are not mutually exclusive. The first is that the symmetrical concave-up profile is a result, or at least amplified, by extreme wind scouring of the basin floor. The second is that the symmetrical concave-up profiles and anomalously low elevations of the basin are surface dynamic expressions of active sinking of relatively dense and tectonically-thickened mantle lithosphere beneath it. Sinking of lithosphere has been inferred beneath parts of the western Tian Shan (Molnar and Houseman, 2004). Basins hypothesized, and numerically simulated to form above sinking drips of lithosphere are characteristically elliptical in map view, bowl-shaped and symmetrical in profile view, internally drained, and flanked by topographic bulges (Göğüş and Pysklywec, 2008; DeCelles et al., 2015; Wang et al., 2015b), much like the composite Turpan-Hami Basin (Fig. 31).

The southern Hami Basin exposes strongly deformed Paleozoic through Jurassic rocks. Unconformably overlying and exposed to the north of these deformed rocks in the central to northern Hami Basin are nearly flat-lying (dipping <1° to the south) Upper Cretaceous nonmarine clastic strata that have been eroded into >5 km-long and >50-m-high megayardangs in places (Fig. 33) (Pullen et al., 2018; Zhang et al., 2020a). The highest-elevation wind-eroded surface on Cretaceous bedrock sits at ~619 m elevation in the northern Hami Basin. Projection of this surface southward across the basin at a southward dip of 0.5–1.0° suggests that a minimum thickness of ~200 m of Cretaceous strata has been eroded from the lower-elevation parts of the Hami Basin (Pullen et al., 2018). In the southeastern part of the Hami Basin is the Tuwu blowout, forming a >500 km^2 irregularly-shaped endorheic depression with >300 m of local relief (Fig. 31).

In the northern Hami Basin, Cretaceous strata are in places unconformably overlain by Pleistocene alluvial strata (Fig. 33). At least six temporally distinct generations of upper Pleistocene alluvial fans with mappable terraces have been recognized (Zhang et al., 2020a). The alluvial-fan terraces decrease in age and elevation southwards, from 766 ± 78 ka at 247 m elevation to 86 ± 4 ka at an elevation of 62 m (Zhang et al., 2020a). This distribution of terrace deposits through space and time is interpreted to evidence the creation of new accommodation space through late Pleistocene wind scour such that younger alluvial fans were deposited at lower elevations and generally more southward in the Hami Basin. Although the depositional ages of the terraces span MIS 19 to MIS 4, no clear pattern for the timing of deposition is discernable because of the large uncertainties and limited number of ages that have been

determined thus far (Zhang et al., 2020a). However, the presence of these alluvial deposits and their eroded nature implies that the Hami Basin has undergone several phases of alluvial-fluvial deposition followed by eolian and fluvial erosion during at least the late Pleistocene and probably before. Additionally, elevated erosion rates of ~0.23 mm/yr during the last ~200 kyr (Zhang et al., 2020a) compared to ~0.12 mm/yr during the last ~20 kyr as quantified by cosmogenic ^{10}Be measurements may support enhanced wind erosion during colder and gustier glacial periods (Zhang et al., 2022a).

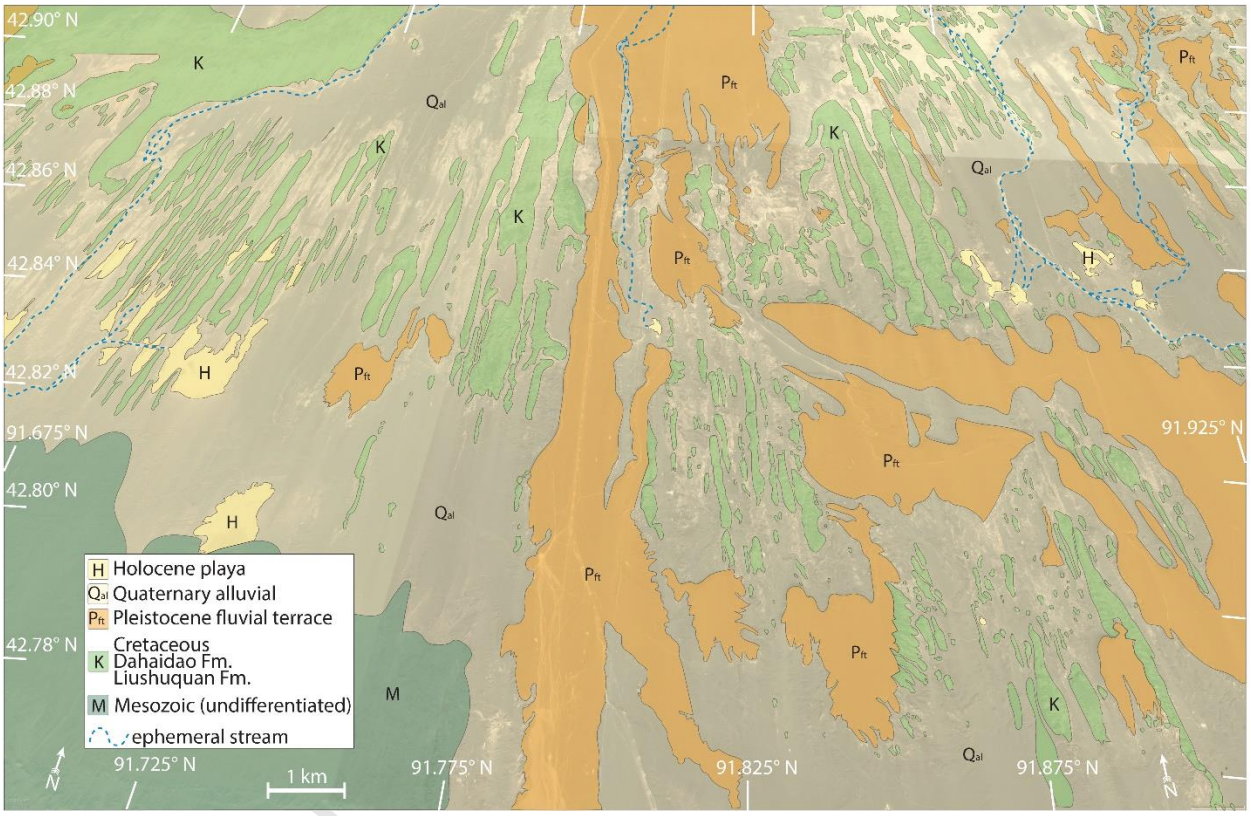

Figure 33. *Geological map of the north-central Hami Basin superimposed on a Google Earth perspective satellite image. The linear outcrops of Cretaceous strata are yardangs.*

The modern surface of the Hami Basin sheds light on the history of Pleistocene landscape evolution. The surface of the central and northern Hami Basin consists mostly of dark-colored unconsolidated gravels (~70%) and lesser unvegetated exposed bedrock (~25%) and active ephemeral channels and playa surfaces (~5%; Figs. 32 and 33) (Pullen et al., 2018). The unconsolidated gravels are organized into planar desert pavement surfaces and gravel-mantled eolian ripples. Little unconsolidated sand and finer clastic particles are present on the surface. It is likely that a significant volume of sand-sized sediment has been removed from the basin by

saltation up and over mountain ranges to the south and ultimately into the Taklamakan sand sea (Fig. 2).

The Hami Basin desert pavements are interpreted to have formed from the in-situ winnowing of finer-grained clasts from underlying conglomerate beds (Pullen et al., 2018; Zhang et al., 2020a). Although some inflation of the regolith has occurred (McFadden et al., 1987; Zhang et al., 2020a), deviations to finer grain-size distributions below the gravel lags (e.g., formation of an A horizon) are limited, suggesting that deflation dominated over inflation during the development of Hami desert pavements (Pullen et al., 2018). Once developed, the tightly-spaced gravel clasts and increased surface roughness of the desert pavements armors the land surface against further wind erosion. Thus, the position of the conglomerate beds within the stratigraphy exerted a first-order control on where the desert pavement surfaces developed and why they are topographically tiered. Because erosion through the pavement surfaces is comparatively very slow (Zhang et al., 2022a), eolian and nominal fluvial undercutting of the desert pavement surfaces, especially where finer-grained strata are present, are invoked to explain the denudation of desert-pavement-capped landforms and, in part, the differential erosion across the basin.

4.3. Feedbacks between landscape properties and atmospheric circulation

There are arguably two end-member states in the climate and landscape evolution of the Hami Basin: (1) drier, sediment-starved times when wind erosion effectively removes most loose sand and finer-grained sediment and dark-colored gravel deposits dominate the basin floor, as in the modern Hami Basin; and (2) wetter times when alluvial-fluvial deposits aggrade into the Hami Basin, as evidenced by the erosional remnants of upper Pleistocene alluvial fan deposits. Here we summarize how these two end-member climate-landscape states might have influenced near-surface atmospheric boundary conditions, and vice versa, based on a modeling approach (Abell et al., 2020a; Abell et al., 2020b).

There are several variables of an arid, unvegetated landscape that can impact local winds. One of these is albedo. Specifically, as land surface albedo changes, so too do the land surface temperatures and their spatial gradients. In the case of the Hami Basin, as the landscape evolved from being dominated by relatively light-colored alluvial-fluvial deposits to dark-colored gravel-dominated surfaces/deposits, the albedo would have shifted as well. A decline in albedo would

be expected to increase the surface temperature of the Hami Basin, holding all else constant, as well as the temperature gradient between the mountains bounding the basin to the north and the basin floor itself. Because altered temperature gradients influence pressure gradients, near-surface wind speeds would also be impacted. Considering changes in albedo only, Abell et al. (2020a) found that under a plausible decline in albedo (assuming the Hami Basin had the albedo of the modern Qaidam Basin or Taklamakan Desert prior to significant wind erosion and desert pavement development) springtime 10-meter wind speeds within the basin would be up to 25% higher today compared to when it was filling with alluvial-fluvial sediment. The lower albedo model scenario also showed decreased wind speeds exiting the Hami Basin and moving towards the Hexi Corridor and Taklamakan Desert.

Another variable that could have impacted atmospheric circulation in the Hami Basin as its landscape evolved is surface roughness. A follow-up study assessed the impacts of changes in surface roughness (greater with the presence of gravel pavement) and erodibility (lower with the presence of gravel pavement), in addition to albedo, on not only the characteristics of the atmospheric boundary layer, but also dust emissions and transport (Abell et al., 2020b). The effects of albedo on near-surface temperature, surface pressure, and wind speed in this suite of simulations are similar to the work of Abell et al. (2020a), ultimately leading to slower 10-meter wind speeds when albedo was higher. However, the impacts of surface roughness and sediment erodibility overwhelm the effects of albedo, leading to a net increase in wind speeds for conditions representative of the Hami Basin when finer-grained alluvial-fluvial deposits were more prevalent. The enhanced winds and higher erodibility of the landscape also resulted in increased dust emissions for the Hami Basin, most of which is transported proximally to the Hexi Corridor and Taklamakan Desert.

Overall, the modeling simulations illustrate the importance of landscape properties on influencing atmospheric circulation. However, they were performed using modern spring-time climate conditions (specifically, 00:00 UTC 1 February 2011 to 00:00 1 June 2011) (Abell et al., 2020a; Abell et al., 2020b). Further investigations are needed to assess the relative importance of landscape properties during past colder and drier glacial periods and warmer and likely wetter (e.g., Pliocene) climates.

4.4. Landscape evolution hypothesis

We expand on a hypothesis for how the landscape of the Hami Basin evolved during Pliocene – Quaternary time (Pullen et al., 2018; Abell et al., 2020b; Zhang et al., 2020a), with implications for the history of dust emission (Fig. 34). During the warmer and wetter Pliocene, the Hami Basin likely filled with dust-fertile alluvial-fluvial-lacustrine sediment sourced from mountain ranges of the eastern Tian Shan to the north (Fig. 34A). At the onset of colder, drier, and windier glacials of the latest Pliocene or early Pleistocene, sand and finer-grained sediment were removed from the basin by wind (Fig. 34B). The lower surface roughness and finer grain size of the surface sediment during these intervals might have acted to increase wind speeds, wind erosion, and dust emissions. Alluvial fans are notoriously high dust emitters (Sweeney et al., 2011; Wu et al., 2018; Bakker et al., 2019). We envision that without significant surface "refreshing" through the deposition of additional alluvial-fluvial and playa deposits, dust emissions would have diminished as eolian winnowing resulted in more gravels coalescing at the surface (Fig. 34C). Thus, we infer that reduced dust fertility may have occurred during the later stages of glacial intervals because precipitation, generally lower during glacials, would have been the primary cause of surface refreshing. As such, we posit that sediment refreshing primarily occurred during wetter interglacial periods (Fig. 34D). In the proceeding glacial, dust emissions would initially spike early when the exposure of finer-grained sediment was still extensive (Fig. 34E) and then decrease as gravelly surfaces develop and act to armor the land surface from further wind erosion (Fig. 34F). We infer that dust emissions would be slightly higher at the beginning of the next dry glacial period (Fig. 34E) than at the end of the proceeding dry interval (Fig. 34C). We speculate that these cycles of surface refreshing, higher dust emission at the start of a dry interval, and diminishing dust emission until the end of the dry interval, repeated throughout the Pleistocene (Fig. 34G-I), and likely followed glacial-interglacial variability.

In summary, the general long-term trend in the Hami Basin was towards higher concentrations of unconsolidated gravel desert pavements on the surface and lower dust fertility, regardless of wind speeds (Fig. 34J). However, this long-term trend was punctuated by intervals of alluvial-fluvial-playa deposition and sediment refreshing, likely during wetter interglacial periods. If the inferred landscape and dust-emission evolution for the Hami Basin is representative of the broader stony Gobi Desert, then despite net aridification and desert expansion throughout the Pliocene – Pleistocene, the establishment of widespread gravel

surfaces may have served to decrease dust emissions from this enormous dust-source region. This dust emission history contrasts to that inferred for the Qaidam Basin, which due to progressive aridification and rock deformation and uplift, exposed a larger area of fine-grained and friable (mostly lacustrine) strata to wind erosion from early to late Pleistocene time.

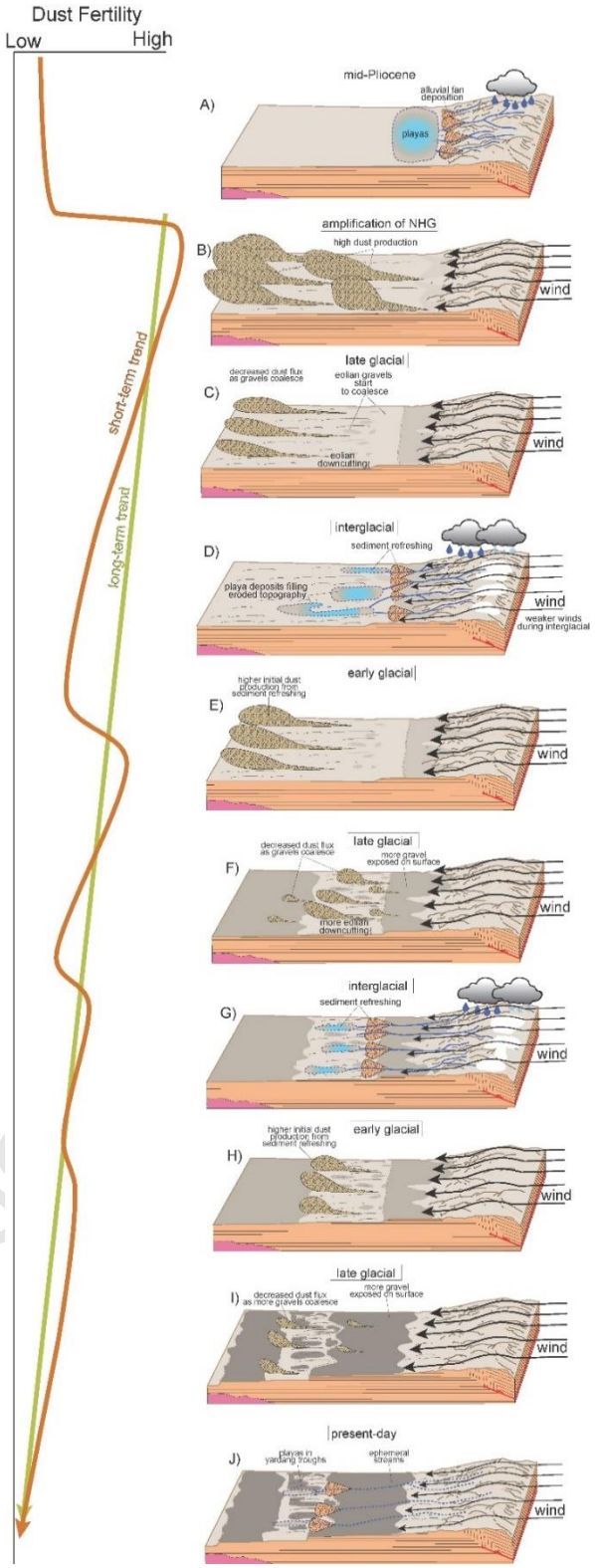

Figure 34. *Pliocene – Pleistocene landscape evolution model for the Hami Basin considering climate states, alluvial-fluvial-lacustrine deposition, and wind erosion. Long-term dust fertility*

trend ignores glacial-interglacial cyclicity whereas the short-term trend considers 40-100 kyr cycles. See text for description of A-J.

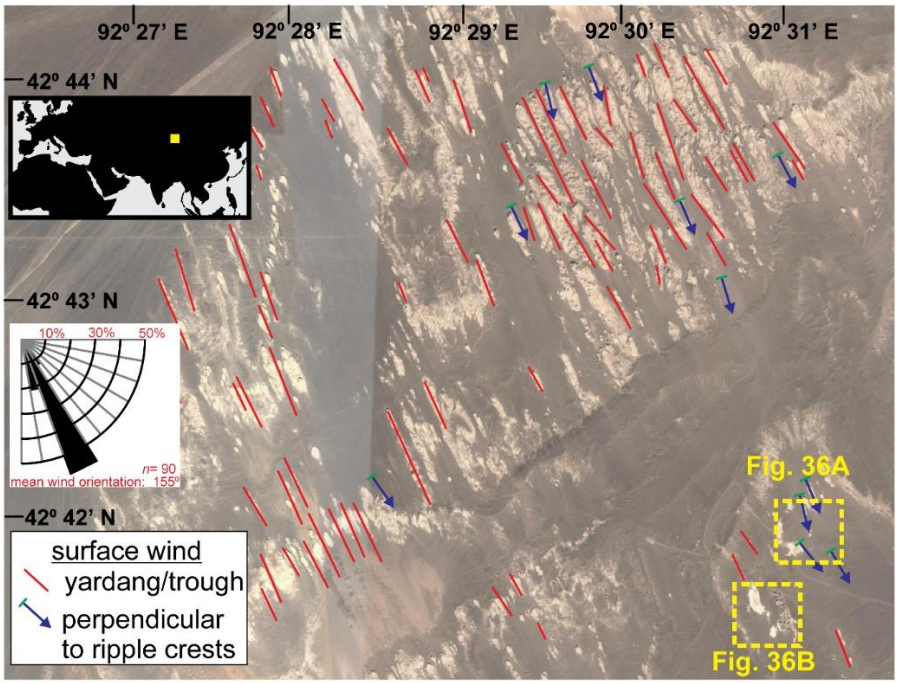

Figure 35. *Region of jointed yardang landforms in the Hami Basin.*

4.5. Role of structural joints in landform development

Along the eastern margin of the Hami Basin, approximately halfway between the longitude of the Shisanjianfang wind gap and the city of Hami (Fig. 31), wind-eroded Cretaceous bedrock is pervasively deformed by joints. Joints are the most ubiquitous form of brittle deformation in rock on Earth and develop predominately by tensile failure as rock expands vertically and contracts horizontally during removal of overburden (van der Pluijm and Marshak, 1997; Davis et al., 2012). Joints form spaced to penetrative planes of weakness within rocks and typically form as orthogonal and/or conjugate joint systems. Joints may exert first-order controls on gravitational wasting of rock, landform morphology, and erosion rates (Brookes, 2001; Gutiérrez-Elorza et al., 2002; de Silva et al., 2010). Here, we provide a case example from the Hami Basin of how joints influence yardang morphology and erosion rates, and conversely, how spatially variable wind erosion may have influenced joint orientations.

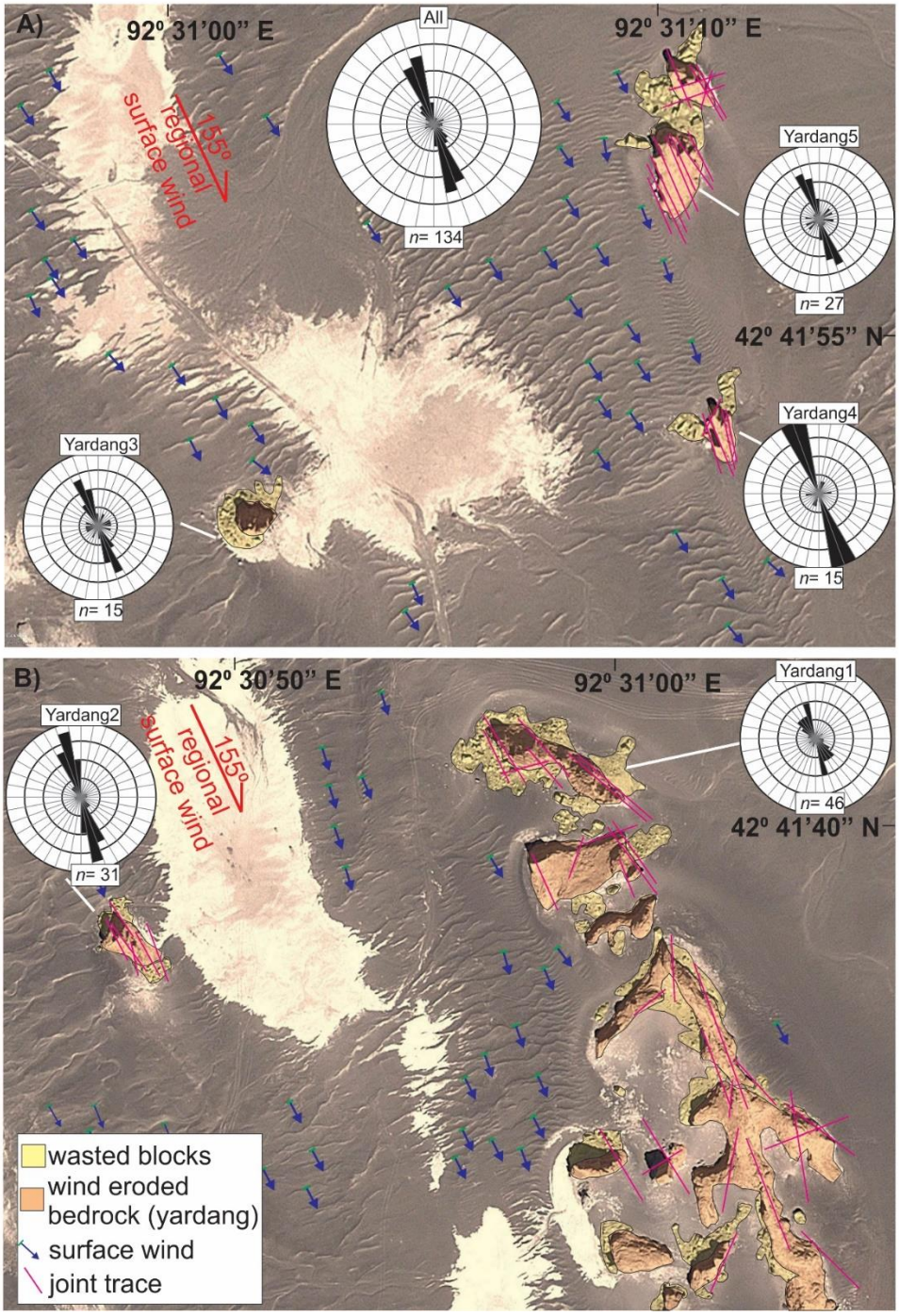

Figure 36. *Google Earth images showing distributions and orientations of eroding bedrock, eolian gravel ripples, and joints. Rose diagrams show the strike azimuth orientations of joints.*

In the jointed rocks study area (Figs. 35 and 36), the orientations of yardangs and ridge crests of eolian gravel-mantled ripples indicate that the geomorphologically-effective wind direction is toward ~155° (Fig. 35 inset). The nearly flat-lying Cretaceous strata consist of well-

indurated mudstone and sandstone, and are exposed as blocky, linear landforms (Figs. 37 and 37A-D). Orientation measurements of $n = 134$ joint surfaces exposed at $N = 5$ yardang localities yield a mean dip of 83° with a standard deviation of 8° and two dominant strike directions clustering at ~164° and ~340° (Fig. 36).

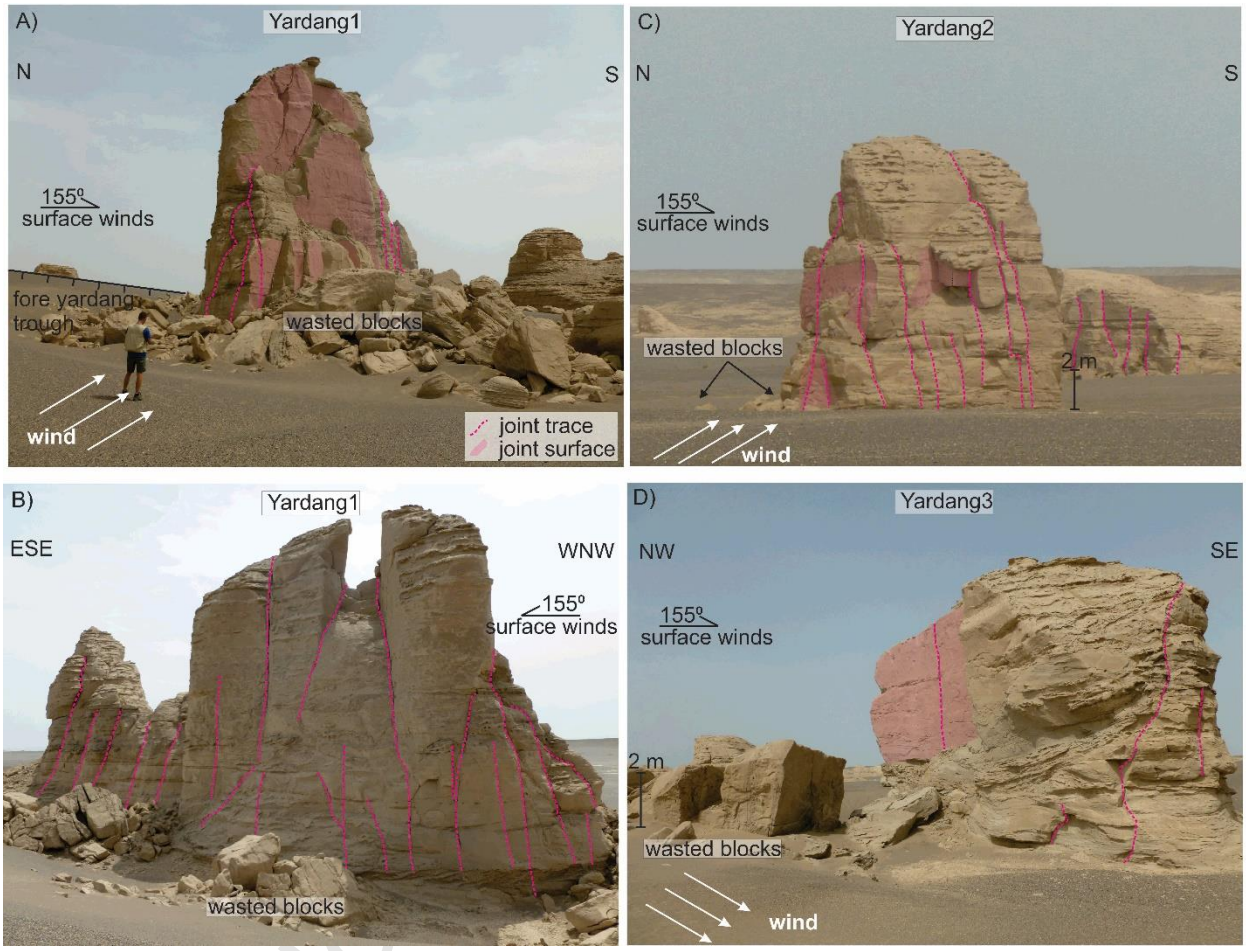

Figure 37. *Photos of yardangs and peripheral mass wasted blocks. Joint traces are denoted with pink dashed lines; joint surfaces are mapped with opaque pink polygons.*

Joint orientations may be controlled by the regional tectonic stress field (Davis et al., 2012) or more local stress perturbations generated by topography (Chapman, 1958; Savage and Swolfs, 1986; Molnar, 2004; Martel, 2017). The eastern Tian Shan is actively shortening ~NNE-SSW within an overall left-lateral transpressional setting based on Global Positioning System (Wang and Shen, 2020) and field-based neotectonic studies (Cunningham et al., 2003). If joints were to form within this regional stress field, their dominant orientation should be parallel to the regional shortening direction. Instead, the dominant joint orientations are subparallel to the geomorphically-effective wind direction (Fig. 36). Cretaceous bedrock is thus preferentially

dilating perpendicular to the wind direction (Fig. 38) and towards the inter-yardang troughs, likely due to preferential removal of mass by wind erosion along them and the resultant topography-driven stress perturbations. Conversely, the presence of weak joint planes in bedrock influences the rates and style of erosion.

Wind abrasion by saltating and suspended particles is greatest <1 m above the surface for nearly all wind regimes on Earth (Anderson and Hallet, 1986) and along the windward faces of yardangs. Preferential eolian undercutting and erosion around the windward faces of yardangs contributes to the formation of windward-side steep faces, aprons of mass-wasted blocks, and crescent-shaped (in map view) wind-echo-generated moats (Blackwelder, 1934; Halimov and Fezer, 1989; Xiao et al., 2018). These erosional products are exemplified by the jointed Hami yardangs. The presence of weak subvertical joint surfaces together with the lithologic and strength heterogeneity of the subhorizontal Cretaceous strata facilitate the generation and mass wasting of cuboidal blocks. Debris fields of wasted blocks are abundant within windward troughs across wind-parallel horizontal distances of 5–40 m (Figs. 36-38). The windward faces of wasted blocks show textures consistent with eolian abrasion, such as rounded edges and pitted surfaces. In contrast, the leeward surfaces of the wasted blocks are typically planar and have sharp edges consistent with joint-controlled detachment surfaces (Fig. 37D). The jointed yardang study region could arguably be in the last stage of yardang evolution—demise—in which yardang lengths are decreasing and inter-yardang corridors have transitioned from eolian downcutting to surface armoring from eolian gravel ripple deposits (Barchyn and Hugenholtz, 2015) (Fig. 38).

Mass wasting of jointed cuboidal blocks leads to a greater total surface area of indurated bedrock within the near-surface eolian high-kinetic energy flux zone and thus may serve to increase rates of wind erosion. The Hami Basin provides a natural laboratory to test this inference because yardangs are not uniformly jointed, and wind speeds are not uniformly high across the Hami Basin. For example, joints are present but much less pervasive in the wind-eroded Cretaceous bedrock along the N-S axis of the Shisanjianfang wind gap where near-surface wind speeds are the fastest in the Hami Basin (Yao et al., 2012; Abell et al., 2020a; Abell et al., 2020b). However, Zhang et al. (2022) showed that cosmogenic ^{10}Be derived erosion rates are indistinguishable in both areas (~0.12 mm/yr), presumably because the higher erodibility of

the jointed yardangs and mass wasted blocks balances out the effects of relatively slower wind speeds.

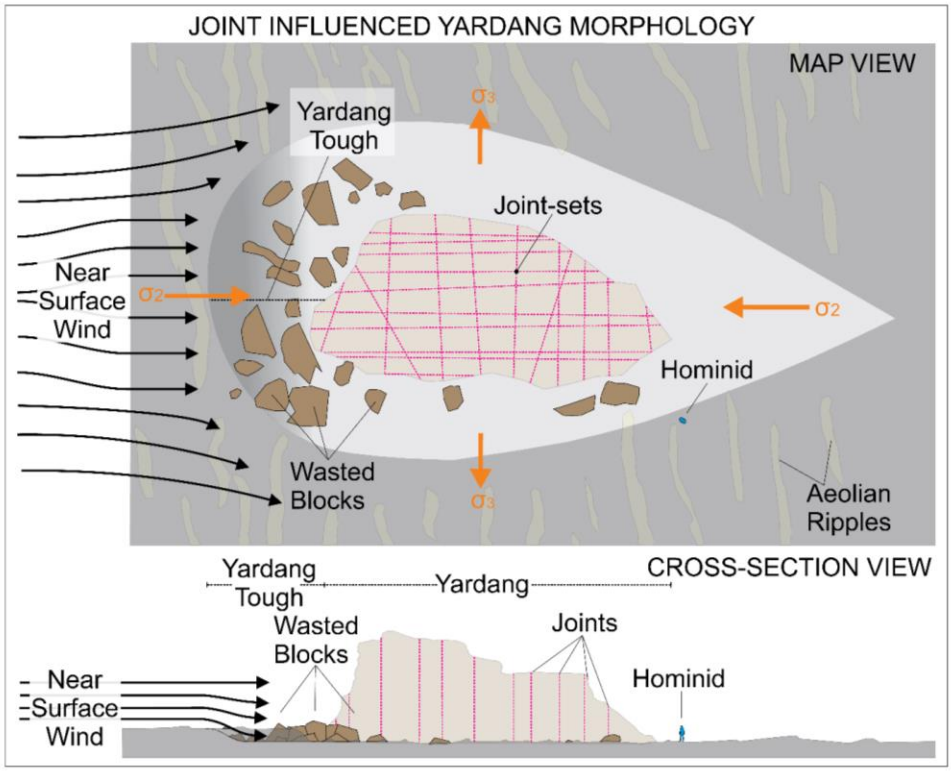

Figure 38. *Schematic geomorphic model of yardang demise, showing the distribution of wasted blocks, jointed yardangs, and eolian gravel ripples.*

5. Discussion and conclusions

The extent to which wind processes has modified northern China's local and regional landforms and landscapes over the past few million years is profound. A thickness of hundreds of meters of strata has been removed from parts of the Qaidam fold belt, the Mu Us Desert, and the Hami Basin by wind, and locally kilometers of strata from above Qaidam anticline crests. Wind processes scoured and expanded the Mu Us Desert and simultaneously built, eroded, and moved the Loess Plateau (Fig. 27). The Loess Plateau exists because here the wind is mightier than the rivers. Landscape modification by wind was most extensive during glacial periods and is thus unable to be directly observed or measured in the modern interglacial climate. However, stratigraphic and geomorphic records of wind processes abound, and their future investigation offers endless potential for discovery. In this final section we discuss some broader implications

of wind-themed research findings in China along with outstanding questions and future directions.

5.1. Yardangs and paleoyardangs

There is a growing appreciation of the large diversity of yardang landforms and how they might evolve (Dong et al., 2012a; Barchyn and Hugenholtz, 2015; Li et al., 2016; Hu et al., 2017; Pelletier, 2018; Pelletier et al., 2018). Yardangs are in many places not streamlined and may form in areas where there is more than one geomorphically-effective wind direction (Fig. 10). Not all yardangs are destined to reach a stage of erosional demise (Dong et al., 2012a; Barchyn and Hugenholtz, 2015). For example, yardangs within many Qaidam fold belt rocks developed preferentially within more resistant sedimentary beds. Given the tilted nature of the sedimentary bedding, the length scales of the yardangs are controlled by the strike of the bedding, relative to the wind direction, and the dip angles and thicknesses of the more resistant beds. Moving forward in time, bedding-controlled yardangs will propagate spatially downwind (or upwind) depending on whether bedding is dipping downwind (or upwind), but not reach demise as the more resistant beds are continuously being exhumed to the surface.

Yardangs may be buried during wetter climatic conditions to become paleoyardangs, as proposed for the Qaidam Basin during interglacial periods of sediment accumulation. Paleoyardangs are challenging to identify in the stratigraphic record, directly in the field or remotely in satellite imagery, especially if they are oriented subparallel to “modern” yardangs. One may even question how many burial-exhumation cycles a “modern” yardang has experienced. Paleoyardangs are larger in scale than sedimentary structures typically documented in detailed measured stratigraphic sections and smaller in scale than regionally mappable unconformities. The most readily identifiable paleoyardangs in the Qaidam Basin are the oddly-oriented ones, which in turn reveal a reasonable but yet-to-be-explained near surface paleowind pattern (Fig. 17). A concerted search will certainly reveal paleoyardang fields in other stratigraphic records globally, and particularly through subsurface imaging techniques like ground penetrating radar and high-resolution seismic-reflection profiling. Candidate environments for paleoyardang preservation include coastal deserts and their offshore basins, in which sediment deposition versus erosion is modulated by sea level, in addition to lake/playa environments like those in the Qaidam Basin. The preservation of paleoyardangs in sandy desert

settings is less certain. Sand seas and sand dunes are prevalent downwind of yardang fields, and thus if surface wind directions remain uniform, it is unlikely that yardangs would get buried and preserved beneath eolian sand. However, changes in surface wind directions and speeds, and sources and supplies of sand, might be conducive to yardang burial and preservation.

Wind-parallel linear loess topography is not restricted to the Chinese Loess Plateau (Fig. 2). It is also present in European loess (know there as *greda*) and the Peoria Loess and Palouse Loess of the American Midwest and Pacific Northwest, respectively (known there as *paha*). The linear nature of the topography has been interpreted to be of dominantly erosional origin (Sweeney and Mason, 2013) or depositional origin, either as linear dunes of loess (Flemal et al., 1972; Leger, 1990) or preferential loess accumulation in the lee of topographic/vegetation obstacles (Lewis, 1960; Mason et al., 1999). Additional studies are needed to better understand the mechanisms by which linear loess topography develops and the extent to which its orientation reflects modern and/or last glacial period geomorphically-effective winds. We speculate that wind-parallel linear topography is a characteristic of relatively sandy loess, and like yardangs, has potential to be preserved in the stratigraphic record if specific criteria are met.

5.2. Potential linkages between wind processes and tectonics

Potential linkages between wind processes and rock deformation are largely unexplored. We pose that wind erosion may have influenced the rates and kinematics of folding in the Qaidam fold belt (Fig. 18) and the orientations of joints in Hami Basin yardangs (Fig. 38). Looking more broadly, many of Earth's most extreme regions of bedrock wind erosion, as exemplified by the presence of yardang fields (Fig. 1), are undergoing tectonically-driven surface uplift. Tectonics enhances wind erosion by uplifting rocks above the erosion surface and generating topographic obstacles and corridors which can accelerate near-surface wind velocities (Jackson and Hunt, 1975; Laity, 1987). The most significant yardang field in the American Southwest (Ocotillo Wells, southernmost California; not shown on Fig. 1) is in Pleistocene (~1.1 – 0.5 Ma) strata that are being folded and wind eroded at rates of several mm/yr (Pelletier et al., 2018) within a dextral wrench tectonic setting associated with the San Andreas fault system (Kirby et al., 2007; Janecke et al., 2010). Coastal yardangs in western South America are spatially localized to the Peruvian forearc where the inactive Nazca Ridge is subducting at low angle beneath the South American Plate because of its relatively thick and buoyant oceanic crust

(Bishop et al., 2017) (Fig. 1). The remainder of South America's yardang fields are associated with the active Andean orogenic belt (Fig. 1). Wind erosion in southern Africa, the Sahara, and in Arabia could be enhanced by dynamic surface uplift associated with buoyant upwelling mantle (Lithgow-Bertelloni and Silver, 1998) and surface uplift along the flanks of the active Red Sea rift. The field of eolian geology is mature, but that of integrative solid Earth tectonics – bedrock geology – topography – eolian – atmospheric system science is still emerging.

5.3. Chinese Loess Plateau

Wind processes not only built the Chinese Loess Plateau, but also moved its windward margin up to ~200 km downwind as the endorheic Mu Us Desert expanded southward and eastward (Fig. 27). The idea that Loess Plateau strata were deposited and then uplifted and incised by rivers is a misconception. The Loess Plateau was built because the net volume of eolian sedimentation exceeded the net volume of sediment removed by rivers (Fig. 27). Where the Loess Plateau is least fluvially incised, its highest points are at similar elevations over lateral distances of hundreds of kilometers (Fig. 21), justifying its nomenclature as a physiographic plateau. How this regional flatness was achieved and maintained, however, remains an open question for future research. The Loess Plateau needs further consideration as an enormous and dynamic eolian landform; it offers a unique laboratory for simulation in, and tuning of numerical landscape evolution models that couple fluvial and eolian processes.

While the leaf-blower analogy provides a simple mechanism for how to simultaneously build and erode a plateau of dust (Fig. 28), the role of tectonics can once again not be neglected. Tectonics exerts the dominant control on changing topography; topography in turn influences surface wind directions and velocities as well as spatial variations in precipitation, which in turn influences where and how much dust will accumulate (or erode). The potential interplays among orography (e.g., the northeastern margin of the Tibetan Plateau, Luliang and Qinling mountains, and the relatively high-elevation Loess Plateau itself), pre-existing bedrock topography, surface wind directions and velocities, and spatial gradients in precipitation and loess mass accumulation rates offer exciting avenues of future research on the Loess Plateau and other loess accumulations globally.

5.4. Deflationary basins

The western Qaidam and Hami basins and Mu Us Desert are not the only significantly wind-scoured endorheic regions in central Asia. Approximately 400-500 km to the northeast of the Mu Us Desert is the >8000 km^2 Sunite deflationary basin (Yin et al., 2023) (Fig. 2). Down-wind to the east of the Sunite basin is the Otindag sand sea. In between the Hami and western Qaidam basins are impressive yardang fields of Yardang National Geopark (Dong et al., 2012a; Wang et al., 2016) and the ~18,000 km^2 Lop Nur Depression (Dong et al., 2012b; Lin et al., 2018), both of which lie upwind of sand seas (Fig. 2). North of the eastern Tian Shan is the Junggar Basin, the northern part of which is strongly deflationary and/or wind scoured upwind (to the north) of the Gurbantünggüt sand sea. These and other vast areas in Asia, including regions that are wetter and more vegetated now than during past glacial periods, remain frontiers for future Earth system science research.

Wind has scoured 100-km-scale depressions with hundreds of meters (or more) of relief in other arid, or formerly arid regions on Earth (Knight, 2019). Examples include the ~19,000 km^2 Qattara Depression of the Western Desert of Egypt (Albritton Jr. et al., 1990) and probably other large endorheic regions in Africa like the Bodélé Depression (Washington et al., 2006) (Fig. 1). Wind removed a thickness of up to two kilometers of strata from the 300 km^2 Salina del Fraile Basin in the southern Puna Plateau of northwestern Argentina (Fig. 1) (Goudie and Wells, 1995; McMillan and Schoenbohm, 2020). An outstanding question is the extent to which wind erosion generated or amplified preexisting closed topographic depressions. The net expansion of the Mu Us Desert shows that wind erosion is capable of outpacing fluvial incision and transitioning regions of prior external drainage into endorheic basins. Future integrated digital elevation model analysis and geologic and geomorphic mapping have strong potential to quantify volumes of sediment removed from wind-scoured basins globally. Challenging in places where informative sedimentary records are absent will be unraveling how wind erosion rates varied through time.

5.5. Evolving landscapes, winds, and sources and fluxes of dust

Dramatic changes in the landscape and climate of central Asia at million-year and glacial-interglacial (40-100 kyr) timescales likely impacted the sources and fluxes of Asian dust through time. Wind erosion initiated in the western Qaidam Basin at ~3 Ma and likely increased dramatically in spatial extent and magnitude during the Pleistocene as the climate became more

arid and sedimentary rocks were tectonically uplifted to subaerial conditions. The Qaidam Basin is a modest source of dust in the modern climate but was likely a dust hotspot—perhaps akin to the modern Bodélé Depression (Todd et al., 2007)—during glacial periods of the mid-to-late Pleistocene.

The Mu Us Desert was a major sink of dust during the Neogene – early Pleistocene when Loess Plateau strata extended farther to the north of its modern extent (Fig. 27). During Pleistocene aridification and expansion of Asian deserts, the Mu Us Desert transitioned from a dust sink to a dust source as the windward escarpment margin of the Loess Plateau was eroded by wind processes and retreated downwind. Reworking of loess by wind processes was likely a major process contributing to dust emissions in Asia during late Pleistocene time.

In contrast to the Qaidam Basin and Mu Us Desert, the Gobi Desert might have been a much higher emitter of dust during the early Pleistocene when its landscape was likely more fertile with silt and less extensively armored by gravel-dominated surfaces. Dust flux records from the Sea of Japan and North Pacific suggest that from early to late Pleistocene time, dust flux either increased (Anderson et al., 2020; Zhang et al., 2020b; Zhang et al., 2020c), remained relatively stable (Rea et al., 1998; Lee et al., 2022; Tang et al., 2022), decreased (Zhang et al., 2016; Abell et al., 2023), and/or reflects a complex evolution in Asian dust dynamics (Abell et al., 2023; Zhong et al., 2023). An increase in dust flux through the Quaternary might be expected given the general trend toward increased Asian aridity, whereas a decrease in dust flux might implicate changes in landscape evolution (e.g., development of Gobi Desert landscape) and decreased dust fertility in response to a combination of gravel armoring and a decrease in silt production under more arid climates (Abell et al., 2023).

Based on the case studies of the Qaidam Basin, Mu Us Desert, Loess Plateau, and Hami Basin reviewed herein, Asian dust dynamics were likely extremely dynamic as the climate, landscape, topography, and geology evolved throughout Pliocene – Quaternary time. A potentially major factor that we have neglected is the expansion of mountain glaciers in central Asia since mid-Pleistocene time, which would have provided an additional glaciogenic dust flux component to consider and one that is richer in biologically reactive reduced iron and other metals than Asian desert dust (Koffman et al., 2021; Zan et al., 2023). Future major advances in understanding will likely require holistic investigations that simultaneously assess all these changing factors. Conceptual models for how central Asia's sandy deserts evolved (e.g.,

Taklamakan, Badain Jaran, and Tengger; Fig. 2) remain to be further developed (Dong et al., 2012b; Li et al., 2014; Wang et al., 2015a). High spatial resolution numerical weather and climate models should aim to simulate the modern near surface geomorphically-effective wind pattern (Fig. 2) and dust storm events—a requisite for being able to confidently simulate winds and dust emissions under past landscape and climate conditions.

Declaration of Competing Interest

The authors declare that they have no known competing financial interests or personal relationships that could have appeared to influence the work reported in this paper.

Acknowledgements

This research was supported by the U.S. National Science Foundation grant number 1545859. We thank reviewers John Douglass and Jinbo Zan for helping us clarify arguments strengthen the manuscript. We thank Fulong Cai, Richard Heermance, Jon D. Pelletier, and Alexander Rohrmann for companionship and discussions during fieldwork and Lin Ding for logistical support. The content in this manuscript was additionally influenced by discussions with Robert F. Anderson, Feng Cheng, Carmala Garzione, Lin Li, Peter Molnar, Junsheng Nie, Joellen Russell, and Gisela Winckler, among many others.

References

Abell, J.T., Pullen, A., Lebo, Z.J., Kapp, P., Gloege, L., Metcalf, A.R., Nie, J., Winckler, G., 2020a. A wind-albedo-wind feedback driven by landscape evolution. Nat. Commun. 11, 96.

Abell, J.T., Rahimi, S.R., Pullen, A., Lebo, Z.J., Zhang, D., Kapp, P., Gloege, L., Ridge, S., Nie, J., Winckler, G., 2020b. A quantitative model-based assessment of stony desert landscape evolution in the Hami Basin, China: Implications for Plio-Pleistocene dust production in eastern Asia. Geophys. Res. Lett. 47, e2020GL090064.

Abell, J.T., Winckler, G., Anderson, R.F., Herbert, T.D., 2021. Poleward and weakened westerlies during Pliocene warmth. Nature 589, 70–75.

Abell, J.T., Winckler, G., Pullen, A., Kinsley, C.W., Kapp, P.A., Middleton, J.L., Pavia, F.J., McGee, D., Ford, H.L., Raymo, M.E., 2023. Evaluating the drivers of Quaternary dust

fluxes to the western North Pacific: East Asian dustiness and Northern Hemisphere gustiness. Paleoceanography and Paleoclimatology 38, e2022PA004571.

Aciego, S.M., Riebe, C.S., Hart, S.C., Blakowski, M.A., Carey, C.J., Aarons, S.M., Dove, N.C., Botthoff, J.K., Sims, K.W.W., Aronson, E.L., 2017. Dust outpaces bedrock in nutrient supply to montane forest ecosystems. Nat. Commun. 8, 14800.

Albritton Jr., C.C., Brooks, J.E., Issawi, B., Swedan, A., 1990. Origin of the Qattara Depression, Egypt. Geol. Soc. Am. Bull. 102, 952–960.

Allen, M.B., Windley, B.F., Zhang, C., Guo, J., 1993. Evolution of the Turfan basin, Chinese central Asia. Tectonics 12, 889–896.

An, Z., 2000. The history and variability of the East Asian paleomonsoon climate. Quat. Sci. Rev. 19, 171–187.

Anderson, C.H., Murray, R.W., Dunlea, A.G., Giosan, L., Kinsley, C.W., McGee, D., Tada, R., 2020. Aeolian delivery to Ulleung Basin, Korea (Japan Sea), during development of the East Asian Monsoon through the last 12 Ma. Geol. Mag. 157, 806–817.

Anderson, R.S. and Hallet, B., 1986. Sediment transport by wind: Toward a general model. Geol. Soc. Am. Bull. 97, 523–535.

Anglés, A., Li, Y., 2017. The western Qaidam Basin as a potential Martian environmental analogue: An overview. J. Geophys. Res.: Planets 122, 856–888.

Bakker, N.L., Drake, N.A., Bristow, C.S., 2019. Evaluating the relative importance of northern African mineral dust sources using remote sensing. Atmos. Chem. Phys. 19, 10525–10535.

Bao, J., Wang, Y., Song, C., Feng, Y.-X., Hu, C., Zhong, S., Yang, J., 2017. Cenozoic sediment flux in the Qaidam Basin, northern Tibetan Plateau, and implications with regional tectonics and climate. Global Planet. Change 155, 56–69.

Barchyn, T.E., Hugenholtz, C.H., 2015. Yardang evolution from maturity to demise. Geophys. Res. Lett. 42, 5865–5871.

Beaumont, C., Jamieson, R.A., Nguyen, M.H., Lee, B., 2001. Himalayan tectonics explained by extrusion of a low-viscosity crustal channel coupled to focused surface denudation. Nature 414, 738–742.

Berger, A.L., Gulick, S.P.S., Spotila, J.A., Upton, P., Jaeger, J.M., Chapman, J.B., Worthington, L.A., Pavlis, T.L., Ridgway, K.D., Willems, B.A., McAleer, R.J., 2008. Quaternary

tectonic response to intensified glacial erosion in an orogenic wedge. Nat. Geosci. 1, 793–799.

Bettinelli, P., Avouac, J.-P., Flouzat, M., Bollinger, L., Ramillien, G., Rajaure, S., Sapkota, S., 2008. Seasonal variations of seismicity and geodetic strain in the Himalaya induced by surface hydrology. Earth Planet. Sci. Lett. 266, 332–344.

Bishop, B.T., Beck, S.L., Zandt, G., Wagner, L., Long, M., Antonijevic, S.K., Kumar, A., Tavera, H., 2017. Causes and consequences of flat-slab subduction in southern Peru. Geosphere 13, 1392–1407.

Blackwelder, E., 1934. Yardangs. Geol. Soc. Am. Bull. 45, 159–166.

Bohm, K., Kaakinen, A., Stevens, T., Lahaye, Y., O'Brien, H., Tang, H., Shang, Y., Zhang, H., Lu, H., 2023. Neogene global climate change and East Asian dust sources: Combined rutile geochemistry and zircon U-Pb analysis from the northern Chinese Loess Plateau. Global Planet. Change 221, 104049.

Bollinger, L., Perrier, F., Avouac, J.-P., Sapkota, S., Gautam, U., Tiwari, D.R., 2007. Seasonal modulation of seismicity in the Himalaya of Nepal. Geophys. Res. Lett. 34, L08304.

Bopp, L., Kohfeld, K.E., Le Quere, C., Aumont, O., 2003. Dust impact on marine biota and atmospheric CO_2 during glacial periods. Paleoceanography 18, 1046.

Bowler, J.M., Chen, K., Yuan, B., 1987. Systematic variations in loess source areas: Evidence from Qaidam and Qinghai basins, western China. Aspects of Loess Research. China Ocean Press, pp. 39–51.

Bowler, J.M., Qi, H., Kezao, C., Head, M.J., Baoyin, Y., 1986. Radiocarbon dating of playa-lake hydrologic changes: examples from northwestern China and central Australia. Palaeogeog. Palaeoclimatol. Palaeoecol. 54, 241–260.

Boy, J., Wilcke, W., 2008. Tropical Andean forest derives calcium and magnesium from Saharan dust. Global Biogeochemical Cycles 22, GB1027.

Bristow, C.S., Hudson-Edwards, K.A., Chappell, A., 2010. Fertilizing the Amazon and equatorial Atlantic with West African dust. Geophys. Res. Lett. 37, L14807.

Brookes, I.A., 2001. Aeolian erosional ineations in the Libyan Desert, Dakhla Region, Egypt. Geomorphology 39, 189–209.

Bryan, R.B., 2000. Soil erodibility and processes of water erosion on hillslope. Geomorphology 32, 385–415.

Cai, M., Fang, X., Wu, F., Miao, Y., Appel, E., 2012. Pliocene-Pleistocene stepwise drying of Central Asia: Evidence from paleomagnetism and sporopollen record of the deep borehole SG-3 in the western Qaidam Basin, NE Tibetan Plateau. Glob. Planet. Change 94–95, 72–81.

Chapman, C.A., 1958. Control of jointing by topography. J. Geol. 66, 552–558.

Chen, G., Held, I.M., 2007. Phase speed spectra and the recent poleward shift of Southern Hemisphere surface westerlies. Geophys. Res. Lett. 34, L21805.

Chen, K., Bowler, J.M., 1986. Late Pleistocene evolution of salt lakes in the Qaidam basin, Qinghai Province, China. Palaeogeog. Palaeoclimatol. Palaeoecol. 54, 87–104.

Cheng, F., Jolivet, M., Guo, Z., Lu, H., Zhang, B., Li, X., Zhang, D., Zhang, C., Zhang, H., Wang, L., Wang, Z., Zhang, Q., 2019. Jurassic-Early Cenozoic tectonic inversion in the Qilian Shan and Qaidam Basin, North Tibet: New insight from seismic reflection, isopach mapping, and drill core data. J. Geophys. Res.: Solid Earth 124, 12077–12098.

Cheng, F., Jolivet, M., Guo, Z., Wang, L., Zhang, C., Li, X., 2021. Cenozoic evolution of the Qaidam basin and implications for the growth of the northern Tibetan plateau: A review. Earth-Sci. Rev. 220, 103730.

Clinkscales, C., Kapp, P., Thomson, S., Wang, H., Laskowski, A., Orme, D.A., Pullen, A., 2021. Regional exhumation and tectonic history of the Shanxi Rift and Taihangshan, North China. Tectonics 40, e2020TC006416.

Craddock, W.H., Kirby, E., Harkins, N.W., Zhang, H., Shi, X., Liu, J., 2010. Rapid fluvial incision along the Yellow River during headward basin integration. Nat. Geosci. 3, 209–213.

Cunningham, D., Owen, L.A., Snee, L.W., Jiliang, L., 2003. Structural framework of a major intracontinental orogenic termination zone: the easternmost Tien Shan, China. J. Geol. Soc. London 160, 575–590.

Dahlen, F.A., Suppe, J., Davis, D., 1984. Mechanics of fold-and-thrust belts and accretionary wedges: Cohesive Coulomb theory. J. Geophys. Res. 89, 10087–10101.

Davis, G.H., Reynolds, S.J., Kluth, C.F., 2012. Structural Geology of Rocks and Regions. John Wiley and Sons, Inc., 839 pp.

de Silva, S.L., Bailey, J.E., Mandt, K.E., Viramonte, J.M., 2010. Yardangs in terrestrial ignimbrites: Synergistic remote and field observations on Earth with application to Mars. Planet. Space Sci. 58, 459–471.

DeCelles, P.G., Carrapa, B., Horton, B.K., McNabb, J., Gehrels, G.E., Boyd, J., 2015. The Miocene Arizaro Basin, central Andean hinterland: Response to partial lithosphere removal? In: P.G. DeCelles, M.N. Ducea, B. Carrapa and P.A. Kapp (Editors), Geodynamics of a Cordilleran Orogenic System: The Central Andes of Argentina and Northern Chile. Geological Society of America Memoir 212, Boulder, pp. 359–386.

Dettman, D.L., Fang, X., Garzione, C.N., Li, J., 2003. Uplift-driven climate change at 12 Ma: a long $\delta^{18}O$ record from the NE margin of the Tibetan plateau. Earth Plane. Sci. Lett. 214, 267–277.

Ding, Z., Gong, S., Xiao, G., Wang, Y., Yuan, W., Zhang, J., Wang, J., Lai, Z., 2024. Episodic sediment accumulation linked to global change in the endorheic Qaidam Basin of the Tibetan Plateau revealed by feldspar luminescence dating. Quat. Geochronol. 81, 101522.

Ding, Z., Yu, L., Lai, Z., An, P., Miao, X., Xu, R., Liu, Z., 2021. Post-IR IRSL chronology of paleo-lacustrine sediments from yardangs in the Qaidam basin, NE Tibetan Plateau. Geochronometria 48, 313–324.

Ding, Z.L., Derbyshire, E., Yang, S.L., Sun, J.M., Liu, T.S., 2005. Stepwise expansion of desert environment across northern China in the past 3.5 Ma and implications for monsoon evolution. Earth Planet. Sci. Lett. 237, 45–55.

Ding, Z.L., Xiong, S.F., Sun, J.M., Yang, S.L., Gu, Z.Y., Liu, T.S., 1999. Pedostratigraphy and paleomagnetism of a ~7.0 Ma eolian loess-red clay sequence at Lingtai, Loess Plateau, north-central China and the implications for paleomonsoon evolution. Palaeogeogr. Palaeoclimatol. Palaeoecol. 152, 49–66.

Dong, Z., Lv, P., Lu, J., Qiang, G., Zhang, Z., Luo, W., 2012a. Geomorphology and origin of Yardangs in the Kumtagh Desert, Northwest China. Geomorphology 139–140, 145–154.

Dong, Z., Lv, P., Qian, G., Xia, X., Zhao, Y., Mu, G., 2012b. Research progress in China's Lop Nur. Earth-Sci. Rev. 111, 142–153.

Dromart, G., Le Deit, L., Rapin, W., Gasnault, O., Le Mouelic, S., Quantin-Nataf, C., Mangold, N., Rubin, D., Lasue, J., Maurice, S., Newsom, H.E., Pinet, P., Scuderi, L., Wiens, R.C.,

2021. Deposition and erosion of a Light-Toned Yardang-forming unit of Mt Sharp, Gale crater, Mars. Earth Plane. Sc. Lett. 554, 116681.

Duszyński, F., Migoń, P., Strzelecki, C., 2019. Escarpment retreat in sedimentary tablelands and cuesta landscapes - Landforms, mechanisms and patterns. Earth-Sci. Rev. 196, 102890.

Egholm, D.L., Nielsen, S.B., Pedersen, V.K., Lesemann, J.-E., 2009. Glacial effects limiting mountain height. Nature 460, 884–888.

Evans, J.R., 1962. Falling and climbing sand dunes in the Cronese ("Cat") Mountains area, San Bernardino County, California. J. Geol. 70, 107–113.

Fan, Q., Ma, H., Cao, G., Chen, Z., Cao, S., 2012. Geomorphic and chronometric evidence for high lake level history in Gahai Lake and Toson Lake of north-eastern Qaidam Basin, north-eastern Qinghai-Tibetan Plateau. J. Quat. Sci. 27, 819–827.

Fang, X., An, Z., Clemens, S.C., Zan, J., Shi, Z., Yang, S., Han, W., 2020. The 3.6-Ma aridity and westerlies history over midlatitude Asia linked with global climate cooling. PNAS 117, 24729–24734.

Flemal, R.C., Odom, I.E., Vail, R.G., 1972. Stratigraphy and origin of the paha topography of northwestern Illinois. Quat. Res. 2, 232–243.

Fu, B., 1989. Soil erosion and its control in the loess plateau of China. Soil Use and Management, 5, 76–82.

Gan, W., Zhang, P., Shen, Z.-K., Niu, Z., Wang, M., Wan, Y., Zhou, D., Cheng, J., 2007. Present-day crustal motion within the Tibetan Plateau inferred from GPS measurements. J. Geophys. Res. 112, B08416.

Gillette, D.A., Adams, J., Endo, A., Smith, D., Kihl, R., 1980. Threshold velocities for input of soil particles into the air by desert soils. J. Geophys. Res. 85, 5621–5630.

Göğüş, O.H., Pysklywec, R.N., 2008. Near-surface diagnostics of dripping or delaminating lithosphere. J. Geophys. Res. 113, B11404.

Goudie, A.S., 2007. Mega-Yardangs: A Global Analysis. Geography Compass 1, 65–81.

Goudie, A.S., 2008. The history and nature of wind erosion in deserts. Ann. Rev. Earth Planet. Sci. 36, 97–119.

Goudie, A.S., 2012. Charles Rollin Keyes and extravagant aeolation. Aeolian Res. 4, 51–53.

Goudie, A.S., Wells, G.L., 1995. The nature, distribution and formation of pans in arid zones. Earth-Sci. Rev. 38, 1–69.

Gulev, S.K., Thorne, P.W., Ahn, J., Dentener, F.J., Domingues, C.M., Gerland, S., Gong, D., Kaufman, D.S., Nnamchi, H.C., Quaas, J., Rivera, J.A., Sathyendranath, S., Smith, S.L., Trewin, B., von Schuckmann, K., Vose, R.S., 2021. Changing State of the Climate System. In: V. Masson-Delmotte, P. Zhai, A. Pirani, S.L. Connors, C. Péan, S. Berger, N. Caud, Y. Chen, L. Goldfarb, M.I. Gomis, M. Huang, K. Leitzell, E. Lonnoy, J.B.R. Matthews, T.K. Maycock, T. Waterfield, O. Yelekçi, R. Yu and B. Zhou (Editors), Climate Change 2021: The Physical Science Basis. Contribution of Working Group I to the Sixth Assessment Report of the Intergovernmental Panel on Climate Change. Cambridge University Press, Cambridge, United Kingdom and New York, NY, USA, pp. 287–422.

Guo, Z.T., Ruddiman, W.F., Hao, Q.Z., Wu, H.B., Qiao, Y.S., Zhu, R.X., Peng, S.Z., Wei, J.J., B.Y., Y., Liu, T.S., 2002. Onset of Asian desertification by 22 Myr ago inferred from loess deposits in China. Nature 416, 159–163.

Gutiérrez-Elorza, M., Desir, G., Gutiérrez-Santolalla, F., 2002. Yardangs in the semiarid central sector of the Ebro Depression (NE Spain). Geomorphology 44,155–170.

Halimov, M., Fezer, F., 1989. Eight yardang types in Central Asia. Zeitschrift fur Geomorphologie 33, 205–217.

Han, W., Fang, X., Ye, C., Teng, X., Zhang, T., 2014a. Tibet forcing Quaternary stepwise enhancement of westerly jet and central Asian aridification: Carbonate isotope records from deep drilling in the Qaidam salt playa, NE Tibet. Global Planet. Change 116, 68–75.

Han, W., Ma, Z., Lai, Z., Appel, E., Fang, X., Yu, L.P., 2014b. Wind erosion on the north-eastern Tibetan Plateau: constraints from OSL and U-Th dating of playa salt crust in the Qaidam Basin. Earth Surf. Process. Landf. 39, 779–789.

Haywood, A.M., Dowsett, H.J., Dolan, A.M., 2016. Integrating geological archives and climate models for the mid-Pliocene warm period. Nat. Commun. 7, 10646.

He, Z., Zhou, J., Lai, Z.P., Yang, L.H., Liang, J.M., Long, H., Ou, X.J., 2010. Quartz OSL dating of sand dunes of Late Pleistocene in the Mu Us Desert in northern China. Quat. Geochronology 5, 102–106.

Hedin, S.A., 1903. Central Asia and Tibet, 2. Hurst and Blakett, Limited and Charles Scribners Sons, London/New York, 664 pp.

Heermance, R.V., Pullen, A., Kapp, P., Garzione, C.N., Bogue, S., Ding, L., Song, P., 2013. Climatic and tectonic controls on sedimentation and erosion during the Pliocene-Quaternary in the Qaidam Basin (China). Geol. Soc. Am. Bull. 125, 833–856.

Herb, C., Koutsodendris, A., Zhang, W., Appel, E., Fang, X., Voigt, S., Pross, J., 2015. Late Plio-Pleistocene humidity fluctuations in the western Qaidam Basin (NE Tibetan Plateau) revealed by an integrated magnetic-palynological record from lacustrine sediments. Quat. Res. 84, 457–466.

Herbert, T.D., 2023. The Mid-Pleistocene Climate Transition. Ann. Rev. Earth Planet. Sci. 51, 389–418.

Hu, C., Chen, N., Kapp, P., Chen, J., Xiao, A., Zhao, Y., 2017. Yardang geometries in the Qaidam Basin and their controlling factors. Geomorphology 299, 142–151.

Huang, C.C., Pang, J., Zhao, X., Su, H., Zhou, Y., 2012. Development of gully systems under the combined impact of monsoonal climatic shift and neo-tectonic uplift over the Chinese Loess Plateau. Quat. Int. 263, 46–54.

Huang, K., Wu, L., Zhao, H., Zhang, J., Zhang, Y., Xiao, A., Chen, Y., Chen, H., 2021. Development and interplay of two orthogonal fault systems in the NW Qaidam Basin, northern Tibetan Plateau. Front. Earth Sci. 9, 637056.

Husar, R.B., Tratt, D.M., Schichtel, B.A., Falke, S.R., Li, F., Jaffe, D., Gasso, S., Gill, T.E., Laulainen, N.S., Lu, F., Reheis, M.C., Chun, Y., Westphal, D., Holben, B.N., Gueymard, C., McKendry, I., Kuring, N., Feldman, G.C., McClain, C., Frouin, R.J., Merrill, J., DuBois, D., Vignola, F., Murayama, T., Nickovic, S., Wilson, W.E., Sassen, K., Sugimoto, N., Malm, W.C., 2001. Asian dust events of April 1998. J. Geophys. Res. 106, 18317–18330.

Jackson, P.S., Hunt, J.C.R., 1975. Turbulent wind flow over a low hill. Quarterly J. Royal Meteorological Soc. 101, 929–955.

Janecke, S.U., Dorsey, R.J., Forand, D., Steely, A.N., Kirby, S.M., Lutz, A.T., Housen, B.A., Belgarde, B., Langenheim, V.E., Rittenour, T.M., 2010. High Geologic Slip Rates since Early Pleistocene Initiation of the San Jacinto and San Felipe Fault Zones in the San Andreas Fault System: Southern Calironia, USA. Geological Society of America Special Paper 475, pp. 48.

Jia, L., Zhang, X., Ye, P., Zhao, X., He, Z., He, X., Zhou, Q., Li, J., Ye, M., Wang, Z., Meng, J., 2016. Development of the allvuial and lacustrine terraces on the northern margin of the Hetao Basin, Inner Mongolia, China: Implications for the evolution of the Yellow River in the Hetao area since the late Pleistocene. Geomorphology 263, 87–98.

Jiang, L., Liu, Y., Li, W., Yuan, S., Yuan, J., LI, S., Liu, Z., 2022. Cenozoic double-layered structure in the western Qaidam Basin, northern Tibetan Plateau, China. J. Asian Earth Sci. 232, 105123.

Jickells, T.D., An, Z.S., Andersen, K.K., Baker, A.R., Bergametti, G., Brooks, N., Cao, J.J., Boyd, P.W., Duce, R.A., Hunter, K.A., Kawahata, H., Kubilay, N., laRoche, J., Liss, P.S., Mahowald, N.M., Prospero, J.M., Ridgwell, A.J., Tegen, I., Torres, R., 2005. Global iron connections between desert dust, ocean biogeochemistry, and climate. Science 308, 67–71.

Jin, X., Guo, R., Xia, W., 2013. Distribution of actual evapotranspiration over Qaidam Basin, an arid area in China. Remote Sensing 5, 6976–6996.

Jones, L., Blakey, R.C., 1993. Erosional remnants and adjacent unconformities along an eolian-marine boundary of the Page sandstone and Carmel Formation, Middle Jurassic, south-central Utah. J. Sediment. Petrol. 63, 852–859.

Kapp, P., DeCelles, P.G., 2019. Mesozoic-Cenozoic geological evolution of the Himalayan-Tibetan orogen and working tectonic hypotheses. Am. J. Sci. 319: 159–254.

Kapp, P., Pelletier, J.D., Rohrmann, A., Heermance, R., Russell, J. and Ding, L., 2011. Wind erosion in the Qaidam basin, central Asia: Implications for tectonics, paleoclimate, and the source of the Loess Plateau. GSA Today 21, 4–10.

Kapp, P., Pullen, A., Pelletier, J.D., Russell, J., Goodman, P., Cai, F., 2015. From dust to dust: Quaternary wind erosion of the Mu Us Desert and Loess Plateau, China. Geology 43, 835–838.

Keyes, C.R., 1912. Deflative scheme of the geographic cycle in an arid climate. Bull. Geol. Soc. Am. 23, 537–562.

Kirby, S.M., Janecke, S.U., Dorsey, R.J., Housen, B.A., Langenheim, V.E., McDougall, K.A., Steely, A.N., 2007. Pleistocene Brawley and Ocotillo Formations: Evidence for initial strike-slip deformation along the San Felipe and San Jacinto Fault Zones, Southern California. J. Geol. 115, 43–62.

Knight, J., 2019. Wind Erosion. In: I. Livingstone and A. Warren (Editors), Aeolian Geomorphology: A New Introduction. John Wiley and Sons Ltd., pp. 61–80.

Koffman, B.G., Yoder, M.F., Methven, T., Hanschka, L., Sears, H.B., Saylor, P.L., Wallace, K.L., 2021. Glacial dust surpasses both volcanic ash and desert dust in its iron fertilization potential. Glob. Biogeochem. Cycles 35, e2020GB006821.

Kohfeld, K.E., Harrison, S.P., 2003. Glacial-interglacial changes in dust deposition on the Chinese Loess Plateau. Quat. Sci. Rev. 22, 1859–1878.

Kok, J.F., Storelvmo, T., Karydis, V.A., Adebiyi, A.A., Mahowald, N.M., Evan, A.T., He, C., Leung, D.M., 2023. Mineral dust aerosol impacts on global climate and climate change. Nat. Rev. Earth Environ. 4, 71–86.

Kuhlbrodt, T., Griesel, A., Montoya, M., Levermann, A., Hofmann, M., Rahmstorf, S., 2007. On the driving processes of the Atlantic meridional overturning circulation. Rev. Geophys. 45, RG2001.

Kukla, G., An, Z., 1989. Loess stratigraphy in central China. Palaeogeogr. Palaeoclimatol. Palaeoecol. 72, 203–225.

Lai, Z.P., Mischke, S., Madsen, D., 2014. Paleoenvironmental implications of new OSL dates on the formation of the "Shell Bar" in the Qaidam Basin, northeastern Qinghai-Tibetan Plateau. J. Paleolimnol. 51, 197–210.

Laity, J.E., 1987. Topographic effects on ventifact development, Mojave Desert, California. Phys. Geogr. 8, 113–132.

Laity, J.E., 2011. Wind erosion in drylands. In: D.S.G. Thomas (Editor), Arid Zone Geomorphology: Process, Form and Change in Drylands. John Wiley & Sons, pp. 539–568.

Lee, A.M.F., Maruyama, A., Lu, S., Yamashita, Y., Irino, T., 2022. Quantification of Asian dust source variabilities in silt and clay fractions since 10 Ma by Parallel Factor (PARAFAC) endmember modeling at IODP Site U1425 in the Japan Sea. Lithosphere 2022, 6818103.

Leger, M., 1990. Loess landforms. Quat. Int. 7/8, 53–61.

Lewis, P.F., 1960. Linear topography in the southwestern Palouse, Washington-Oregon. Ann. Assoc. Am. Geogr. 50, 98–111.

Li, B., Feng, Q., Wang, F., Wang, X., Li, Z., Zhang, C., Guo, X., Liu, W., Li, R., 2020. A 1.68 Ma organic isotope record from the Hetao Basin, upper reaches of the Yellow River in

northern China: Implications for hydrological and ecological variations. Glob. Planet. Change 184, 103061.

Li, B., Feng, Q., Wang, X., Li, Z., Wang, F., Zhao, C., Yu, T., Chen, W., 2023. Formation of the upper reaches of the Yellow River: Provenance evidence from the strata of the Yellow River sedimentary basin. Glob. Planet. Change 229, 104224.

Li, B., Sun, D., Xu, W., Wang, F., Liang, B., Ma, Z., Wang, X., Li, Z., Chen, F., 2017. Paleomagnetic chronology and paleoenvironmental records from drill cores from the Hetao Basin and their implications for the formation of the Hobq Desert and the Yellow River. Quat. Sci. Rev. 156, 69–89.

Li, H., Mao, D., Li, X., Wang, Z., Wang, C., 2019. Monitoring 40-year lake area changes of the Qaidam Basin, Tibetan Plateau, using Landsat time series. Remote Sensing 11, 343.

Li, J., Dong, Z., Qian, G., Zhang, Z., Luo, W., Lu, J., Wang, M., 2016. Yardangs in the Qaidam Basin, northwestern China: Distribution and morphology. Aeolian Res. 20, 89–99.

Li, J., Fang, X., 1999. Uplift of the Tibetan Plateau and environmental changes. Chi. Sci. Bull. 44, 2117–2124.

Li, T., 2006. Geological Map of Western China and Adjacent Regions (1:2,500,000). In: X. Qi (Editor). Geological Publishing House, Beijing.

Li, Z., Sun, D., Chen, F., WaNg, F., Zhang, Y., Guo, F., Wang, X., Li, B., 2014. Chronology and paleoenvironmental records of a drill core in the central Tengger Desert of China. Quat. Sc. Rev. 85, 85–98.

Licht, A., Pullen, A., Kapp, P., Abell, J., Giesler, N., 2016. Eolian cannibalism: Reworked loess and fluvial sediment as the main sources of the Chinese Loess Plateau. Geol. Soc. Am. Bull. 128, 944–956.

Lin, Y., Xu, L., Mu, G., 2018. Differential erosion and the formation of layered yardangs in the Loulan region (Lop Nur), eastern Tarim Basin. Aeolian Res. 30, 41–47.

Lisiecki, L.E., Raymo, M.E., 2005. A Pliocene-Pleistocene stack of 57 globally distributed benthic $\delta^{18}O$ records. Paleoceanography 20, PA1003.

Lithgow-Bertelloni, C., Silver, P.G., 1998. Dynamic topography, plate driving forces and the African superswell. Nature 395, 269–272.

Liu, L.Y., Skidmore, E., Hasi, E., Wagner, L., Tatarko, J., 2005. Dune sand transport as influenced by wind directions, speed and frequencies in the Ordos Plateau, China. Geomorphology 67, 283–297.

Liu, R., Allen, M.B., Zhang, Q., Du, W., Cheng, X., Holdsworth, R.E., Guo, Z., 2017. Basement controls on deformation during oblique convergence: Transpressive structures in the western Qaidam Basin, northern Tibetan Plateau. Lithosphere 9, 583–594.

Liu, R., Chen, Y., Yu, X., Du, W., Cheng, X., Guo, Z., 2019. An analysis of distributed strike-slip shear deformation of the Qaidam Basin, northern Tibetan Plateau. Geophys. Res. Lett. 46, 4202–4211.

Liu, Z., Yongjin, W., Ye, C., Xuesong, L., Qingchen, L., 1998. Magnetostratigraphy and sedimentologically derived geochronology of the Quaternary lacustrine deposits of a 3000 m thick sequence in the central Qaidam basin, western China. Palaeogeogr. Palaeoclimatol. Palaeoecol. 140, 459–473.

Lu, H., Miao, X., Zhou, Y., Mason, J., Swinchart, J., Zhang, J., Zhou, L., Yi, S., 2005. Late Quaternary aeolian activity in the Mu Us and Otindag dune fields (north China) and lagged response to insolation forcing. Geophy. Res. Lett. 32, L21716.

Lu, Y., Fang, X., Appel, E., Wang, J., Herb, C., Han, W., Wu, F., Song, C., 2015. A 7.3–1.6 Ma grain size record of interaction between anticline uplift and climate change in the western Qaidam Basin, NE Tibetan Plateau. Sed. Geol. 319, 40–51.

Luo, L., Geissman, J.W., Zeng, X., Wang, B., Zhou, F., Zhang, Y., Yang, S., Zhou, Y., 2022. Geometry and kinematics of the western part of the NE Qaidam Basin: Implications for the growth of the Tibetan Plateau. Tectonophysics 822, 229154.

Maher, B.A., 2016. Palaeoclimatic records of the loess/palaeosol sequences of the Chinese Loess Plateau. Quat. Sci. Rev. 154, 23–84.

Mao, L., Xiao, A., Zhang, H., Wu, Z., Wang, L., Shen, Y.-h., Wu, L., 2016. Structural deformation pattern within the NW Qaidam Basin in the Cenozoic era and its tectonic implications. Tectonophysics 687, 78–93.

Martel, S.J., 2017. Progress in understanding sheeting joints over the past two centuries. J. Struct. Geol. 94, 68–86.

Mason, J.A., Nater, E.A., Zanner, C.W., Bell, J.C., 1999. A new model of topographic effects on the distribution of loess. Geomorphology 28, 223–236.

Mason, J.A., Swinehart, J.B., Lu, H., Miao, X., Cha, P., Zhou, Y., 2008. Limited change in dune mobility in response to a large decrease in wind power in semi-arid northern China since the 1970s. Geomorphology 102, 351–363.

McCauley, J.F., Grolier, M.J., Breed, C.S., 1977. Yardangs. In: D.O. Doehring (Editor), Geomorphology In Arid Regions, Binghamton, NY, pp. 233–272.

McFadden, L.D., Wells, S.G., Jercinovich, M.J., 1987. Influences of eolian and pedogenic processes on the origin and evolution of desert pavements. Geology 15, 504–508.

McGee, D., Broecker, W.S., Winckler, G., 2010. Gustiness: The driver of glacial dustiness? Quat. Sci. Rev. 29, 2340–2350.

McMillan, M., Schoenbohm, L.M., 2020. Large-scale Cenozoic wind erosion in the Puna Plateau: The Salina del Fraile depression. J. Geophys. Res.: Earth Surface 125, e2020JF005682.

Meijer, N., van der Meulen, B., 2023. Loss of loess in the geological record due to poor preservation. Terra Nova 35, 185–192.

Meng, Q.-R., Fang, X., 2008. Cenozoic tectonic development of the Qaidam Basin in the northeastern Tibetan Plateau. In: B.C. Burchfiel and E. Wang (Editors), Investigations into the Tectonics of the Tibetan Plateau. Geological Society of America Special Paper 444, Boulder, pp. 1–24.

Miao, Y., Fang, X., Herrmann, M., Wu, F., Zhang, Y., Liu, D., 2011. Miocene pollen record of KC-1 core in the Qaidam Basin, NE Tibetan Plateau and implications for evolution of the East Asian monsoon. Palaeogeogr. Palaeoclimatol. Palaeoecol. 299, 30–38.

Middleton, N., 2020. Health in dust belt cities and beyond-an essay by Nick Middleton. BMJ, 371, m3089.

Mildrexler, D.J., Zhao, M.,Running, S.W., 2011. Satellite finds highest land skin temperatures on Earth. Bull. Am. Meteor. Soc. July, 855–860.

Mischke, S., Sun, Z., Herzschuh, U., Qiao, Z., Sun, N., 2010. An ostracod-inferred large Middle Pleistocene freshwater lake in the presently hyper-arid Qaidam Basin (NW China). Quat. Int. 218, 74–85.

Molnar, P., 2004. Interactions among topographically induced elastic stress, static fatigue, and valley incision. J. Geophys. Res. 109, F02010.

Molnar, P., Houseman, G.A., 2004. The effects of buoyant crust on the gravitational instability of thickened mantle lithosphere at zones of intractontinental convergence. Geophys. J. Int. 158, 1134–1150.

Montgomery, D.R., Balco, G., Willett, S.D., 2001. Climate, tectonics, and the morphology of the Andes. Geology 29, 579–582.

Montgomery, D.R., Brandon, M.T., 2002. Topographic controls on erosion rates in tectonically active mountain ranges. Earth Planet. Sci. Lett. 201, 481–489.

Montgomery, D.R., Stolar, D.B., 2006. Reconsidering Himalayan river anticlines. Geomorphology 82, 4–15.

Moore, C.M., Mills, M.M., Arrigo, K.R., Berman-Frank, I., Bopp, L., Boyd, P.W., Galbraith, E.D., Geider, R.J., Guieu, C., Jaccard, S.L., Jickells, T.D., La Roche, J., Lenton, T.M., Mahowald, N.M., Maranon, E., Marinov, E., Moore, J.K., Nakatsuka, T., Oschlies, A., Saito, M.A., Thingstand, T.F., Tsuda, A., Ulloao, O., 2013. Processes and patterns of oceanic nutrient limitation. Nat. Geosci. 6, 701–710.

Muhs, D.R., 2013. The geologic records of dust in the Quaternary. Aeolian Res. 9, 3–48.

Muhs, D.R., Prospereo, J.M., Baddock, M.C., Gill, T.E., 2014. Identifying sources of aeolian mineral dust: present and past. In: P. Knippertz and J.-B.W. Stuut (Editors), Mineral Dust: A Key Player in the Earth System. Springer Science, pp. 51–74.

Nie, J., Stevens, T., Rittner, M., Stockli, D., Garzanti, E., Limonta, M., Bird, A., Ando, S., Vermeesch, P., Saylor, J., Lu, H., Breecker, D., Hu, X., Liu, S., Resentini, A., Vezzoli, G., Peng, W., Carter, A., Ji, S., Pan, B., 2015. Loess Plateau storage of northeastern Tibetan Plateau-derived Yellow River sediment. Nat. Commun. 6, 8511.

Nobakht, M., Shahgedanova, M., White, K., 2021. New inventory of dust emission sources in Central Asia and northwestern China derived from MODIS imagery using dust enhancement technique. J. Geophys. Res.: Atmospheres 126, e2020JD033382.

Nugteren, G., Vandenberghe, J., 2004. Spatial climatic variability on the Central Loess Plateau as recorded by grain size for the last 250 kyr. Glob. Planet. Change 41, 185–206.

Orme, A.R., 2013. Denudation, planation, and cyclicity: myths, models, and reality. Treatise on Geomorphology 1, 205–232.

Peizhen, Z., Burchfiel, B.C., Molnar, P., Weiqi, Z., Dechen, J., Qidong, D., Yipeng, W., Royden, L., Fangmin, S., 1991. Amount and style of late Cenozoic deformation in the Liupan Shan area, Ningxia Autonomous Region, China. Tectonics 10, 1111–1129.

Pelletier, J.D., 2018. Controls on yardang development and morphology: 2. Numerical modeling. J. Geophys. Res.: Earth Surf. 123, 723–743.

Pelletier, J.D., Kapp, P., Abell, J., Field, J.P., Williams, Z.C., Dorsey, R.J., 2018. Controls on yardang development and morphology: 1. Field observations and measurements at Ocotillo Wells, California. J. Geophys. Res.: Earth Surf. 123, 694–722.

Peng, W., Zhang, H., Pullen, A., Li, M., Pan, B., Xia, W., Nie, J., 2023. Stepwise increased spatial provenance contrast on the Chinese Loess Plateau over late Miocene-Pleistocene. Nat. Commun. Earth and Environ. 4, 60.

Porter, S.C., 2007. LOESS RECORDS | China. In: A.E. Scott (Editor), Encyclopedia of Quaternary Science. Elsevier, Oxford, pp. 1429–1440.

Porter, S.C., An, Z., 2005. Episodic gullying and paleomonsoon cycles on the Chinese Loess Plateau. Quat. Res. 64, 234–241.

Porter, S.C., Hallet, B., Wu, X., An, Z., 2001. Dependence of near-surface magnetic susceptibility on dust accumulation rate and precipitation on the Chinese Loess Plateau. Quat. Res. 55, 271–283.

Potter, S., Lehmkuhl, F., Weise, J., Zykina, V.S., Zykin, V.S., 2023. Spatiotemporal model for the evolution of a mega-yardang system in the foreland of the Russian Altai. Aeolian Res. 61, 100866.

Prospero, J.M., Ginoux, P., Torres, O., Nicholson, S.E., Gill, T.E., 2002. Environmental characterization of global sources of atmospheric soil dust identified with the Nimbus 7 Total Ozone Mapping Spectrometer (TOMS) absorbing aerosol product. Rev.Geophys. 40, 1002.

Pullen, A., Barbeau Jr., D.L., Leier, A.L., Abell, J.T., Ward, M., Bruner, A., Fidler, M.K., 2022. A westerly wind dominated Puna Plateau during deposition of upper Pleistocene loessic sediments in the subtropical Andes, South America. Nat. Commun. 13, 3411.

Pullen, A., Kapp, P., Chen, N., 2018. Development of stratigraphically controlled, eolian-modified unconsolidated gravel surfaces and yardang fields in the wind-eroded Hami Basin, northwestern China. Geol. Soc. Am. Bull. 130, 630–648.

Pullen, A., Kapp, P., McCallister, A.T., Chang, H., Gehrels, G.E., Garzione, C.N., Heermance, R.V., Ding, L., 2011. Qaidam Basin and northern Tibetan Plateau as dust sources for the Chinese Loess Plateau and paleoclimatic implications. Geology 39, 1031–1034.

Qiang, M., Lang, L., Wang, Z., 2010. Do fine-grained components of loess indicate westerlies: Insights from observations of dust storm deposits at Lenghu (Qaidam Basin, China). J. Arid Environ. 74, 1232–1239.

Qiang, X.K., Li, Z.X., Powell, C.M.c.A., Zheng, H.B., 2001. Magnetostratigraphic record of the Late Miocene onset of the East Asian monsoon, and Pliocene uplift of northern Tibet. Earth Planet. Sci. Lett. 187, 83–93.

Quade, J. Kaplan, M.R., 2017. Lake-level stratigraphy and geochronology revisted at Lago (Lake) Cardiel, Argentina, and changes in the Southern Hemispheric Westerlies over the last 25 ka. Quat. Sci. Rev. 177, 173–188.

Rea, D.K., Snoeckx, H., Joseph, L.H., 1998. Late Cenozoic eolian deposition in the North Pacific: Asian drying, Tibetan uplift, and cooling of the northern hemisphere. Paleoceanography, 13, 215–224.

Reiners, P.W., Ehlers, T.A., Mitchell, S.G., Montgomery, D.R., 2003. Coupled spatial variations in precipitation and long-term erosion rates across the Washington Cascades. Nature, 426, 645–647.

Rieser, A.B., Bojar, A.-V., Neubauer, F., Genser, J., Liu, Y., Ge, X.-H., Friedl, G., 2009. Monitoring Cenozoic climate evolution of northeastern Tibet: stable isotope constraints from the western Qaidam Basin, China. Int. J. Earth Sci. 98, 1063–1075.

Roe, G., 2009. On the interpretation of Chinese loess as a paleoclimate indicator. Quat. Res. 71, 150–161.

Rohrmann, A., Heermance, R., Kapp, P. Cai, F., 2013. Wind as the primary driver of erosion in the Qaidam Basin, China. Earth Planet. Sci. Lett. 374, 1–10.

Rubin, D.M., Hesp, P.A., 2009. Multiple origins of linear dunes on Earth and Titan. Nat. Geos. 2, 653–658.

Savage, W.Z., Swolfs, H.S., 1986. Tectonic and gravitational stress in long symmetric ridges and valleys. J. Geophys. Res. 91, 3677–3685.

Schwarz, F., Salzmann, U., Koutsodendris, A., Nie, J., Friedrich, O., Ni, J., Garzione, C., Fang, X., Wu, F., Woodward, J., Appel, E., Pross, J., 2022. Controls of precipitation and

vegetation variability on the NE Tibetan Plateau during the late Pliocene warmth (~3.5–3.0 Ma). Glob. Planet. Change 208, 103707.

Sebe, K., Csillag, G., Ruszkiczay-Rudiger, Z., Fodor, L., Thamo-Bozso, E., Muller, P., Braucher, R., 2011. Wind erosion under cold climate: A Pleistocene periglacial mega-yardang system in Central Europe (Western Pannonian Basin, Hungary). Geomorphology 134, 470–482.

Simpson, G., 2004. Role of river incision in enhancing deformation. Geology 32, 341–344.

Song, T., Wang, X., 1993. Structural styles and stratigraphic patterns of syndepositional faults in a contractional setting: Examples from Quaidam basin, northwestern China. Am. Assoc. Petrol. Geol. Bull. 77, 102–117.

Stevens, T., Buylaert, J.-P., Thiel, C., Ujvari, G., Yi, S., Murray, A.S., Frechen, M., Lu, H., 2018. Ice-volume-forced erosion of the Chinese Loess Plateau global Quaternary stratotype site. Nat. Commun. 9, 983.

Stevens, T., Carter, A., Watson, T.P., Vermeesch, P., Ando, S., Bird, A.F., Lu, H., Garzanti, E., Cottam, M.A., Sevastjanova, I., 2013. Genetic linkage between the Yellow River, the Mu Us desert and the Chinese Loess Plateau. Quat. Sci. Rev. 78, 355–368.

Stubbins, B., Leier, A.L., Barbeau Jr., D.L., Pullen, A., Abell, J.T., Nie, J., Zarate, M.A., Fidler, M.K., 2023. Global climate forcing on late Miocene establishment of the Pampean aeolian system in South America. Nat. Commun. 14, 6899.

Su, Q., Nie, J., Han, W., Garzione, C.N., Gao, P., 2024. Obliquity forcing of Late Pliocene-Early Pleistocene aridification in the Qaidam Basin, NE Tibetan Plateau. Palaeogeogr. Palaeoclimatol. Palaeoecol. 635, 111951.

Sun, J., 2002. Provenance of loess material and formation of loess deposits on the Chinese Loess Plateau. Earth Planet. Sci. Lett. 203, 845–859.

Sun, J., Zhang, M., Liu, T., 2001. Spatial and temporal characteristics of dust storms in China and its surrounding regions, 1960-1999: Relations to source area and climate. J. Geophys. Res. 106, 10325–10333.

Sun, Y., An, Z., 2005. Late Pliocene-Pleistocene changes in mass accumulation rates of eolian deposits on the central Chinese Loess Plateau. J. Geophys. Res. 110, D23101.

Sun, Y., Clemens, S.C., Morrill, C., Lin, X., Wang, X., An, Z., 2011. Influence of Atlantic meridional overturning circulation on the East Asian winter monsoon. Nat. Geosci. 5, 46–49.

Sun, Y., Tada, R., Chen, J., Liu, Q., Toyoda, S., Tani, A., Ji, J., Isozaki, Y., 2008. Tracing the provenance of fine-grained dust deposited on the central Chinese Loess Plateau. Geophys. Res. Lett. 35, L01804.

Suppe, J., Chou, G.T., Hook, S.C., 1992. Rates of folding and faulting determined from growth strata. In: K.R. McClay (Editor), Thrust Tectonics. Chapman and Hall, London, pp. 105–122.

Sweeney, M.R., Mason, J.A., 2013. Mechanisms of dust emission from Pleistocene loess deposits, Nebraska, USA. J. Geophys. Res.: Earth Surface 118, 1460–1471.

Sweeney, M.R., McDonald, E.V., Etyemezian, V., 2011. Quantifying dust emissions from desert landforms, eastern Mojave Desert, USA. Geomorphology 135, 21–34.

Tang, Y., Wan, S., Clift, P.D., Zhao, D., Xu, Z., Zhang, J., Song, Z., Jin, H.T., Li, M., Shi, X., Li, A., 2022. Northward shift of the Northern Hemisphere Westerlies in the early to late Miocene and its links to Tibetan uplift. Geophys. Res. Lett. 49, e2022GL099311.

Taylor, M., Yin, A., 2009. Active structures of the Himalayan-Tibetan orogen and their relationships to earthquake distribution, contemporary strain field, and Cenozoic volcanism. Geosphere 5, 199–214.

Tewes, D.W., Loope, D.B., 1992. Palaeo-yardangs: wind-scoured desert landforms at the Permo-Triassic unconformity. Sedimentology 39, 251–261.

Todd, M.C., Washington, R., Martins, J.V., Dubovik, O., Lizcano, G., M'Bainayel, S., Engelstaedter, S., 2007. Mineral dust emission from the Bodélé Depression, northern Chad, during BoDEx 2005. J. Geophys. Res. 112, D06207.

Toggweiler, J.R., Russell, J., 2008. Ocean circulation in a warming climate. Nature 451, 286–288.

Toggweiler, J.R., Russell, J.L., Carson, S.R., 2006. Midlatitude westerlies, atmospheric CO_2, and climate change during the ice ages. Paleoceanography 21, PA2005.

Toggweiler, J.R., Samuels, B., 1995. Effect of Drake Passage on the global thermohaline circulation. Deep-Sea Res. I 42, 477–500.

Tungsheng, L., Zhongli, D., 1993. Stepwise coupling of monsoon circulations to global ice volume variations during the late Cenozoic. Glob. Planet. Change 7, 119–130.

Uno, I., Eguchi, K., Yumimoto, K., Takemura, T., Shimizu, A., Uematsu, M., Liu, Z., Wang, Z., Hara, Y., Sugimoto, N., 2009. Asian dust transported one full circuit around the globe. Nat. Geos. 2, 557–560.

van der Pluijm, B.A., Marshak, S., 1997. Earth Structure: An Introduction to Structural Geology and Tectonics. McGraw-Hill Companies, Inc.

Wang, F., Sun, D., Chen, F., Bloemendal, J., Guo, F., Li, Z., Zhang, Y., Li, B. and Wang, X., 2015a. Formation and evolution of the Badain Jaran Desert, North China, as revealed by a drill core from the desert centre and by geological survey. Palaeogeogr. Palaeclimatol. Palaeoecol. 426, 139–158.

Wang, H., Currie, C.A., DeCelles, P.G., 2015b. Hinterland basin formation and gravitational instabilities in the central Andes: Constraints from gravity data and geodynamic models. In: P.G. DeCelles, M.N. Ducea, B. Carrapa and P.A. Kapp (Editors), Geodynamics of a Cordilleran Orogenic System: The Central Andes of Argentina and Northern Chile. Geological Society of America Memoir 212, Boulder, pp. 387–406.

Wang, J., Fang, X., Appel, E., Zhang, W., 2013. Magnetostratigraphic and radiometric constraints on salt formation in the Qaidam Basin, NE Tibetan Plateau. Quat. Sci. Rev. 78, 53–64.

Wang, J., Xiao, L., Reiss, D., Hiesinger, H., Huang, J., Xu, Y., Zhao, J., Xiao, Z., Komatsu, G., 2018. Geological features and evolution of yardangs in the Qaidam Basin, Tibetan Plateau (NW China): A terrestrial analogue for Mars. J. Geophys. Res.: Planets 123, 2336–2364.

Wang, M., Shen, Z.-K., 2020. Present-day crustal deformation of continental China derived from GPS and its tectonic implications. J. Geophys. Res.: Solid Earth 125, e2019JB018774.

Wang, X., Qiu, Z., Li, Q., Wang, B., Downs, W.R., Xie, G., Xie, J., Deng, T., Takeuchi, G.T., Tseng, Z.J., Chang, M., Liu, J., Wang, Y., Biasatti, D., Sun, Z., Fang, X., Meng, Q., 2007. Vertebrate paleontology, biostratigraphy, geochronology, and paleoenvironment of Qaidam Basin in northern Tibetan Plateau. Palaeogeogr. Palaeoclimatol. Palaeoecol. 254, 363–385.

Wang, X., Xia, D., Wang, T., Xue, X., Li, J., 2008. Dust sources in arid and semiarid China and southern Mongolia: Impacts of geomorphological setting and surface materials. Geomorphology 97, 583–600.

Wang, Y., Wu, F., Zhang, X., Zeng, P., Ma, P., Song, Y., Chu, H., 2016. Formation and evolution of yardangs activated by Late Pleistocene tectonic movement in Dunhuang, Gansu Province of China. J. Earth Sys. Sci. 125, 1603–1614.

Ward, A.W., Greeley, R., 1984. Evolution of the yardangs at Rogers Lake, California. Geol. Soc. Am. Bull. 95, 829–837.

Washington, R., Todd, M., Middleton, N.J., Goudie, A.S., 2003. Dust-storm source areas determined by the Total Ozone Monitoring Spectrometer and surface observations. Ann. Assoc. Am. Geogr. 93, 297–313.

Washington, R., Todd, M.C., Lizcano, G., Tegen, I., Flamant, C., Koren, I., Ginoux, P., Engelstadter, S., Bristow, C.S., Zender, C.S., Goudie, A.S., Warren, A., Prospero, J.M., 2006. Links between topography, wind, deflation, lakes and dust: The case of the Bodélé Depression, Chad. Geophys. Res. Lett. 33, L09401.

Wei, A., Xiao, A., Wu, L., Mao, L., Zhao, H., Shen, Y., Wang, W., 2016. Temporal and spatial patterns of Cenozoic deformation across the Qaidam Basin, Northern Tibetan Plateau. Terra Nova 28, 409–418.

Wen, Y., Wu, Y., Tan, L., Li, D., Fu, T., 2019. End-member modeling of the grain size record of loess in the Mu Us Desert and implications for dust sources. Quat. Int. 532, 87–97.

Westerhold, T., Marwan, N., Drury, A.J., Liebrand, D., Agnini, C., Anagnostou, E., Barnet, J.S.K., Bohaty, S.M., De Vleeschouwer, D., Florindo, F., Frederichs, T., Hodell, D.A., Holbourn, A.E., Kroon, D., Lauretano, V., Littler, K., Lourens, L.J., Lyle, M., Palike, H., Rohl, U., Tian, J., Wilkens, R.H., Wilson, P.A., Zachos, J.C., 2020. An astronomically dated record of Earth's climate and its predictability over the last 66 million years. Science 369, 1383–1387.

Whipple, K.X., 2009. The influence of climate on the tectonic evolution of mountain belts. Nat. Geos. 2, 97–104.

Willett, S.D., 1999. Orogeny and orography: The effects of erosion on the structure of mountain belts. J. Geophys. Res. 104, 28957–28981.

Wu, L., Prush, V., Lin, X., Xiao, A., Zhang, L., Chen, N., Yang, R., Chen, H., 2019. Quantifying wind erosion during the late Quaternary in the Qaidam Basin, Central Asia. Geophys. Res. Lett. 46, 6378–6387.

Wu, W., Yan, P., Wang, Y., Dong, M., Meng, X., Ji, X., 2018. Wind tunnel experiments on dust emissions from different landform types. J. Arid Land 10, 548–560.

Xia, W., Zhang, N., Yuan, X., Fan, L, Zhang, B., 2001. Cenozoic Qaidam basin, China: A stronger tectonic inversed, extensional rifted basin. AAPG Bull. 85, 715–736.

Xiao, L. (Editor), 2021. Mars and Earth: A Study of the Qaidam Basin. Advances in Planetary Science. World Scientific Publishing Company, New Jersey, 337 pp.

Xiao, L., Wang, J., Dang, Y., Cheng, Z., Huang, T.-Y., Zhao, J., Xu, Y., Huang, J., Xiao, Z., Komatsu, G., 2017. A new terrestrial analogue site for Mars research: The Qaidam Basin, Tibetan Plateau (NW China). Earth-Sci. Rev. 164, 84–101.

Xiao, L., Wang, J., Dang, Y., Zhao, J., Zhang, M., 2021. The Qaidam Basin, NE Tibetan Plateau. In: L. Xiao (Editor), Mars on Earth: A Study of the Qaidam Basin. Advances in Planetary Science. World Scientific Company, New Jersey, pp. 71–110.

Xiao, X., Wang, J., Huang, J., Ye, B., 2018. A new approach to study terrestrial yardang geomorphology based on high-resolution data acquired by unmanned aerial vehicles (UAVs): A showcase of whaleback yardangs in Qaidam Basin, NW China. Earth Planet. Phys. 2, 398–405.

Xiong, L.-Y., Tang, G.-A., Li, F.-Y., Yuan, B.-Y., Lu, Z.-C., 2014. Modeling the evolution of loess-covered landforms in the Loess Plateau of China using a DEM of underground bedrock surface. Geomorphology 209, 18–26.

Xu, X., Ma, X., 1992. Geodynamics of the Shanxi Rift system, China. Tectonophysics 208, 325–340.

Xu, Z., Lu, H., Yi, S., Vandenberghe, J., Mason, J.A., Zhou, Y., Wang, X., 2015. Climate-driven changes to dune activity during the Last Glacial Maximum and deglaciation in the Mu Us dune field, north-central China. Earth Planet. Sci. Lett. 427, 149–159.

Xuan, J., Sokolik, I.N., 2002. Characterization of sources and emission rates of mineral dust in Northern China. Atmos. Environ. 36, 4863–4876.

Yang, H., Lohmann, G., Krebs-Kanzow, U., Ionita, M., Shi, X., Sidorenko, D., Gong, X., Chen, X., Gowan, E.J., 2020a. Poleward shift of the major ocean gyres detected in a warming climate. Geophys. Res. Lett. 47, e2019GL085868.

Yang, L., Zhang, W., Fang, X., Cai, M., Lu, Y., 2020b. Aridification recorded by lithofacies and grain size in a continuous Pliocene-Quaternary lacustrine sediment record in the western Qaidam Basin, NE Tibetan Plateau. Palaeogeogr. Palaeclimatol. Palaeoecol. 556, 109903.

Yang, Y., Yang, R., Li, X., Han, W., Zan, J., Fang, X., Appel, E., Galy, A., Wu, F., Yang, S., Zhang, Z., Zhang, W., Ye, C., 2017. Glacial-interglacial climate change on the northeastern Tibetan Plateau over the last 600 kyr. Palaeogeogr. Palaeoclimatol. Palaeoecol. 476, 181–191.

Yao, Z., Xiao, J., Jiang, F., 2012. Characteristics of daily extreme-wind gusts along the Lanxin Railway in Xinjiang, China. Aeolian Res. 6, 31–40.

Yin, A., Dang, Y.-Q., Zhang, M., Chen, X.-H., McRivette, M.W., 2008. Cenozoic tectonic evolution of the Qaidam basin and its surrounding regions (Part 3): Structural geology, sedimentation, and regional tectonic reconstruction. Geol. Soc. Am. Bull. 120, 847–876.

Yin, J., Han, Z., Zeng, Y., Qin, L., Pan, R., Zhou, Y., Lu, M., Zhang, H., Li, X., 2023. The largest deflation basin in Asia reveals that the Miocene basin-filling sdiments in the eastern Gobi Desert are an important dust source. Geomorphology 436, 108780.

Yu, S.-Y., Colman, S.M., Lai, Z.-P., 2019. Late-Quaternary history of 'great lakes' on the Tibetan Plateau and palaeoclimatic implications - A review. Boreas 48, 1–19.

Zan, J., Maher, B.A., Yamazaki, T., Fang, X., Han, W., Kang, J., Hu, Z., 2023. Mid-Pleistocene links between Asian dust, Tibetan glaciers, and Pacific iron fertilization. PNAS 120, e2304773120.

Zeitler, P.K., Meltzer, A.S., Koons, P.O., Craw, D., Hallet, B., Chamberlain, C.P., Kidd, W.S.F., Park, S.K., Seeber, L., Bishop, M., Shroder, J., 2001. Erosion, Himalayan geodynamics, and the geomorphology of metamorphism. GSA Today 11, 4–8.

Zhang, D., Wang, C., Pullen, A., Abell, J.T., Ji, J., Shen, T., 2020a. Landscape evolution and development of eolian-modified unconsolidated gravel surfaces and yardangs in the Hami Basin, China. Geomorphology 368, 107355.

Zhang, D., Wang, G., Abell, J.T., Pullen, A., Winckler, G., Schaefer, J.M., Shen, T., 2022a. Quantifying late Pleistocene to Holocene erosion rates in the Hami Basin, China: Insights

into Pleistocene dust dynamics of an East Asian stony desert. Geophys. Res. Lett. 49, e2021GL097495.

Zhang, H., Lei, G., Chang, F., Pu, Y., Fan, H., Lei, Y., Yang, M., Zhang, W., Yang, L., 2008. Chronology of the shell bar section and a discussion on the ages of hte Late Pleistocene lacustrine deposits in the paleolake Qarhan, Qaidam basin. Front. Earth Sci. Chi. 2, 225–235.

Zhang, H., Lu, H., He, J., Xie, W., Wang, H., Zhang, H., Breecker, D., Bird, A., Stevens, T., Nie, J., Li, G., 2022b. Large-number detrital zircon U-Pb ages reveal global cooling caused the formation of the Chinese Loess Plateau during Late Miocene. Sci. Adv. 8, eabq2007.

Zhang, H., Nie, J., Liu, X., Pullen, A., Li, G., Peng, W., Zhang, H., 2021. Spatially variable provenance of the Chinese Loess Plateau. Geology 49, 1155–1159.

Zhang, J., Hao, Q., Li, S.-H., 2022c. An absolutely dated record of climate change over the last three glacial-interglacial cycles from Chinese loess deposits. Geology 50, 1116–1120.

Zhang, Q., Liu, Q., Roberts, A.P., Larrasoaña, J.C., Shi, X., Jin, C., 2020b. Mechanism for enhanced eolian dust flux recorded in North Pacific Ocean sediments since 4.0 Ma: Aridity or humidity at dust source areas in the Asian interior? Geology 48, 77–81.

Zhang, Q., Liu, Q., Sun, Y., 2020c. Review of recent developments in aeolian dust signal of sediments from the North Pacific Ocean based on magnetic minerals. Geol. Mag. 157, 790–805.

Zhang, W., Appel, E., Fang, X., Setzer, F., Song, C., Meng, Q., Yan, M., 2020d. New paleomagnetic constraints on syntectonic growth strata in the western Qaidam Basin, NE Tibetan Plateau. Tectonophysics 780, 228401.

Zhang, W., Chen, J., Ji, J., Li, G., 2016. Evolving flux of Asian dust in the North Pacific Ocean since the late Oligocene. Aeolian Res. 23, 11–20.

Zhang, Y.Q., Mercier, J.L., Vergely, P., 1998. Extension in the graben systems around the Ordos (China), and its contribution to the extrusion tectonics of south China with respect to Gobi-Mongolia. Tectonophysics 285, 41–75.

Zhao, J., Huang, T., 2021. Lakes. In: L. Xiao (Editor), Mars On Earth: A Study of the Qaidam Basin. World Scientfic Publishing Company, New Jersey, pp. 111–156.

Zheng, D., Zhang, P.-Z., Wan, J., Yuan, D., Li, C., Yin, G., Zhang, G., Wang, Z., Min, W., Chen, J., 2006. Rapid exhumation at ~8 Ma on the Liupan Shan thrust fault from apatite fission-

track thermochronology: Implications for growth of the northeastern Tibetan Plateau margin. Earth Planet. Sci. Lett. 248, 198–208.

Zhisheng, A., Kutzbach, J.E., Prell, W.L., Porter, S.C., 2001. Evolution of Asian monsoons and phased uplift of the Himalaya-Tibetan plateau since Late Miocene time. Nature 411, 62–66.

Zhong, Y., Lu, Z., Wilson, D.J., Zhao, D., Liu, Y., Chen, T., Gai, C., Gong, X., Jiang, Z., Liu, J., Liu, Q., 2023. Paleoclimate evolution of the North Pacific Ocean during the late Quaternary: Progress and challenges. Geosys. Geoenviron. 2, 100124.

Zhou, G., Li, L., Xiao, G., Yan, L., Pearson, D.G., Hao, Q., Wu, Y., 2022. New constraints on the source of loess from U/Th-Pb geochronology of detrital multi-minerals. Geology 50, 1156–1160.

Zhou, J., Xu, F., Wang, T., Cao, A., Yin, C., 2006. Cenozoic deformation history of the Qaidam Basin, NW China: Results from cross-section restoration and implications for Qinghai-Tibet Plateau tectonics. Earth Planet. Sci. Lett. 243, 195–210.

Zhu, Y., Jia, X., Shao, M., 2018a. Loess thickness variations across the Loess Plateau of China. Surv. Geophys. 39, 715–727.

Zhu, Z., Dennell, R., Huang, W., Wu, Y., Qiu, S., Yang, S., Rao, Z., Hou, Y., Xie, J., Han, J., Ouyang, T., 2018b. Hominin occupation of the Chinese Loess Plateau since about 2.1 million years ago. Nature 559, 608–612.

Zhuang, G., Brandon, M.T., Pagani, M., Krishnan, S., 2014. Leaf wax stable isotopes from Northern Tibetan Plateau: Implications for uplift and climate since 15 Ma. Earth Planet. Sci. Lett. 390, 186–198.

Zhuang, G., Hourigan, J.K., Ritts, B.D., Kent-Corson, M.L., 2011. Cenozoic multiple-phase tectonic evolution of the northern Tibetan Plateau: Constraints from sedimentary records from Qaidam Basin, Hexi Corridor, and Subei Basin, northwest China. Am. J. Sci. 311, 116–152.

Declaration of interests

☒The authors declare that they have no known competing financial interests or personal relationships that could have appeared to influence the work reported in this paper.

☐The authors declare the following financial interests/personal relationships which may be considered as potential competing interests: